

# UC San Diego

## Research Theses and Dissertations

**Title**

Exchange at the Estuary-Ocean Interface: Fluxes through the Golden Gate Channel

**Permalink**

<https://escholarship.org/uc/item/2qz6m0sv>

**Author**

Fram, Jonathan Peter

**Publication Date**

2005-10-01

# **Exchange at the Estuary-Ocean Interface: Fluxes through the Golden Gate Channel**

by

Jonathan Peter Fram

B.A., (Pomona College), 1995  
M.S. (University of California, Berkeley), 2001

A dissertation submitted in partial satisfaction of the requirements for the degree of  
Doctor of Philosophy in Engineering – Civil and Environmental Engineering  
in the GRADUATE DIVISION of the  
UNIVERSITY OF CALIFORNIA, BERKELEY

Committee in charge:

Professor Mark T. Stacey, Chair  
Professor James R. Hunt  
Professor Thomas M. Powell

Fall 2005

UMI Number: 3210585

Copyright 2005 by  
Fram, Jonathan Peter

All rights reserved.

### INFORMATION TO USERS

The quality of this reproduction is dependent upon the quality of the copy submitted. Broken or indistinct print, colored or poor quality illustrations and photographs, print bleed-through, substandard margins, and improper alignment can adversely affect reproduction.

In the unlikely event that the author did not send a complete manuscript and there are missing pages, these will be noted. Also, if unauthorized copyright material had to be removed, a note will indicate the deletion.

**UMI**<sup>®</sup>

---

UMI Microform 3210585

Copyright 2006 by ProQuest Information and Learning Company.

All rights reserved. This microform edition is protected against unauthorized copying under Title 17, United States Code.

ProQuest Information and Learning Company  
300 North Zeeb Road  
P.O. Box 1346  
Ann Arbor, MI 48106-1346

**Exchange at the Estuary-Ocean Interface: Fluxes through the Golden Gate Channel**

Copyright 2005 by Jonathan Peter Fram

The dissertation of Jonathan Peter Fram is approved:

---

Chair Date

---

Date

---

Date

University of California, Berkeley

Fall 2005

## **Abstract**

Exchange at the Estuary-Ocean Interface:

Fluxes through the Golden Gate Channel

by

Jonathan Peter Fram

Doctor of Philosophy in Engineering — Civil and Environmental Engineering

University of California, Berkeley


Professor Mark T. Stacey, Chair

Residual flow and exchange along a channel connecting an embayment with the coastal ocean are examined experimentally, using direct observations of currents and scalar concentrations across the mouth of San Francisco Bay. The study encompasses separate experiments during each of three “seasons”: winter/spring runoff (March 2002), summer upwelling (July 2003), and fall relaxation (October 2002). Within each experiment, transects across the channel were repeated approximately every 12 minutes for 25 hours during both spring and neap tides. Velocity was measured from a boat-mounted acoustic Doppler current profiler. Scalar concentrations were measured at the surface and from a tow-yoed SeaSciences Inc. Acrobat.

Several sources of residual circulation were isolated: baroclinic flow, tidal pumping, and frictional phasing. We further isolated a portion of tidal pumping as tidal trapping of a headland eddy during flood tide. Density-driven flow is complicated by a dramatic growth in the cross-channel density gradient during the second half of ebb tide, which

drives along-channel shear at the beginning flood tide, creating an asymmetry in frictional phasing.

Velocity fields formed by residual circulation mechanisms combine with scalar concentration fields to define scalar exchange processes. Net salinity exchange rates for each season are quantified with harmonic analysis. Harmonic results are then decomposed into flux mechanisms using temporal and spatial correlations. In this study, the temporal correlation of cross-sectionally averaged salinity and velocity (tidal pumping flux) is the largest component of the dispersive flux of salinity into the bay. From the tidal pumping flux portion of the dispersive flux, it is shown that there is less exchange than was found in earlier studies. Furthermore, tidal pumping flux scales strongly with freshwater flow because of density-driven movement of a tidally trapped eddy and stratification-induced increases in ebb-flood frictional phasing. Complex bathymetry leads to salinity exchange that scales differently with flow than would be expected from simple tidal asymmetry and gravitational circulation models.



12-19-05

## Table of Contents

<b>1</b>	<b>INTRODUCTION.....</b>	<b>1</b>
1.1	BAY MOUTHS .....	1
1.2	SAN FRANCISCO BAY SALINITY.....	4
1.3	SETTING SAN FRANCISCO BAY SALINITY .....	5
1.4	FROM SALINITY TO OTHER SCALARS.....	6
1.4.1	<i>Sediment Flux</i> .....	6
1.4.2	<i>Chlorophyll Fluxes</i> .....	8
1.4.3	<i>Other Scalar Fluxes of Importance</i> .....	8
1.5	HYDRODYNAMICS OF EXCHANGE .....	9
1.5.1	<i>Introduction</i> .....	10
1.5.2	<i>Bathymetric Influence</i> .....	11
1.5.2.1	Tidal Pumping .....	12
1.5.2.2	Tidally Trapped Eddies .....	13
1.5.2.3	Hydraulics .....	14
1.5.3	<i>Density Driven Exchange</i> .....	16
1.5.3.1	Highly Stratified Estuaries.....	16
1.5.3.2	Partially Mixed Estuaries .....	16
1.5.3.3	Estuarine Circulation.....	17
1.5.3.4	Strain Induced Periodic Stratification.....	18
1.5.3.5	Shoal-Channel Dynamics .....	19
1.5.3.6	Application to Salt Fluxes .....	20
1.6	SUMMARY OF PROJECT GOALS .....	21
<b>2</b>	<b>EXPERIMENTAL DESIGN.....</b>	<b>29</b>
2.1	FIELD SITE .....	29
2.2	SUMMARY OF METHODOLOGY .....	30
2.3	PREVIOUS GOLDEN GATE EXCHANGE EXPERIMENTS.....	30
2.4	INSTRUMENTS.....	32
2.4.1	<i>Introduction</i> .....	32
2.4.2	<i>Acrobat</i> .....	33
2.4.3	<i>Acrobat Payload</i> .....	34
2.4.4	<i>Boat-Mounted Instruments</i> .....	35
2.4.5	<i>Oblique Angle Photographs</i> .....	37
2.5	THE EXPERIMENT .....	37
2.5.1	<i>Three Seasons</i> .....	37
2.5.2	<i>Field Testing</i> .....	39
2.5.3	<i>Spring 2002 Neap Tide</i> .....	41
2.5.4	<i>Fall 2002</i> .....	44
2.5.5	<i>Summer 2003</i> .....	46
2.6	ANCILLARY DATA STREAMS .....	46
2.7	CONCLUSION .....	47
<b>3</b>	<b>CHARACTERIZING FLOW AND EXCHANGE.....</b>	<b>57</b>
3.1	INTRODUCTION.....	57
3.2	2D GRID.....	57
3.3	SEABIRD GRIDDING .....	58
3.4	VELOCITY KRIGING .....	59
3.5	SPLINING, AN ALTERNATIVE TO KRIGING .....	63
3.6	SCALAR KRIGING.....	64
3.7	OVERVIEW OF CONDITIONS .....	65
<b>4</b>	<b>TIDAL VARIABILITY .....</b>	<b>75</b>
4.1	INTRODUCTION.....	75
4.2	PRINCIPAL COMPONENT ANALYSIS.....	75



4.2.1	<i>Theory</i> .....	75
4.2.2	<i>Empirical Orthogonal Functions</i> .....	77
4.2.3	<i>EOF Tidal Variability</i> .....	79
4.3	MODELING TIDAL VARIABILITY .....	81
4.4	AXIAL CIRCULATION .....	84
4.5	TIDAL VARIABILITY SUMMARY .....	86
<b>5</b>	<b>RESIDUAL FLOW</b> .....	<b>97</b>
5.1	RELEVANT FORCING MECHANISMS .....	97
5.2	RESIDUAL FIELDS .....	100
5.3	RESIDUAL FLOW MECHANISMS .....	101
5.3.1	<i>Quantifying Mechanisms</i> .....	101
5.3.2	<i>Lateral Shear from Tidal Pumping</i> .....	103
5.3.3	<i>Traditional Density Driven Shears</i> .....	106
5.3.4	<i>Sill Induced Vertical Shear</i> .....	107
5.3.5	<i>Shear by Asymmetric Frictional Phasing</i> .....	108
5.3.6	<i>Shear from Axial Circulation</i> .....	112
5.3.7	<i>Vertical Shear Source Comparison</i> .....	113
5.4	SEASONAL VARIABILITY OF RESIDUAL FLOW DYNAMICS .....	114
5.5	RESIDUAL FLOW SUMMARY .....	116
<b>6</b>	<b>SCALAR EXCHANGE</b> .....	<b>123</b>
6.1	INTRODUCTION.....	123
6.1.1	<i>Baroclinic Exchange</i> .....	125
6.1.2	<i>Tidal Pumping and Trapping</i> .....	126
6.1.3	<i>Shear Dispersion</i> .....	128
6.1.4	<i>Exchange Process Summary</i> .....	128
6.2	ANALYSIS METHODS .....	129
6.2.1	<i>Flux Decomposition</i> .....	129
6.2.2	<i>Harmonic Analysis</i> .....	133
6.3	NET FLUXES.....	135
6.3.1	<i>Advective Flux</i> .....	136
6.3.2	<i>Advective vs. Total Dispersive Flux</i> .....	138
6.4	DISPERSION PROCESSES .....	139
6.4.1	<i>Tidal Pumping</i> .....	139
6.4.1.1	<i>Flood-Ebb Tidally Trapped Eddy</i> .....	144
6.4.1.2	<i>Ebb-Flood Frictional Phasing</i> .....	147
6.4.1.3	<i>Tidal Exchange Ratio</i> .....	148
6.4.2	<i>Steady Fluxes</i> .....	151
6.4.3	<i>Unsteady Shear Flux</i> .....	153
6.5	DISPERSION COEFFICIENTS.....	153
6.6	EXCHANGE SUMMARY .....	157
<b>7</b>	<b>CONCLUSIONS AND FUTURE WORK</b> .....	<b>166</b>
7.1	METHODS.....	166
7.2	TIDAL PUMPING AND TRAPPING .....	167
7.3	CONSIDERATIONS FOR FUTURE STUDIES .....	170

## List of Figures

Figure 1.1: Schematic of wide and narrow mouths of bays .....	23
Figure 1.2: Examples of wide and narrow bay mouths.....	24
Figure 1.3: Schematic of a tidal system without mixing .....	25
Figure 1.4: Tidal Pumping Schematic.....	26
Figure 1.5: San Francisco Bay Region.....	27
Figure 1.6: Golden Gate Channel Field Site.....	28
Figure 2.1: SeaSciences Acrobat.....	49
Figure 2.2: Tow-yo Profiling Schematic .....	50
Figure 2.3: Rope-Clutch System.....	51
Figure 2.4: Boat-Mounted Instruments .....	52
Figure 2.5: Tow-Body Location.....	53
Figure 2.6: Turning Into the Tide.....	54
Figure 2.7: Acrobat Instability .....	55
Figure 2.8: Vertical Profiling Schematic.....	56
Figure 3.1: Grid Path.....	69
Figure 3.2: Spline Features .....	70
Figure 3.3: Typical Spring-Runoff Velocities .....	72
Figure 3.4: Typical Fall-Relaxation Velocities.....	73
Figure 3.5: T-S Relationship.....	74
Figure 4.1: Along-Channel EOFs .....	87
Figure 4.2: Cross-Channel EOFs .....	88
Figure 4.3: Density EOFs .....	89
Figure 4.4: Tidally Aligned EOF Time Series.....	90
Figure 4.5: Modeled Velocity.....	91
Figure 4.6: Measured Vertical Shear.....	93
Figure 4.7: Modeled 2D Residual Velocity .....	94
Figure 4.8: Measured Circulation Data .....	95
Figure 4.9: Circulation Schematic.....	96
Figure 5.1: Average Velocity and Density .....	118
Figure 5.2a: Conical Tidal Pumping Schematic .....	119
Figure 5.2 b & c: Conical Tidal Pumping Results .....	120
Figure 5.3: Low Slack Frictional Phasing .....	121
Figure 5.4: Seasonal Bay Density Response to Outflow.....	122
Figure 6.1: Averaging Order Schematic.....	159
Figure 6.2: Averaging Order Ratios.....	160
Figure 6.3: Tidally-Aligned Data.....	161
Figure 6.4: Tidal Pumping Across the Grid.....	162
Figure 6.5: Tidal Pumping vs. TER .....	163
Figure 6.6a: Channel Cross-section Bathymetry .....	164
Figure 6.6b: Channel Cross-sectional Area .....	164
Figure 6.7: Dispersion Coefficients.....	165
Figure 7.1: Photograph of a Lateral Front .....	177
Figure 7.2: A Lateral Front Follows the Eddy.....	177
Figure 7.3: Sudden Changes at the Front .....	178

### List of Tables

Table 2.1: Sampling Times (in year days).....	44
Table 3.1: Summary of Conditions .....	68
Table 5.1: Baroclinic Scaling Data .....	98
Table 6.1: R <sup>2</sup> Values of Harmonic Verification.....	135
Table 6.2: Advective vs. Dispersive Fluxes .....	137
Table 6.3: Dispersive Flux Decomposition .....	141
Table 6.4: Tidal Exchange Ratios .....	148

## **Acknowledgements**

These data were collected with the skilled support of the crew of the USGS *R/V Turning Tide*, captained by Jay Cuetara, and operated with Jon Yokomizo, Chris Smith, and Curt Battenfield. Field assistance on the boat was provided by Maureen Martin, David Ralston, James Gray, Stefan Talke, and Deanna Sereno. Gaj Sivangan, Sarah Giddings, and Deanna Sereno did oblique angle photography of the experiment from shore. Matt Brennan, Maureen Martin, David Ralston, Seungjin Baek, and Miranda Fram gave invaluable advice on data analysis and/or modeling. Liz Perotti and the three members of my dissertation committee helped me edit this document.

Many thanks go to Mark Stacey for designing this project, acquiring the necessary funding and equipment for it, teaching me environmental fluid mechanics, and helping me analyze and describe this data set.

This material is based upon work funded by the National Science Foundation under Grant No. OCE-0094317 to Mark Stacey and by California Sea Grant R/CZ-170 to Mark Stacey and Thomas Powell.

# 1 Introduction

## 1.1 Bay Mouths

Estuaries are defined by their salinity fields. Put simply, “an estuary is where a river meets the sea,” [p.229 *Fischer et al.*, 1979]. Estuaries are thus bounded by the seaward extent of freshwater influence and the upstream extent of saltwater influence. In this project, we investigate why San Francisco Bay has the salinity it has by studying the mouth of the bay, the Golden Gate Channel. This chapter includes an introduction to ocean-estuary exchange at bay mouths, reasons for characterizing this estuary’s salt field, a description of the importance of quantifying the mechanisms for salt exchange, and an overview of hydrodynamics related to ocean-estuary exchange.

We start with an idealized river exiting into a bay that is connected to the ocean (figure 1.1). In figure 1.1a, the mouth of the bay is wide, while in figure 1.1b the mouth is narrow. Which bay will have fresher water? The Salinas River to Monterey Bay to Pacific Ocean system is an example of wide mouth case (figure 1.2a). Monterey Bay has nearly oceanic salinity [*Ramp et al.*, 2005]. The Catatumbo River to Lake Maracaibo to Gulf of Venezuela system is an example of the opposite extreme (figure 1.2b). Lake Maracaibo maintains salinity fresher than 12 PSU (Practical Salinity Units) [*Findikakas et al.*, 2001]. Several factors set the salinity differences between Monterey Bay and Lake Maracaibo.

Tidal forcing is much stronger in Monterey Bay than in Lake Maracaibo. The mean tidal range is 30cm at the mouth of Lake Maracaibo [*Redfield*, 1961], while it is 3.5 times as

large (107cm) at both sides of the mouth of Monterey Bay [www.co-ops.noaa.gov].

Stronger tides push more water in and out of the bay during each tidal cycle. If the same water returned to the ocean on ebb tide that entered it on flood tide, then the tides would not change the average salinity of the bay by much. This is illustrated in figure 1.3. The tidal cycle presented in figure 1.3 starts at the beginning of flood tide because it is assumed that the ocean is large enough and its currents are strong enough to quickly dilute and remove the freshwater plume that exits the bay during the previous ebb tide.

This exchange can be described more quantitatively by examining equations for the bay's water and salt budgets. The water budget at the mouth over a tidal cycle is:

$$\int_{t_f} U_f A_f dt + \int_{t_e} U_e A_e dt = Q_r \cdot (t_f + t_e) \quad (1)$$

where  $U$  is the velocity through the mouth,  $A$  is the area of the mouth,  $Q_r$  is the river flow rate,  $t$  is time, the  $f$  subscript refers to flood tide, and the  $e$  subscript refers to ebb tide.

The total volume of water exiting the mouth during ebb tide is greater than the volume entering the bay during flood tide by an amount equal to the river flow rate times the tidal period. The salt budget for the bay over a tidal cycle is:

$$\int_{t_f} S_f U_f A_f dt + \int_{t_e} S_e U_e A_e dt \cong 0 \quad (2)$$

$S_e$  and  $S_f$  are the ebb and flood salinities at the mouth. The salinity of the river water entering the bay is assumed to be negligible. To complete this salt balance, average flood salinity should be higher than ebb salinity [Fischer *et al.*, 1979]. In figure 1.3e, ebb tide returns all of the flood water plus a small amount of freshwater. The volume of this freshwater is equal to the river flow times the tidal time period.

If however, there is mixing between the flood water and the bay water in the bay, then the ebb tide will not return all of the water from the previous flood tide to the ocean. To maintain the salt balance, the bay water will have to be saltier than in the non-mixing case shown in figure 1.3. We will precisely define mechanisms for mixing later in this chapter and in chapter 6. Examples of mixing processes that are not part of figure 1.3 include tidal pumping [*Stommel and Farmer, 1952*], which is shown in figure 1.4, and entrainment along the edges of the flood jet [*Kundu and Cohen, 2002, pp. 443-448*]. The essential effect of strengthening tides on ocean-bay exchange is to stir waters more vigorously, which increases mixing between ocean and bay waters. Stronger tides also bring more oceanic water into bays on flood tide, making more water available for mixing in bays. A major goal of this project is to examine how shape and size of a bay mouth influences tidal mixing. The overall effect of the width of the mouth on mixing is not immediately obvious. A wide mouth allows more oceanic water to be available for mixing in the bay. However, bathymetric irregularities such as a contraction at the mouth may reduce the tidal flow rate, but they also combine with tides to increase mixing.

The amount of river flow into a bay also affects a bay's salinity. If the river flow is very large, then saltwater might not intrude into the bay at all. An extreme example of this is the Amazon River, which has a freshwater plume that often extends over one hundred kilometers into the Atlantic Ocean [*Geyer et al., 1996*]. If annual river flow is small compared to the volume of a bay, it quickly can be evaporated from the bay's surface or mixed out by tides, and thus it may leave the bay with near oceanic salinity

(e.g. Monterey Bay). With moderate river flow, strong longitudinal density gradients can develop in a bay [*Hansen and Rattray, 1965*]. These density gradients can drive salinity exchange through a bay mouth [e.g. Lake Maracaibo, *Horn et al., 2001*].

Both tides and river flows influence exchange dynamics at the bay mouth studied for this project, the Golden Gate Channel [*Largier, 1996*]. Furthermore, we will also need to consider whether exchange is driven by other mechanisms, such as evaporation from the bay surface, wind, or the Coriolis Effect. We will examine how the size and shape of the Golden Gate Channel affects salinity exchange caused by each mechanism, and thus how the mouth affects the salinity of San Francisco Bay.

## **1.2 San Francisco Bay Salinity**

Using the definition that an estuary is bounded by waters with riverine and oceanic salinities, the San Francisco Bay Estuary extends from the Sacramento-San Joaquin Delta to the Golden Gate Channel (figure 1.5). The San Francisco Bay Estuary is the largest in California in terms of its surface area ( $\sim 1300 \text{ Mm}^2$ ), the watershed area it drains (half of the state), and the annual freshwater flow it conveys ( $\sim 20,000 \text{ Mm}^3$ ). For their size, estuaries have enormous ecological value. Thus, the simplest reason to study the salinity of San Francisco Bay is to aid understanding of the estuarine ecosystem. Quantitatively, the abundance of a wide variety of estuarine organisms is related to the salinity at various locations in the San Francisco Bay Estuary during certain times of the year [*Kimmerer, 2002b*].



Jassby et al. [1995] demonstrated that populations of several important species, such as striped bass and starry flounder, are inversely related to the salinity of the bay. Bay salinity is parameterized by X2, which is the 2 parts per thousand bed salinity distance from the Golden Gate Bridge along the main axis of the estuary. Increasing freshwater input to the bay from the Sacramento-San Joaquin Delta compresses the salt field towards the Golden Gate, decreasing X2. A direct relationship can be made between X2 at certain times of the year and populations of organisms from phytoplankton to the striped bass in the Bay-Delta [Kimmerer, 2002a]. There is a tradeoff between supplying freshwater for lowering X2 to support the estuary's ecosystem and diverting freshwater for agriculture, municipal, and industrial use. Regulators manage the estuary's ecosystem by adjusting the estuary's salt field, as parameterized by X2.

### **1.3 Setting San Francisco Bay Salinity**

Raising freshwater input does not lower X2 as much as standard estuarine hydrodynamic theories predict [Monismith et al., 2002]. Part of the motivation for this project is to investigate the hydrodynamic processes that are determining X2. The theoretical background for the project and its application to X2 will be presented in section 1.5. Also, just as the connection between freshwater inflow and X2 is not completely understood, there is not yet a full explanation of the X2 to ecosystem health relationship [Kimmerer, 2002a]. Do, for example, lower X2 values benefit organisms that live within a certain salinity range by bringing them downstream to a part of the bay with more fringing wetlands or by increasing stratification [Kimmerer, pers. comm. 2004]? Thus it

is useful to measure, for example, how much stratification is generated by the salinity exchange processes that occur at the mouth and into the bay.

#### **1.4 From Salinity to Other Scalars**

Important scalars other than salinity, such as organic carbon and sediment, are exchanged between the coastal ocean and the estuary through the Golden Gate, but these fluxes are not as well understood [*Jassby et al.*, 1993; *Krone*, 1996] because of spatial heterogeneity and energetic mixing in the region. With detailed measurements of one relatively conservative scalar, such as salinity, distributions of other scalars from limited measurements can be modeled.

##### **1.4.1 Sediment Flux**

Anthropogenic changes in the bay's sediment flux have dramatically altered the bay's bathymetry. Hydraulic mining increased sediment flux by an order of magnitude in the late 1800s [*van Geen and Luoma*, 1999], filling Suisun Bay by 1m and Central Bay by 0.25m—large amounts considering the bay has a median depth of only 2m [*Chin et al.*, 2004]. Sediment surpluses from hydraulic mining continue to enter the bay even though hydraulic mining ceased in 1884. More recently, it is becoming apparent that dams are decreasing sediment input [*Wright and Schoellhamer*, 2004]. Locally, there is a variety of sediment sources and sinks related to human activity. The bay's shoreline continues to change by a combination of development (e.g. a possible San Francisco airport runway extension) and restoration (e.g. South Bay salt evaporation ponds). To keep shipping channels and marinas open, at a cost of \$30-60M, 6M cubic yards of sediment are

dredged annually, an amount comparable to the estimated annual Golden Gate sediment efflux [*Chin et al.*, 2004; *LTMS*, 1998]. Near the Golden Gate, dredging occurs from the ebb bar at the western end of the Golden Gate Channel, and some dredge spoils are deposited in the channel. In recent years, the dredged material pile adjacent the western side of Alcatraz did not disperse as quickly as expected, threatening to interfere with shipping traffic, creating environmental concerns, and leading to a new dredging management strategy [*LTMS*, 1998]. Historically, removal of sediments occurred in the vicinity (within 5 km) of this field site in the form of sand mining [*Chin et al.*, 2004]. In addition to helping to describe changes to the bay's morphology, characterizing sediment exchange at the mouth could also aid understanding of the fate of contaminants attached to sediments, such as mercury [*Schoellhamer*, 1996].

Sediment transport models can be validated using measures of suspended solids concentration in river inflows and of erosion and deposition of the estuarine bed, but there have not been accurate measures of suspended solid fluxes at the Golden Gate [*Krone*, 1996]. Output of sediment is likely to be less variable than input, because most of the suspended sediment around the Golden Gate is from tidal resuspension, although a large portion of the annual load exits the channel following large winter/spring storms [*Schoellhamer*, 2002]. The USGS measured suspended solids concentration on the south side of the Golden Gate for several years, but the spatial heterogeneity of the concentration across the channel, as is needed for a flux calculation, remains unknown [*Schoellhamer*, 1996, Ganju pers. comm. 2004]. Suspended sediment concentration (SSC) generally increases with depth, so in addition to direct SSC measurements,

description of vertically sheared exchange processes from the salt flux analysis may support future sediment flux analysis.

### **1.4.2 Chlorophyll Fluxes**

The exchange of biological scalars are also not well characterized. Researchers have measured chlorophyll concentration in the bay, but modeling the production in the estuary also requires data on exchange in and out of the bay [Cloern, 1996]. As with suspended sediment, chlorophyll concentration was measured for this experiment, and the flux results are not as robust as they are for salinity. We will discuss salinity exchange in detail, and this will provide a basis for future work on chlorophyll fluxes.

### **1.4.3 Other Scalar Fluxes of Importance**

Characterizing exchange through estuary mouths is critical to analysis of scalar transport in estuaries. By accurately measuring salt and heat exchange as well as residual flow, a model can be created to calculate exchange of other scalars. Prandle [1990], for example, quantifies oxygen exchange at the Mersey River—Liverpool Bay boundary from surface oxygen measurements and the proportion of exchange due to baroclinic circulation.

The exchange mechanisms also transport juvenile fauna that cannot swim effectively. For example, in late spring Dungeness crab (*Cancer magister*) larvae move from the coastal ocean to San Pablo Bay despite very poor swimming ability. While harvests are down by over an order of magnitude, two million pounds of Dungeness crabs are still caught in Central California annually, and each of those crabs lived as a juvenile for

approximately one year in an estuary [<http://www.sfws.org>]. It is valuable to understand more about their life cycle. Drifter studies qualitatively demonstrated that particles that stay near the bottom move from the ocean to San Pablo Bay [Conomos *et al.*, 1971]. Although at first glance, one might assume that the *C. magister* larvae ride this baroclinic current, it has not been shown that *C. magister* larvae float along the bottom continuously during migration. In some cases, other larvae use tides rather than density-driven circulation to navigate through estuaries; in those cases the buoyant estuarine water might merely signal a bay's location [Epifanio and Garvine, 2001]. It has been shown for example that menhaden, a planktivorous fish, migrate by tidal stream transport, migrating vertically depending on if it is ebb or flood tide [Epifanio and Garvine, 2001]. *C. magister* may migrate via estuarine fronts [Eggleston *et al.*, 1998], which are generated by the interaction of tidal asymmetries with along-channel density gradients [O'Donnell, 1993]. To model how *C. magister* larvae move from the coastal ocean to San Francisco Bay, it would be useful to quantify the proportion of vertical exchange to depth-average exchange processes. To model how they end up in North Bay as opposed to South Bay, one also should characterize cross-channel asymmetries and exchange.

The oxygen exchange and larval transport examples illustrate how this project could aid understanding of the transport of any nutrient or planktivorous species through the mouth of San Francisco Bay.

## **1.5 Hydrodynamics of Exchange**

After establishing the value of characterizing exchange at the Golden Gate, here the theoretical background for describing ocean-estuary exchange is presented.

### 1.5.1 Introduction

The connection between the coastal ocean and estuaries is defined by the complex interaction of energetic tides, density variations, wind forcing, and local bathymetry [*Jay et al.*, 1997]. Longitudinal and vertical gradients in salinity and temperature result in a density field that both drives baroclinic flow and inhibits vertical mixing through stabilization of the water column [*Prandle*, 1985]. Superposition of these dynamics with tidal flows results in tidal asymmetries that can produce large net transport [e.g. Strain-Induced Periodic Stratification, or SIPS, *Simpson et al.*, 1990].

In most studies of estuary dynamics [*Bowen and Geyer*, 2003; *Prandle et al.*, 1990], relatively uniform stretches of estuary are considered in order to focus on the interaction of density forcing and the tides. However, at the ocean-estuary interface bathymetric variations are more pronounced and produce a tidal asymmetry of their own, with a momentum jet entering the estuary on flood tides and a radial potential flow exiting on ebb [*Stommel and Farmer*, 1952]. Smaller scale features, such as sills and islands, which are also frequently present near estuary mouths, further perturb the flow field, creating additional variability at finer scales. It is therefore likely that ocean-estuary exchange is characterized by three-dimensional flow structures resulting from both bathymetric and density influences on tidal flows. New instruments [*Jay et al.*, 1997] make it possible to explore exchange hydrodynamics in such complex systems, and, specifically, to refine

previous characterizations of exchange at the Golden Gate [Largier, 1996; Parker et al., 1972; Walters and Gartner, 1985].

To determine which hydrodynamic mechanisms are more important at the Golden Gate, we examine the residual flow at a cross section, using an approach that is similar to that presented by Jay and Smith [1990] and Stacey et al. [2001]. “Residual” implies averaging over meaningful time period—one that integrates over a cycle of variable forcing, such as a wind event, a tidal cycle, a freshet pulse, or a diurnal solar heating cycle. In this case, the tidal cycle is the main source of velocity variability.

Consequently, our residual flows will be tidally averaged flows. A detailed discussion of residual flow at the Golden Gate is presented in chapter 5.

Flow fields combine with scalar concentrations to make scalar mass exchange (e.g. equation 2). Fischer [1972] develops a method for separating exchange processes from repeated cross-section velocity and scalar concentration measurements. Dyer [1997] reviews variants on Fischer’s method to account for irregular cross-section bathymetry, large lateral exchanges, and alternate coordinate systems. In chapter 6, exchange processes are isolated using an alternative to Fischer’s method, and then correlated with the residual flow mechanisms.

### **1.5.2 Bathymetric Influence**

Many estuaries have clearly defined mouths that demark their ocean-estuary boundary. A clearly defined mouth is one where the cross-sectional area of an estuary goes from

being narrow to very wide in a small along-channel distance. Where the mouth is formed by a sand bar, such as for the Roanoke River, ocean waves and currents constrain the ocean-estuary interface to narrow passages. In glacially scoured fjords, sills can demarcate the estuary mouth [e.g. Knight Inlet, *Farmer and Armi*, 1999]. In San Francisco Bay, the mouth is narrower than the rest of the bay because of seismic faulting [Dyer, 1997]. In contrast, other estuaries, such as the Nile and Brahmaputra River, bifurcate into wide deltas.

### 1.5.2.1 Tidal Pumping

Stommel and Farmer [1952] coined the term “tidal pumping” in relation to ocean-estuary exchange. It refers to the tidal asymmetry created by a bathymetric contraction. On flood tide, a jet of water enters an estuary (figure 1.4). Assuming lateral entrainment is negligible and the region is of constant depth, the flood jet is as wide as the contraction. On ebb, flow is toward the contraction center from all landward locations, because the channel water surface is lower than the estuary’s surface. Again assuming that no lateral mixing occurs at the flow edges, the radial flow towards the center can be described as an irrotational drain [figure 1.4 and *Kundu and Cohen*, 2002 p.149]. The jet-drain asymmetry exchanges salt between the ocean and the estuary. Averaging over a tidal cycle, Stommel and Farmer define the tidal exchange ratio (TER) as:

$$TER = \frac{\bar{S}_{Flood} - \bar{S}_{Ebb}}{\bar{S}_{Ocean} - \bar{S}_{Ebb}} \quad (3)$$

where  $\bar{S}$  is average salinity across a transect path during ebb or flood tide, or it represents oceanic salinity. Ozsoy [1977] shows how the jet-drain asymmetry impacts TER as a function of channel width and tidal magnitude. Chadwick and Largier [1999a;



1999b] successfully apply Ozsoy's relations to jet-drain exchange on the seaward side of the contraction at the mouth of San Diego Bay.

### 1.5.2.2 Tidally Trapped Eddies

Mixing and entrainment at the edges of jet-drain flow, however, is not negligible in many cases. In a laboratory study, Wells et al. [2003] show how large tidal eddies develop in the lee of contractions. The size of the tidal eddies at this field site, which is located at the east end of the Golden Gate Channel (figure 1.6), is constrained by the width of the subembayments on each side of the Golden Gate Channel just landward of the Golden Gate Bridge. In this sense, they can be considered tidally trapped eddies. The effect of these eddies on along-channel dispersion has been scaled by Okubo [1973]. Salty water is trapped in side embayments starting towards the beginning of flood tide, and then released back into the channel at the beginning of ebb. The delay between when water enters and leaves a side embayment causes along-channel dispersion. Analytical solutions to tidal trapping, such as Okubo's [1973], apply only to side subembayments much smaller than the main channel and the tidal excursion. For a tidal channel with a small side subembayment:

$$\text{effective diffusivity} = \left\{ \frac{1}{1 + \varepsilon} + \frac{\beta \varepsilon}{2(1 + \varepsilon)^3} \frac{u^2}{Ak} \right\} A + \text{sinusoidal terms} \quad (4)$$

where  $A$  is the along-channel eddy diffusivity,  $\varepsilon$  is ratio of the size of the subembayment to that of the main channel,  $u$  is the maximum tidal velocity,  $k$  is an exchange-rate coefficient, and  $\beta$  is function of  $\varepsilon$  and  $k$  [Okubo, 1973]. At this field site, where the flow

field resembles something in between tidal pumping and tidal trapping, there is not a simple analytical solution for the bathymetric impact on exchange.

An experimental approach to understanding exchange at a contraction requires measuring the velocity field of the tidally trapped eddies. Geyer and Signell [1990] were the first to measure velocity across headland eddies over a tidal cycle with moored and shipboard Acoustic Doppler Current Profilers (ADCPs). Headlands like those at the Golden Gate are often three-dimensional impingements on flow; they intrude more into the channel at depth than at the surface. Edwards et al. [2004] measure and model the tidal mixing, vorticity, and vertical shear caused by this type of three-dimensional headland. There are three relevant headlands at the eastward edge of the Golden Gate Channel, one on each side of the Golden Gate Bridge and one a kilometer landward of the bridge on the north side of the channel (figure 1.6).

### **1.5.2.3 Hydraulics**

Stratification can combine with a bathymetric contraction to limit along-channel salt exchange and locally increase vertical mixing. Farmer and Armi [1986] derive the maximal exchange between two basins of different densities undergoing two-layer vertical exchange. Essentially, an internal hydraulic control develops in relation to the velocity difference between the two layers and the internal wave speed along the interface between the two layers:

$$u_{\text{int}} = \sqrt{\frac{g' h_1 h_2}{h_1 + h_2}}, g' = g \frac{\rho_2 - \rho_1}{\rho} \quad (5)$$

where  $\rho_x$  and  $h_x$  are the densities and heights of the two vertical layers. From conservation of mass and the Bernoulli equation for the two layers, Farmer and Armi show there is a control when the sum of the square of the internal Froude numbers is equal to one:

$$G^2 = Fr_1^2 + Fr_2^2 = \frac{u_1^2}{g' h_1} + \frac{u_2^2}{g' h_2} \quad (6)$$

They successfully applied this theory to data on exchange between the Mediterranean Sea and the Atlantic Ocean through the Strait of Gibraltar [Farmer and Armi, 1986], as well as to stratified fjords such as Knight Inlet [Farmer and Armi, 1999]. Internal hydraulic controls have also been observed in estuaries [MacDonald and Geyer, 2005]. On larger spatial scales, internal hydraulics influence exchange along the Fram Strait [Timmermans and Pratt, 2004], which is the only deep channel connecting the Arctic Ocean with global ocean currents.

To estimate whether internal hydraulic controls may exist at the Golden Gate, we can use Ivey's [2004] classification system. Ivey defines a parameter space in which hydraulics limit exchange versus one in which vertical mixing eliminates the exchange velocity ( $u_1 - u_2$ ). He combines the internal control constraint on exchange (equation 6) with an exchange velocity constraint derived from a momentum balance between the along-channel density gradient and vertical shear stress:

$$\int_{-H}^0 \mathbf{g} \frac{\partial \rho}{\partial x} dz = \rho_o \frac{\partial}{\partial z} \left( K \frac{\partial u}{\partial z} \right) \quad (7)$$

### 1.5.3 Density Driven Exchange

#### 1.5.3.1 Highly Stratified Estuaries

Away from internal hydraulic controls, there is much less vertical mixing in highly stratified estuaries. In weakly tidal systems, such as the mouth of the Mississippi River, stratification confines much of the salt to a wedge that intrudes underneath the fresh water. The slope of the wedge is controlled by balance between the baroclinic pressure gradient and friction at the interface [Dyer, 1997]. Key to understanding exchange in highly stratified systems is mixing at the interface [Kay and Jay, 2003a; Kay and Jay, 2003b]. In highly stratified estuaries that are strongly tidal or that have sharp bathymetric gradients (e.g. sills and headlands), salt wedges can be deformed significantly within a tidal cycle, leading to fronts and internal controls [Dyer, 1997; Kay and Jay, 2003a; MacDonald and Geyer, 2005]. San Francisco Bay is not considered highly stratified, but portions of it may stratify intermittently [Monismith et al., 2002].

#### 1.5.3.2 Partially Mixed Estuaries

Tidal pumping is a vertically well-mixed process of along-channel salt transport that is independent of density-driven forcing. Two-layer exchange in highly stratified estuaries may be constrained by bathymetry, but it is driven by an along-channel pressure gradient pushing buoyant water over dense oceanic water. Partially mixed estuaries lie somewhere in between these extremes. Prandle [1985] defines this regime in terms of a stratification parameter.

$$S_t = \frac{0.85C_d U_{\text{tide}} L_{\text{estuary}}}{g'H^2 U_{\text{river}}} \quad (8)$$

$L_{\text{estuary}}$  is the length of the estuary,  $H$  is the depth of the estuary,  $C_d$  is a drag coefficient, and  $U_{\text{river}}$  and  $U_{\text{tide}}$  are the mean riverine and tidal velocities.  $S_t$  is a ratio of vertical mixing energy from bed shear to stratification caused by riverine buoyancy input. It is similar in function to the reciprocal of Fischer's non-dimensional estuarine Richardson number:

$$Ri_E = \frac{g' H U_{\text{river}}}{U_{\text{tide}}^3} \quad (9)$$

While these are only two of many estuarine classification schemes [e.g. *Hansen and Rattray, 1966*], the salient point is that all of the schemes involve a comparison between stratification caused by density-driven tilting of along-channel isopycnals and destratification because of vertical mixing from bed shear. San Francisco Bay as a whole is considered partially mixed, so a model of exchange will be considered that includes these stratifying and destratifying processes.

### 1.5.3.3 Estuarine Circulation

Estuarine or gravitational circulation is defined for a 2D channel by the following simplified along-channel momentum balance:

$$\frac{Du}{Dt} = -g \frac{\partial \eta}{\partial x} - \int_{-H}^0 \frac{g}{\rho_0} \frac{\partial \rho}{\partial x} dz + \frac{\partial}{\partial z} \left( K \frac{\partial u}{\partial z} \right) \quad (10)$$

where  $\eta$  is the water surface elevation,  $\rho_0$  is the mean density, and  $K$  is an eddy viscosity. Acceleration is forced by barotropic tides and an along-channel density gradient with mixing solely in the vertical direction. For steady velocity and a constant eddy viscosity:

$$\frac{g \frac{\partial \rho}{\partial x}}{K \rho_o} = \frac{\partial^3 u}{\partial z^3} \quad (11)$$

To solve for velocity as a function of depth, three conditions are applied: no-slip at the bed ( $u(-H) = 0$ ), free slip (no wind) at the water-air surface ( $\frac{\partial u(0)}{\partial z} = 0$ ), and constant mean flow from the estuary's freshwater source ( $\bar{u} = \frac{Q_{\text{fresh}}}{A} = \int_{-H}^0 u dz$ ). Normalizing depth with  $\xi = \frac{z}{H}$ :

$$u(\xi) = \frac{3}{2} \bar{u} (1 - \xi^2) + \frac{g \frac{d\rho}{dx} H^3}{48 \rho_o K} (1 - 9\xi^2 - 8\xi^3) \quad (12)$$

Chatwin [1976] extends this result to estimate how tidally averaged vertical shear and stratification vary along an estuary. This tidally averaged quasi-2D analytic model is a good place to start, but it is not sufficient for modeling along-channel exchange in estuaries. Lateral tidal processes, such as pumping and trapping, also contribute to along-channel salt dispersion. Hansen and Rattray [1965] suggest that dispersion from lateral tidal processes increases linearly from the head to the mouth. MacCready [2004] improves the ocean boundary of the Hansen and Rattray analytic model by explicitly incorporating the effect of tidal pumping on along-channel dispersion through extension of Stommel and Farmer's [1952] geometric jet-drain model at the estuary mouth.

#### 1.5.3.4 Strain Induced Periodic Stratification

In partially mixed estuaries, stratification varies throughout the tidal cycle. If stratification changes beyond certain thresholds, then the tidally-averaged estuarine circulation models in 1.5.3.3 are no longer applicable. In estuarine circulation,

stratification develops mainly from vertical shear forced by the along-channel density gradients. Additionally, stratification can be generated by the tides when shear from bed stress strains the along-channel density gradient. Extreme stratification asymmetries can develop in both tidal phases. During flood tide, the water-column can be overstrained [Nepf and Geyer, 1996], creating an unstable density structure that would cause rapid convective mixing. During ebb tide, stratification from tidal shear reduces vertical mixing, which can in turn produce more vertical shear. This feedback loop, termed runaway stratification [Monismith *et al.*, 1996], causes non-linear increases in exchange as a function of along-channel density forcing. Specifically, Strain Induced Periodic Stratification, or SIPS, occurs when:

$$\frac{1}{\rho} \frac{\partial \rho}{\partial x} > 2.2 \cdot 10^5 \left( \frac{U_e}{H} \right)^2 \quad (13)$$

where  $U_e$  is mean ebb tide velocity [Simpson *et al.*, 1990]. As with the other thresholds and parameterizations described in this section (1.5.3), equation 13 is derived from a comparison of stratification from an along-channel density gradient and vertical mixing from bed stress.

#### 1.5.3.5 Shoal-Channel Dynamics

Lateral bathymetry variations may also have density-driven influences on flow patterns, not just the laterally density invariant ones modeled by Hansen and Rattray [1965] and MacCready [2004]. Tidal currents move faster in channels than over shoals to minimize energy loss from shear. Due to the no slip bottom boundary condition, depth-average velocity is lower in shallow shoals than in deep channels. As a result of this velocity asymmetry and along-channel density gradients, channels develop higher density than

shoals during flood tide. This results in a secondary circulation, in which velocity is towards the center at the surface and shoreward near the bed. Nunes and Simpson [1985] observed a dramatic manifestation of this shoal-channel effect in the Conway Estuary, where an axial convergent front is maintained for several kilometers during flood tides. Valle Levinson and Kwiza [1995] observed and modeled axial convergence at the boundary between Chesapeake Bay and the Atlantic Ocean. Axial convergence and other density-driven lateral processes can generate stratification and alter shoal-channel exchange, influencing along-channel dispersion [Zimmerman, 1986].

### 1.5.3.6 Application to Salt Fluxes

Building on the discussion of hydrodynamics presented in earlier parts of section 1.5, the goals of this experiment that relate to  $X_2$  can be further refined. As mentioned in section 1.2,  $X_2$  is less sensitive to changes in Sacramento-San Joaquin Delta inflow rate to San Francisco Bay ( $Q$ ) than is predicted by any combination of estuarine circulation and tidal exchange models, so another process or processes must be controlling exchange.

Monismith et al. [2002] found that  $X_2$  is proportional to  $Q^{-2/3}$ , whereas estuarine circulation exchange scales as  $Q^{-1/3}$  and tidal exchange as  $Q^{-1}$ . The  $X_2$  to  $Q$  scalings follow from Hansen and Rattray [1965] and MacCready's [1999] descriptions of estuarine circulation flux and tidal flux as functions of the along-channel salinity

gradient,  $\frac{dS}{dx}$ :



$$\begin{aligned} \text{Est. Circ. Salt Flux} &= \frac{\alpha(g\beta)^2 H^8}{\nu_t^3} \left( \frac{dS}{dx} \right)^3 \\ \text{Tidal Salt Flux} &= K_H \frac{dS}{dx} \end{aligned} \quad (14)$$

where  $\beta$  relates salinity to density  $\left( .77 \frac{\text{kg}}{\text{m}^3} \text{PSU} \right)$ ,  $\alpha$  is an integration constant, viscosity ( $\nu_t$ )

is constant, and the turbulent Prandtl number is 1. Increasing  $Q$  reduces  $X_2$ , which

compresses the salt field. Compressing the salt field increases  $\frac{dS}{dx}$ , which by equation 14

increases the salt flux. Estuarine circulation salt flux scales as  $\left( \frac{dS}{dx} \right)^3$ , so  $X_2$  scales as

$Q^{-\frac{1}{3}}$  for this process. Tidal exchange includes non-density-driven processes such as tidal pumping. SIPS was presented as a process that may explain the scaling of  $X_2$  and  $Q$  in

San Francisco Bay, because it is a stronger function of  $\frac{dS}{dx}$  for the estuary as a whole than

either estuarine circulation or tidal exchange [Monismith *et al.*, 2002]. With SIPS,  $X_2$

would be less responsive to  $Q$  changes than by the two standard exchange mechanisms.

SIPS was observed in northern San Francisco Bay [Stacey *et al.*, 2001]. SIPS is more

likely to occur at the east end of Golden Gate Channel than at other locations in the lower

estuary because it is deep, and the threshold for SIPS to occur is lower in deeper places

(equation 13).

## 1.6 Summary of Project Goals

Exchange across mouths is important, because mouths serve as boundaries between

distinct water masses: estuarine and oceanic. However, exchange is often poorly

understood at these locations because of spatial flow variability over channel cross-sections and temporal variability over tidal cycles. By employing new technologies, this study aims to address the following questions:

- How does salt exchange between the Golden Gate and the coastal ocean?
- How does bathymetry influence residual circulation?
- How much does each forcing mechanism (e.g. tides, wind) contribute to residual circulation?
- How do exchange and residual circulation scale with seasonal factors such as river flow?

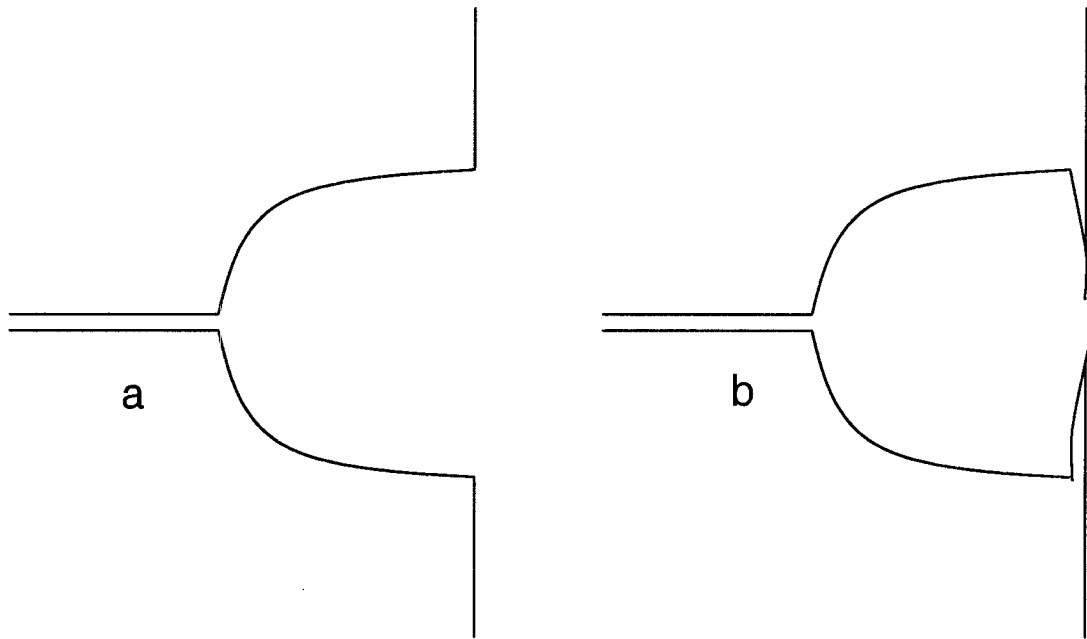


Figure 1.1: Schematic of wide and narrow mouths of bays

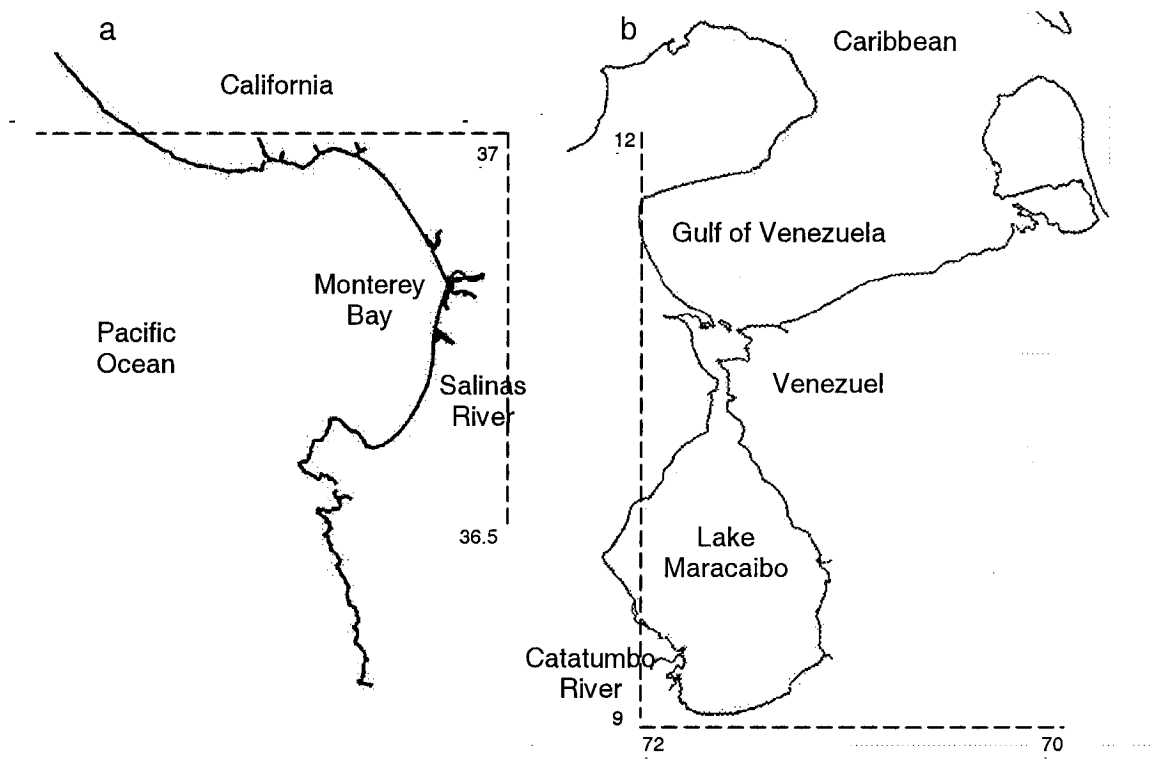


Figure 1.2: Examples of wide and narrow bay mouths

Figure 1.2a is the coastline surrounding Monterey Bay, California USA [data from [spo.nos.noaa.gov](http://spo.nos.noaa.gov)]. Figure 1.2b is the coastline of Lake Maracaibo, Venezuela [adapted from Redfield 1961].

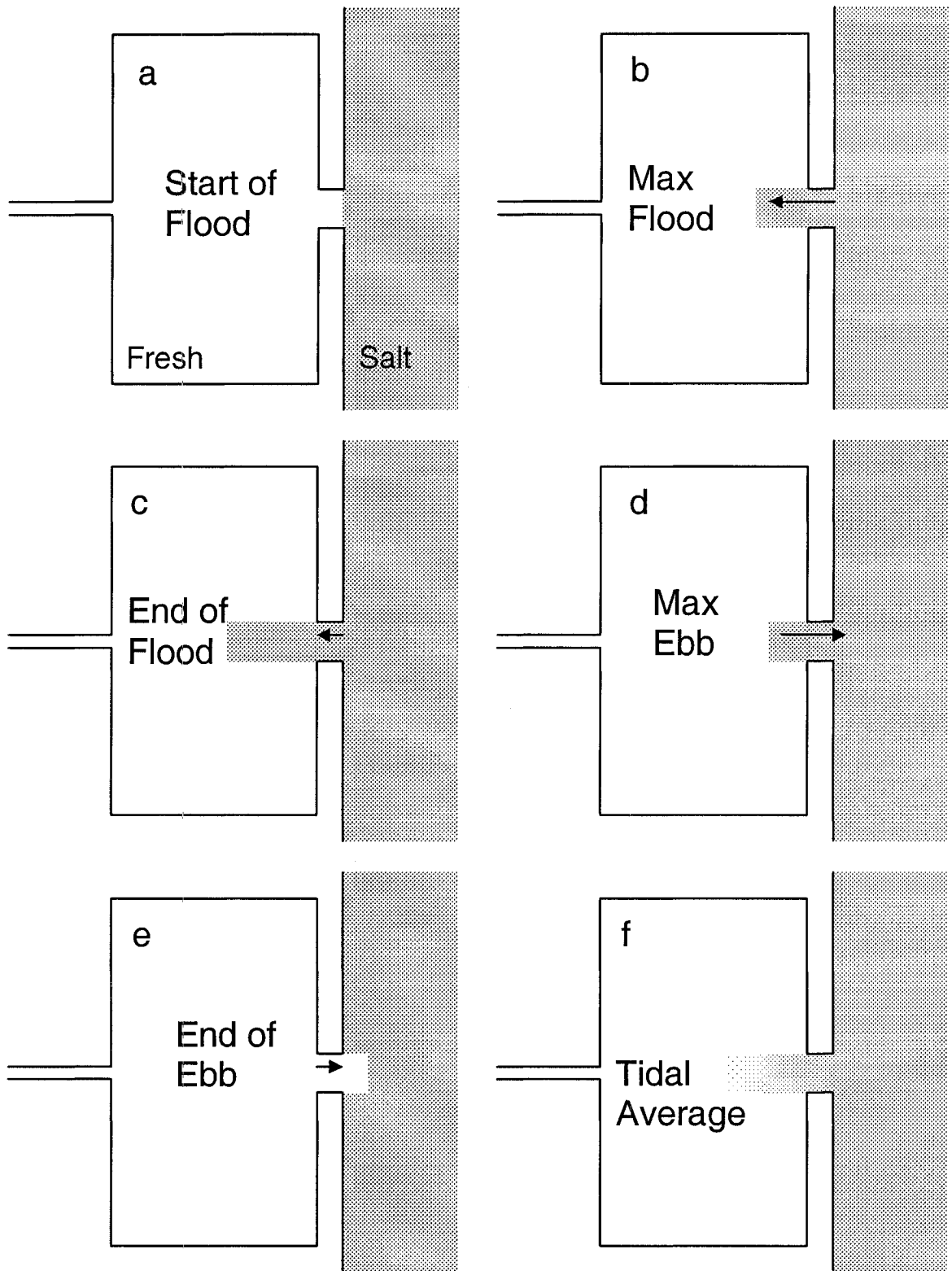


Figure 1.3: Schematic of a tidal system without mixing

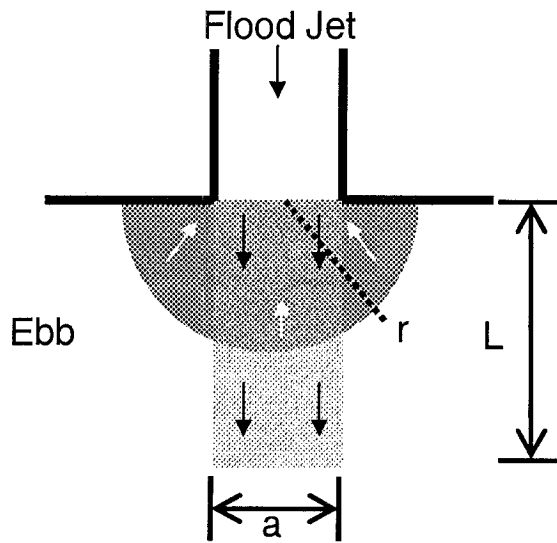


Figure 1.4: Tidal Pumping Schematic

The tidal pumping flow asymmetry is defined by a flood tide jet emanating from the channel and an ebb tide drain directed towards the channel center. 'a' is the jet width, 'L' is the jet length, and 'r' is the drain radius.

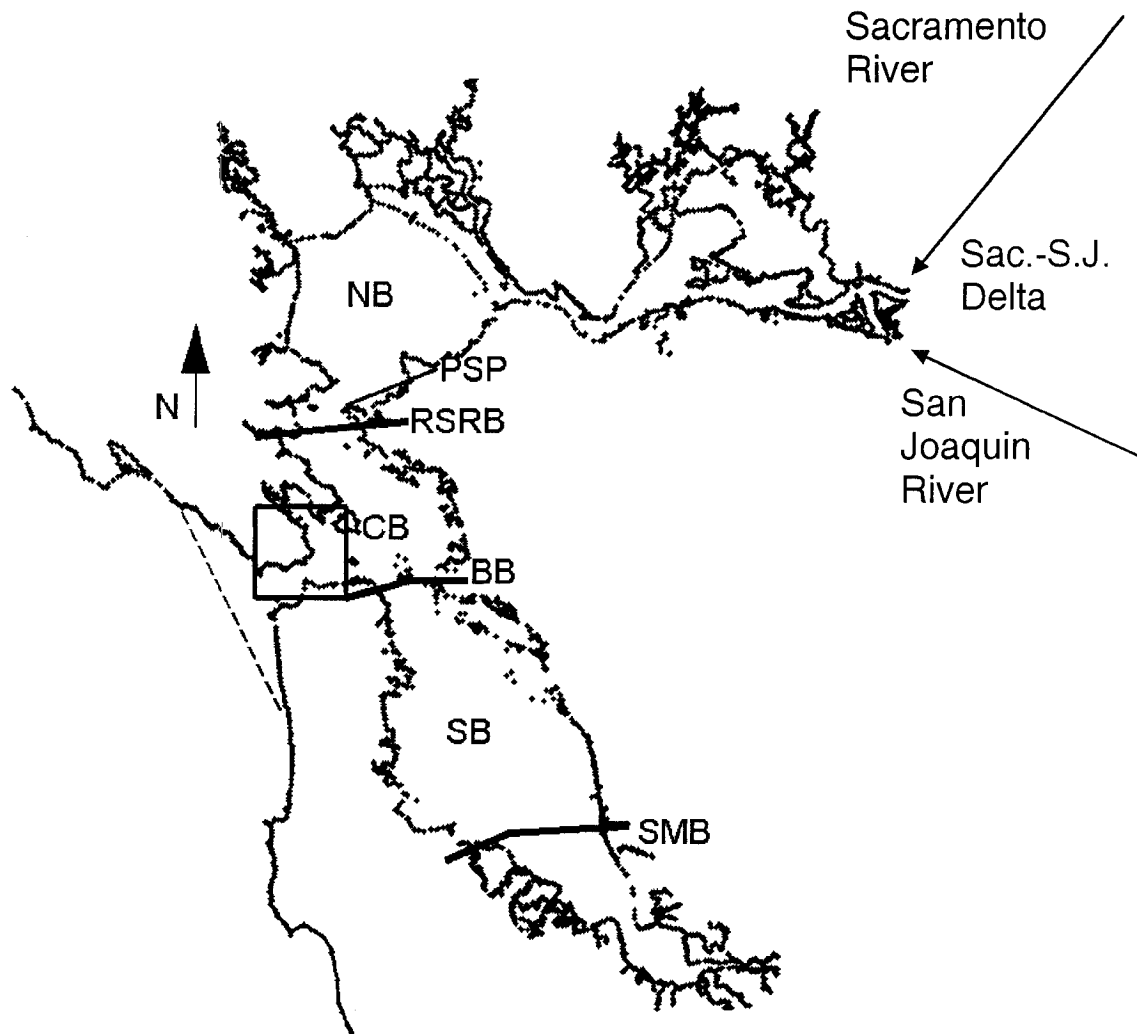


Figure 1.5: San Francisco Bay Region

The coastline of the San Francisco Bay region traces Central Bay (CB), North Bay (NB), and South Bay (SB). Central Bay is bounded on the north by Point San Pablo (PSP) and on the south by San Bruno Shoal, which is halfway between the Bay Bridge (BB) and the San Mateo Bridge (SMB). The Richmond-San Rafael Bridge (RSRB), the main river inputs to the bay, a box around the Golden Gate field site, and a dotted line marking the ocean boundary of a grid used in a numerical model are also included.

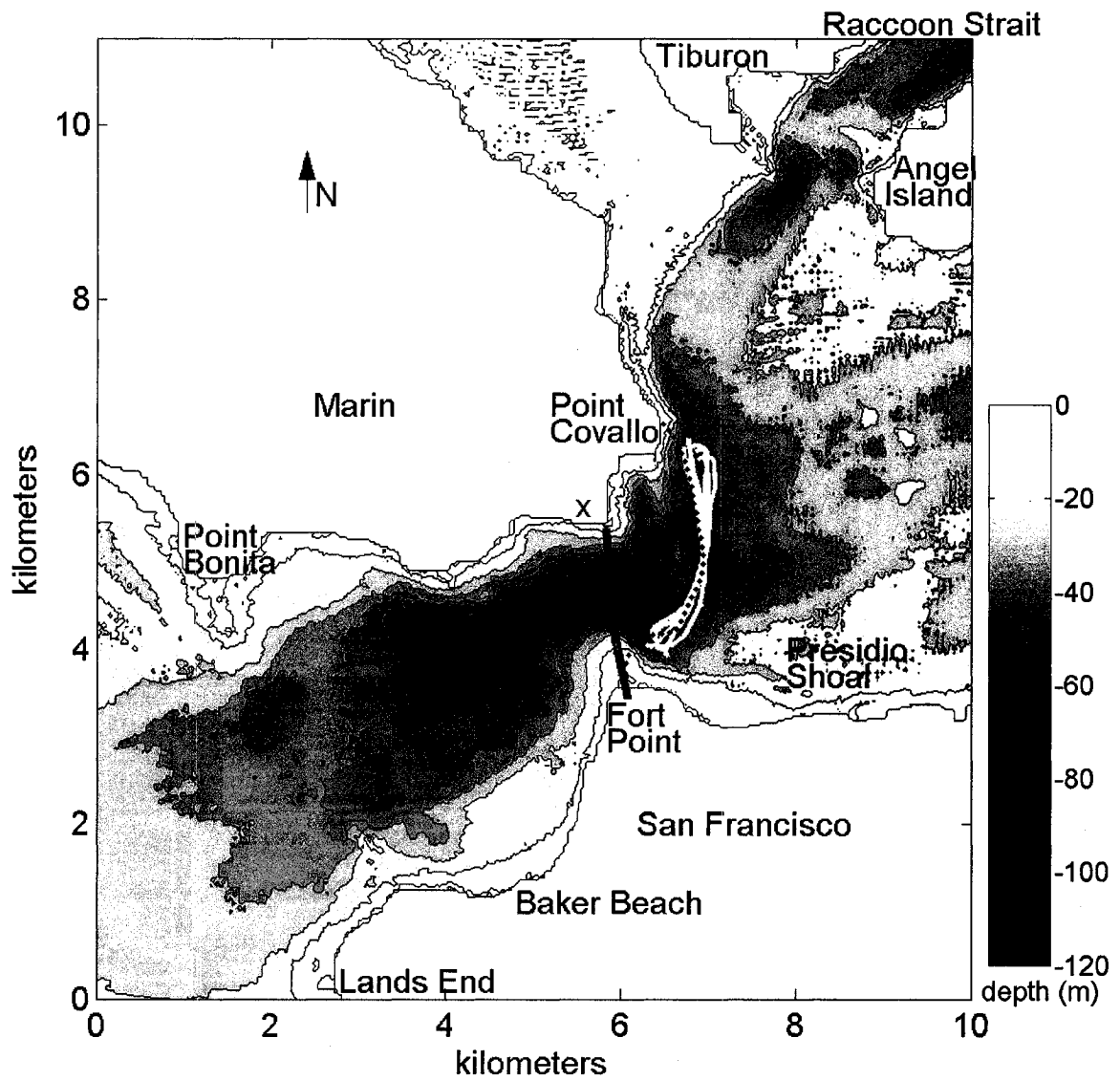


Figure 1.6: Golden Gate Channel Field Site

Shown are 10m bathymetric contours, the Golden Gate Bridge (red), the oblique photography location (green), several transects (yellow), and the grid path (the magenta dots connecting the transect paths to the shores). Note the sill adjacent the west side of the transect path.



## 2 Experimental Design

### 2.1 Field Site

San Francisco Bay is characterized by several subembayments (see figure 1.5); the South Bay consists of one large subembayment, the North Bay consists of two primary subembayments: San Pablo Bay and Suisun Bay. The two arms of the bay have distinctively different freshwater forcing, with North Bay receiving inflow from the Sacramento and San Joaquin Rivers and the South Bay receiving primarily wastewater effluent and small watershed returns. Each of these two arms connects to the coastal ocean through Central Bay. As a result, several water masses are mixed and exchanged through energetic tidal flows in Central Bay, a region bounded by the Golden Gate Bridge, Point San Pablo (2km north of the Richmond-San Rafael Bridge), and San Bruno Shoal (halfway between the Bay and San Mateo Bridges).

Many factors complicate analysis at the Golden Gate, including irregular bathymetry and variations in tides, river inflows, and oceanic density. The jagged topography at the Golden Gate (figure 1.6) indicates that the flows are likely to be characterized by complex spatial structure, with both vertical and lateral variability. Additionally, temporal variability is induced at the tidal, fortnightly, seasonal and inter-annual timescales. San Francisco Bay's tides are mixed between diurnal and semidiurnal components, with significant fortnightly variation [Walters *et al.*, 1985]. At the seasonal timescale, along-channel and vertical density gradients are modulated by a two order of magnitude change in freshwater inflow throughout the year. The temperature difference between the ocean and the rivers feeding the bay also varies annually, with cool water

pulses in the summer from ocean upwelling and cool snowmelt flowing down rivers at the end of winter. Together, these forcings suggest a flow environment with variability at a wide range of timescales.

## **2.2 Summary of Methodology**

A series of three experiments were conducted across the ocean-estuary interface of San Francisco Bay. Measurements were made of the variability of velocity, salinity, temperature, suspended solids, and chlorophyll on daily, fortnightly, and seasonal timescales. Each experiment extends over two diurnal tidal cycles and was repeated each season during both neap and spring tides. During each experiment, continuous transecting was performed across the landward side of the Golden Gate Channel. Surface water density and 3D water column velocity were measured from boat-mounted instruments. Scalar concentrations were measured from a towed profiler. Section 2.3 is a review of previous efforts to measure hydrodynamics around the Golden Gate. The instruments are described in section 2.4, their use in section 2.5, and ancillary data sets collected by others during our experiments in section 2.6.

## **2.3 Previous Golden Gate Exchange Experiments**

This is not the first attempt to measure exchange at the Golden Gate, and as will be described later, other research groups are planning to deploy new measurement technologies at the Golden Gate in the near future. Parker et al. [1972] performed the first major study of exchange at the Golden Gate. Salinity was measured along a transect path between the Golden Gate Bridge and Point Bonita for 12 hours during two days. At

the same time, ocean salinities in the Gulf of the Farallones were measured from another boat. Conomos [1979] reviews previous San Francisco Bay hydrodynamic studies, including his drifter experiment [*Conomos et al.*, 1971] that showed density-driven exchange at the Golden Gate. Surface drifters exited the bay while bottom drifters entered the bay. Conomos [1979] concludes that an investigation of the temporal and spatial variability of velocity and salinity at the Golden Gate is an important research need. USGS studies [*Walters et al.*, 1985; *Walters and Gartner*, 1985] on tides and currents in the whole bay include a description of Golden Gate exchange. Walters et al. [1985] outline the value of measuring scalar exchange through the Golden Gate. They present a simplified version of Fischer's [1972] flux analysis, and suggest that tidal pumping is the largest contributor to exchange. However, they note that instruments were not yet available to capture the Golden Gate's complex exchange dynamics. Since this study was completed both the USGS Menlo Park and Sacramento offices have helped to moor ADCPs, CTDs and other instruments at the Golden Gate (Cheng and Schoellhamer, pers. comm.). For example, the USGS maintained a station on the base of the south tower of the bridge for several years.

In a discussion of Golden Gate Channel hydrodynamics, Largier [1996] summarizes several velocity and salinity data sets collected west of the Golden Gate Bridge. Petzrick et al. [1996] moored an ADCP on the south side of the channel at 91m depth for five weeks. At this location the mean tidal velocity was  $23 \text{ cm s}^{-1}$  landward, 5 degrees north of east. Data from a single water column are difficult to interpret. As such, Petzrick et al. do not tie together reasons for cross-channel flow patterns and flow asymmetries. From data

taken over the entire cross-section, such as our 2002 and 2003 results, we determined that the tidal asymmetry in this moored ADCP data to tidal pumping in conjunction with channeling of the flood jet around the south side of the main sill.

NOAA moored an ADCP in each shipping lane 0.5 km east of our transect path for parts of the late 1990s. Stone and Bourgerie [1999] transected across the channel over these moorings 36 times over 12 hours. Their cruise was also on the USGS *R/V Turning Tide*. The focus of this experiment was to evaluate locations for two long-term ADCP moorings. Their analysis centered on transects near the southern mooring on Presidio Shoal. From their data, at maximum ebb the flow separates between Presidio Shoal and Fort Point. For a couple of hours after maximum ebb, water south of the separation line floods back past Crissy Field. Our transect path is at the north end of this separation zone, and thus our data set does not capture the effect of this feature on exchange. However, by looking at this area from the south side of the Golden Gate Bridge, the author of this thesis noticed a similar flow separation at maximum flood. Stone and Bourgerie did not transect at maximum flood. The net effect of these maximum ebb and flood features is unclear, although they do indicate a smaller than expected amount of tidal exchange through the Golden Gate via the south shoal. Stone and Bourgerie's experiment show how transect data can be used to interpret moored ADCP data. They recommend a more frequent transecting period than 20 minutes, which is the spacing between their transects.

## **2.4 Instruments**

### **2.4.1 Introduction**

Measuring net scalar flux requires water velocity and scalar concentration for the entire cross-section within a stationary time period. Although researchers have been able to make quick velocity transects from boat-mounted Acoustic Doppler Current Profilers (ADCPs) for many years, scalar fields have taken longer to sample because they are harder to measure remotely. Scalar concentrations across other estuaries have been measured by vertical profiles taken at several places across a channel and from arrays of moored CTDs [Bowen and Geyer, 2003, Lerczak pers. comm. 2005; Lerczak and Geyer, 2004]. However, this method would not be effective for characterizing scalar concentrations at many estuary mouths because of large cross-sectional areas and complex bathymetry. New towed instrument packages that can be flown through the cross-section vertically and horizontally along a sine wave path provide a fresh opportunity to examine the dynamics of these estuary mouths.

#### **2.4.2 Acrobat**

The SeaScience Inc. Acrobat is the new tool that distinguishes this experiment from previous ocean-estuary exchange studies (figure 2.1). It is a towed profiler that flies up and down in the water column as it is towed across the transect path (figure 2.2). Larger tow-yo profilers, such as the SeaSoar, are commonly used along the coastal shelf [e.g. Barth *et al.*, 1998]. The Acrobat and its predecessor, the Guildline Minibat, are designed for shallower environments. The Acrobat carries 10-15 kg of instruments, feeding real time data by way of its tow cable to the boat. Through a combination of manual and automatic control, the Acrobat profiles by adjusting wing pitch. Lift from the wings allows the Acrobat to dive down in the water column. Without its wings, it would skip

along the surface like a water skier because of cable and instrument drag. The cable is faired to reduce drag and strumming. The Acrobat must be towed at least  $4 \text{ m s}^{-1}$  to generate enough lift for diving. Typically, the Acrobat will vertically profile a meter for every ten horizontal meters it is towed.

The Acrobat is deployed and retracted with an electric winch, but it is tied off to cleats during profiling. Between cleats and tow cable, a rope-clutch system allows more line to be paid out in the event that the Acrobat snags on something, or if it tugs too hard on its cable (figure 2.3). The instrument relays its depth to the ship and responds to pitch change commands at one Hertz. It calculates the distance from the bottom by integrating water depth data from the boat's fathometer with its  $\sim 15 \text{ cm}$  accurate pressure sensor data, also taking into account the system's pay out distance behind the boat. As a result of these real time interactions, the Acrobat is in theory able to profile autonomously from the surface to just above the bed.

### **2.4.3 Acrobat Payload**

The Acrobat payload is based around a SeaBird 19+. The SeaBird measures conductivity, temperature, and depth (CTD). Three instruments were attached to the three external channels of the SeaBird: a D&A OBS-3 (optical backscatter), a Turner SCUFA (Self-Contained Underwater Fluorescence Apparatus), and a Licor 193SA spherical PAR (Photosynthetically Active Radiation). Real time scalar concentrations relay to the boat through the Acrobat's data cable via the SeaBird at 4 Hz. Four Hertz is the upper sampling rate for the SeaBird 19+ and its sensors. The external sensors are not

over-sampled. The SCUFA responds at 5 Hz, the OBS at 10 Hz, and the PAR at 100,000 Hz.

The Acrobat payload was positioned to minimize turbulence and bubbles in each instrument's sampling volume (figure 2.1). The SeaBird sensors faced upstream. Measuring photosynthetically active radiation, it was important to keep the Licor PAR unshaded. The PAR was mounted on the top of the Acrobat. OBSs quantify turbidity by measuring infrared backscatter off suspended particles. Its infrared beam projects perpendicular to its long axis, so it was mounted on the bottom front of the Acrobat with its sensor pointing downwards. Turner SCUFAs measure UVA fluorescence as a proxy for chlorophyll concentration. The SCUFA was mounted at the front so that it received undisturbed upstream flow. To balance the collection of instruments on the front of the Acrobat, a lead weight was mounted on the rear of the payload bay.

#### **2.4.4 Boat-Mounted Instruments**

The largest quantity of data collected during this experiment by over an order of magnitude was from an RDI 300 kHz ADCP (Acoustic Doppler Current Profiler). An ADCP measures 3D velocity in a water column. It possesses four acoustic transducers oriented 20 degrees apart. The ADCP calculates velocity at several depths based on backscatter received from pulsed signals emitted from the transducers. It cannot detect surface velocities, because the transducers are mounted under the surface to prevent surface reflections and bubble noise. Also, backscatter received from water too near the transducer heads is contaminated because the receiver needs to wait until the transducers

finish their pulses. Vertical side lobes of the transduced pulses interfere with the main  $20^\circ$  lobe for the bottom 6% of the water column, limiting near bed bottom accuracy. Higher frequency ADCPs can sample velocity at smaller depth intervals, but they also have less range. A 300 kHz ADCP has a range of 120m, 10m deeper than the lowest point in the Golden Gate Channel. Optimally, it should have been set to sample every 2m, but we sampled every 1m. Although this slightly increased measurement uncertainty, it will be shown later that there were much larger sources of uncertainty. The ADCP was set to send out and record an acoustic ping every second, which provided 4m horizontal resolution.

ADCPs also include a thermometer for calculating the speed of sound in water. A more precise temperature measurement was made by an RBR XR-420 CTD mounted adjacent to the ADCP (figure 2.4). The conductivity sensor on CTDs is sensitive to small bubbles, because it measures the conductivity of small parcels of water. The thermal sensor is less sensitive to bubbles, because it is a closed circuit with a resistor that changes resistance as a function of temperature. Backscatterance and fluorescence were not measured at the surface because of interference from entrained air.

ADCP results are biased by proximity to large ferromagnetic objects, such as the earth or steel boat hulls. Standard magnetic variation and compass calibrations were performed. The effectiveness of the calibration was verified by comparing GPS track and ADCP bottom track paths during transects.



### **2.4.5 Oblique Angle Photographs**

Surface features were imaged with a Canon PowerShot G3 4.0 Megapixel camera.

Oblique angle photography provides higher frequency views of larger surface areas than boat transects. Pawlowicz [2003] demonstrated this method's effectiveness in tracking surface convergence fronts, internal waves, and large eddies. The pictures were georeferenced with MicroImages TMIPS software.

## **2.5 The Experiment**

### **2.5.1 Three Seasons**

In a discussion of exchange mechanisms through the ocean side of the Golden Gate, Largier [1996] summarizes other salinity and temperature measurements made in this region and concludes that the dynamics of ocean-estuary exchange at the Golden Gate vary with three 'seasons' based on oceanic and estuarine conditions: upwelling, relaxation, and runoff. The runoff season is determined by conditions in the upstream watersheds and by the timing of peak flows. Upwelling refers to the coastal ocean season when strong northerly winds drive cool waters up to the surface along the coast. During the relaxation season in the fall the estuary's density field spreads to its longest extent and its isopycnals orient more horizontally and less vertically.

It is impractical to collect data during all conditions, so field campaigns were planned to occur at times that adequately span the time period of variability of the important physical processes. One field campaign occurred during each season. However, there is variability within each season, as well as annual variability. Flow during the

winter/spring runoff season peaks for a few days to a week after each storm. During the spring part of the runoff season, flow is generally less variable and higher because a large portion of the runoff comes from snowmelt instead of rain. Scheduling sampling during spring rather than winter gave us the best chance of measuring a high flow period. Total seasonal runoff and the annual peak flow vary by more than an order of magnitude [Conomos, 1979, <http://ca.water.usgs.gov>]. The annual variability correlates well with the El Niño cycle, with higher flows and warmer oceanic waters during El Niño. El Niño did not occur during the years of this experiment, which limited the range of conditions that could be measured. Freshwater input drops slowly during the summer, because there are usually no major storms in the watershed after spring. However, storms continued into the May (5/3/03) before our summer experiment. Summer upwelling is episodic, usually lasting a week or two at a time. The cycle of northerly winds that cause upwelling cannot be predicted long enough in advance for us to schedule a field campaign during an upwelling episode. In contrast, tidal patterns are well known (<http://co-ops.nos.noaa.gov>). The diurnal tidal magnitude (K1 and O1) is about equal to the semidiurnal tidal magnitude (M2, S2, and N2) at the Golden Gate, so sampling should occur over an entire day to span typical tidally variability [Walters *et al.*, 1985]. Similarly, there are significant spring-neap differences, so there should be at least two days per campaign to span fortnightly tidal variability. Spring-neap differences are slightly enhanced around the solstices. Also, they often alternate between strong and weak spring-neap differences for several months at a time. The monthly high in spring-neap difference is not consistently correlated with either the full or the new moon.

The spring experiment is described in two parts. The first half of the experiment focused on testing and refining our methodology. The methodology will be described in detail to lay out the limits of the Acrobat for this type of experiment. Acrobats, which have been sold only for a few years, are usually operated in shallower areas with smoother bathymetry and milder currents. Data related to hydrodynamics were collected during the second part of the spring experiment.

### **2.5.2 Field Testing**

Our first experiment at the Golden Gate commenced in the rain on March 6, 2002 during spring tide. The initial plan was to transect along a box with its landward side at the Golden Gate Bridge and seaward side several kilometers seaward, near Point Bonita and Lands End (figure 1.6). The main advantage of this method is the ability to directly measure along-channel properties, such as the along-channel density gradient. Measuring at two cross-sections would also uncover how exchange varies along the channel. Along-channel transects would be useful for resolving headland eddies [Geyer, 1993], and they would be vital for the measuring the effect of hydraulic controls [Farmer and Armi, 1999], however, it is possible to test for the existence these features with just one well-placed cross-section transect path. The box transect plan did not work. Firstly, it would have only allowed hourly sampling at every location at best, and the currents appeared to change too much at this time scale to achieve our goals. Secondly, data collected at the sides of the box would not have been particularly useful. Thirdly, it would have been hard to fly the Acrobat on the sides without hitting one of the many rocks and shoals.

It also proved impractical to measure as far seaward as originally planned. The area between the Golden Gate Bridge and the ebb bar seaward of Point Bonita is referred to locally as the 'potato patch' because ship cargo, such as sacks of potatoes, used to bounce into the water there due to high irregular waves. Waves shoal and sometimes break over the ebb bar, then interfere with each other as they propagate landward. It proved too rough for our vessel, so we moved underneath the bridge. Much of the wave energy is reflected or dissipated by the headland between Baker Beach and Fort Point (figure 1.6), although some of the wave energy makes it across the bay to Richmond [Talke and Stacey, 2003]. The transect path allowed us to turn in relatively protected waters. However, it took the boat over 100m deep water, which was twice as deep as the Acrobat could profile. Furthermore, the transect path was only two kilometers wide. The Acrobat has a 500m turning radius with 200m of cable paid out, so half the transect time was spent turning. Finally, at 12:30pm on March 7<sup>th</sup>, the Acrobat struck a shoal adjacent Fort Point. The wing broke, marking the end of the spring tide portion of the spring season experiment.

March 12<sup>th</sup> was spent experimenting with different boat speeds, pay out lengths, transect paths, and a newly acquired Acrobat wing. The optimal boat speed is as fast as possible. The faster the boat speed, the deeper the Acrobat can dive. However, towing too fast puts too much tension on the tow cable, which is gauged by slipping of the rope clutch. This proved to be the limiting factor on tow speed, but the ADCP would not have been able to locate the bottom effectively at much higher speeds. Transecting was performed at  $4 \text{ m s}^{-1}$  with respect to the surface water velocity in the transecting direction. Long pay

out lengths allowed for deeper diving, but also made for wider turning radii.

Furthermore, cable drag increases with pay out length, reducing the maximum diving depth. We determined an optimal pay out length of 200m of cable.

The Acrobat does not follow the boat track during turns (figure 2.5). Instead, drag makes it move in the direction it is being pulled by the tow cable. The Acrobat thus takes a shorter slower path during turns than the boat. Without tension in the tow cable, the Acrobat plummets downward. Diving during turns limits how close an approach to the shore on either side of the transect path can be taken. To mitigate this problem, the Acrobat was brought to the surface at the beginning of turns. The dive was used to get it near, but still above, the bed at the end of each turn. Turns were made into, not away from, the mean tidal currents because the Acrobat dives during turns (figure 2.6).

Speeding up the boat during turns seemed promising at first, but it led to sudden yanks on the tow cable, and it required exceptional timing between the Acrobat and boat operators.

Finally, a transect path was chosen (figure 1.6). It follows a 55m isobath. It is as perpendicular the mean flow direction as possible. The mean flow direction was estimated from NOAA navigation charts. Balancing this goal was the need to turn in deep water as close to the shore as possible. The south end of the transect path is between two shoals (Fort Point and Presidio Shoal) and the north end is behind a headland (Point Cavallo). 23 ADCP transects without the Acrobat were taken along this transect path on March 12<sup>th</sup>.

### **2.5.3 Spring 2002 Neap Tide**

Continuous transecting was performed for 12.5 hours on March 13<sup>th</sup> and 14<sup>th</sup>, 2002, on the USGS *R/V Turning Tide*. The boat was steered manually. In later experiments, the boat's navigation system was integrated with GPS, so it transected on autopilot. Under manual control, the boat followed a less consistent transect path. Large transect path deviations occurred about every two hours when cargo ships passed through the Golden Gate. The Port of Oakland is the fourth largest commercial shipping port in the United States with over 2 million containers passing through it a year (<http://portofoakland.com>). While the bulk of large vessels traveled to and from Oakland through the Golden Gate's southern shipping channel, occasional oil tankers and cargo ships took the northern channel, presumably to and from an oil pier or the Port of Stockton. To accommodate these large ships, the *R/V Turning Tide* would extend the transect path north past Point Cavallo towards Raccoon Strait (figure 1.6). Smaller vessels did not necessarily require the *R/V Turning Tide* to change course, however, their presence required constant monitoring and frequent negotiation. The large tourist vessels from Fisherman's Wharf were particularly intransigent, nearly clipping our tow body on several occasions. Kite boarders and wind surfers, who crisscross the channel every afternoon, also came dangerously close to the tow cable. Sailors of small sail boats seem to have a lot of trouble controlling their direction of travel around the Golden Gate. While its effect cannot be quantified, vessel traffic clearly eroded our stamina for transecting.

The Acrobat did not operate as autonomously as advertised. The most time consuming problem was instability as it profiled downwards, as shown in figure 2.7. For example, at 14:47:30 the Acrobat descends smoothly downward, adjusting its wing angle as it falls.

At 14:48:05 it dips steeply downward for a few seconds. The Acrobat responded by tilting up its wing, but it overcompensated. After a few seconds it tilted its wing steeply downward, leading to oscillating flight. Instabilities such as this one tended to amplify, resulting in hard tugs, which caused rope clutch slippage. In this case, the wing angle was stabilized manually by limiting the minimum (most negative) wing angle. This usually damped out the oscillations. Then the Acrobat was brought down by slowly increasing the minimum wing angle. In this case, the Acrobat had a surprising non-linear reaction to a one degree expansion of the minimum wing angle. At 14:49 it dropped 8 meters in 8 seconds despite a  $10^\circ$  wing angle response. It is unclear why this occurred. Our immediate response was to fly conservatively, which meant not flying within 10 meters of the bed.

The Acrobat's instability was used to mitigate the Acrobat's main problem: lack of range. The Acrobat was designed to dive from 0 to 60 meters, but we were only able to maintain a reliable profile in a 30 meter range during the spring experiment. Frequently, instability was intentionally induced to get the Acrobat down lower. It appeared to fly less effectively when subject to large cross-flows and large turbulent eddies. Without tilt sensors, it is unclear how these strong flows altered the Acrobat's orientation, reducing its efficiency. The widest vertical range was achieved by flying it between 15 meters and 45 meters below the surface.

Sixty-six transects were completed both March 13<sup>th</sup> and March 14<sup>th</sup>. The Acrobat was at or near the surface during the first and last transects of each day.

#### 2.5.4 Fall 2002

The fall 2002 experiment took place at the very end of the fall season. Fresh water flow from the delta is usually relatively constant and low during September and October because little rainfall occurs in California during these months, snowmelt tapers off, and there are smaller agricultural return flows and water demands at the end of the growing season. The water year as designated by USGS starts October 1<sup>st</sup>, which is typically a month or two before the first winter storm. In 2002, the first winter storm started a few hours after the end of our fall experiment on November 7<sup>th</sup>.

Several equipment upgrades were made between the spring and fall season experiments. The aluminum temporary wing used on the Acrobat March 12<sup>th</sup>-14<sup>th</sup> was replaced with a new wood composite wing. The new wing increased stability and expanded the profiling range by five meters. A new navigation system steered the boat around the transect path on autopilot. The new navigation system combined with a new radar system allowed for transecting at night and in fog. Fall experiments were conducted for 25 hours (dawn to dawn) on October 29<sup>th</sup> and November 6<sup>th</sup> (table 2.1).

	ADCP & Scalar	ADCP & Scalar	ADCP only
Spring '02	72.28-72.75	73.26-73.75	71.47-71.64
Summer '03	154.24-155.10	161.22-162.31	
Fall '02	302.25-303.35	310.24-311.34	

Table 2.1: Sampling Times (in year days)



Three times during each 24-hour experiment the tow body was pulled up so the boat could stop for surface-to-bed CTD-OBS profiles (figure 2.8). Three Niskin water sample bottles were attached to the profiler's cable. They were triggered to close by a series of messenger weights that slid down the cable. Water samples are used to calibrate the OBS to sediment concentration values and UVA fluorescence to chlorophyll concentration values. It took one to two hours to perform two profiles, one at the north side and one at the south side of the transect path. While the tow body was on deck, the *R/V Turning Tide* was driven to each shore, with the goal of characterizing the velocity field in the normally unsampled edges of the cross-section. It took one slow (~20 minute) transect to reel in or deploy the Acrobat with the electric winch.

The Acrobat proved vulnerable to impact from floating objects. A floating bull kelp (*Nereocystis luetkeana*) stipe wrapped around the tow cable at the surface, slid down the cable, and impacted the tow body. It appears that this impact made the Acrobat's tow bar act as a scissor with the tow body on the main data cable, at a point just after the data cable splits from the weight bearing portion of the tow cable. About an hour of profiling was lost fixing the broken cable. Tying the loose cable more restrictively would have avoided this problem.

One hundred twenty spring and one hundred twenty one neap transects were made during the fall experiment. The fall transect path is longer than the spring transect path. It extends about 250m further north. Extending the boat track northward was important,

because much of the ebb flow into the channel comes from the northeast through Raccoon Strait.

### **2.5.5 Summer 2003**

In addition to continuous ADCP tow-yo transect, continuous photographs were taken of the field site from above. Much of the first day of the experiment, June 2<sup>nd</sup>, was spent finding the best vantage point. A close up view was accessible from the deck of the bridge. However, for georeferencing the images it was necessary to have several landmarks in each picture. From underneath the lone tree in the headlands northwest of the bridge, one could see the north side of the transect path and several landmarks (figure 1.6). Unfortunately, fog enshrouded the headlands and the bridge during most of the afternoon of June 2<sup>nd</sup>. A full day of pictures was taken June 10<sup>th</sup>, except for three hours in the afternoon while a battery problem was addressed. A picture was taken every two minutes.

As before, the Acrobat briefly stopped working. A connection between the T-cable and the wing control box failed due to repetitive strain. The loss of the T-cable resulted in a six hour loss of Acrobat data on the morning of June 3<sup>rd</sup>. The ADCP continued profiling for two hours after the T-cable failure. One hundred twenty one neap and eighty two spring transects were made during the summer experiment.

## **2.6 Ancillary Data Streams**

Several ongoing monitoring programs provided data on properties that influence Golden Gate exchange. There are five active NOAA tide gauges in San Francisco (<http://co-ops.nos.noaa.gov>), including one on a pier just southeast of the transect path.

Meteorological data for San Francisco is available from the National Climate Data Center (<http://www.ncdc.noaa.gov>). United States Geological Survey measures the flow of the rivers feeding the bay (<http://ca.water.usgs.gov>), conducts monthly water quality surveys along the estuary, and maintains CTDs throughout the bay (<http://sfbay.wr.usgs.gov>). The USGS CTDs either moored on or adjacent to Presidio Shoal since 1990 are of particular relevance to this project. The California Department of Water Resources catalogs delta outflow and X2 (<http://www.iep.ca.gov>). The University of California at Santa Cruz processes and provides SeaWiFS and other satellite data (<http://oceandatacenter.ucsc.edu/>). Solar radiation for calculating evaporative fluxes is measured for the FAA at the San Francisco Airport (<http://www.ll.mit.edu/Aviation/Weather>). On the final day of the fall experiment, a series of CTD casts at the Golden Gate were done from the *R/V Point Sur* as part of a Naval Postgraduate School class that was collecting data for an intermittent long-term coastal monitoring program [CalCOFI <http://www-mlrg.ucsd.edu/calcofi.html> and *Collins et al.*, 2002].

## **2.7 Conclusion**

One theme present in reports and papers describing Golden Gate experiments is that this has been a difficult place to study. The 16th and 17th century ocean-going explorers of the west coast completely missed San Francisco Bay, most likely due to a combination of

fog and rough seas around the bay's ebb bar. When Sergeant Jose Ortega finally discovered this channel by sea in 1769, more than 200 years after Sir Francis Drake's first voyage to the region, the currents proved too hard for him to navigate into the bay. Challenging oceanographic conditions have kept many questions unanswered about Golden Gate exchange and circulation. Some of these questions will be answered in the following chapters, and plans for answering the others will be presented in the last chapter.

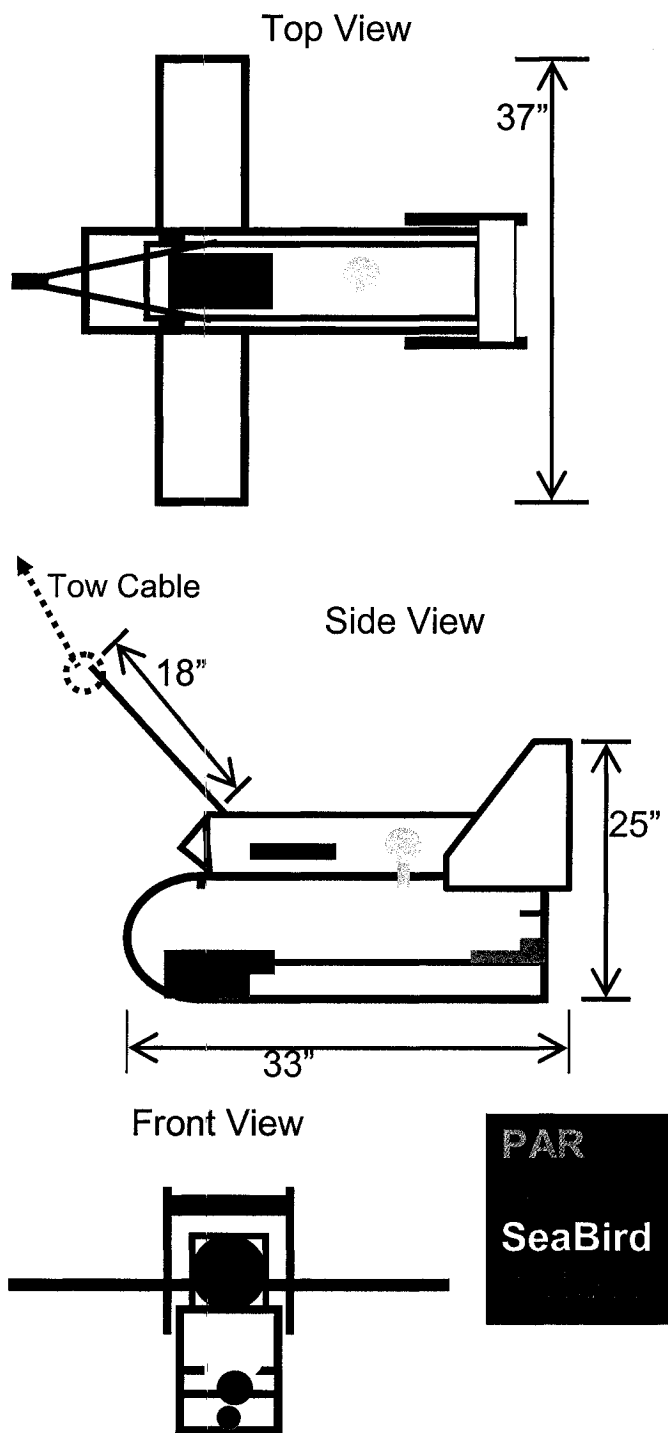


Figure 2.1: SeaSciences Acrobat

Instruments mounted on the SeaSciences Acrobat measure photosynthetically active radiation, optical backscatter, UVA fluorescence, salinity, temperature, and depth.

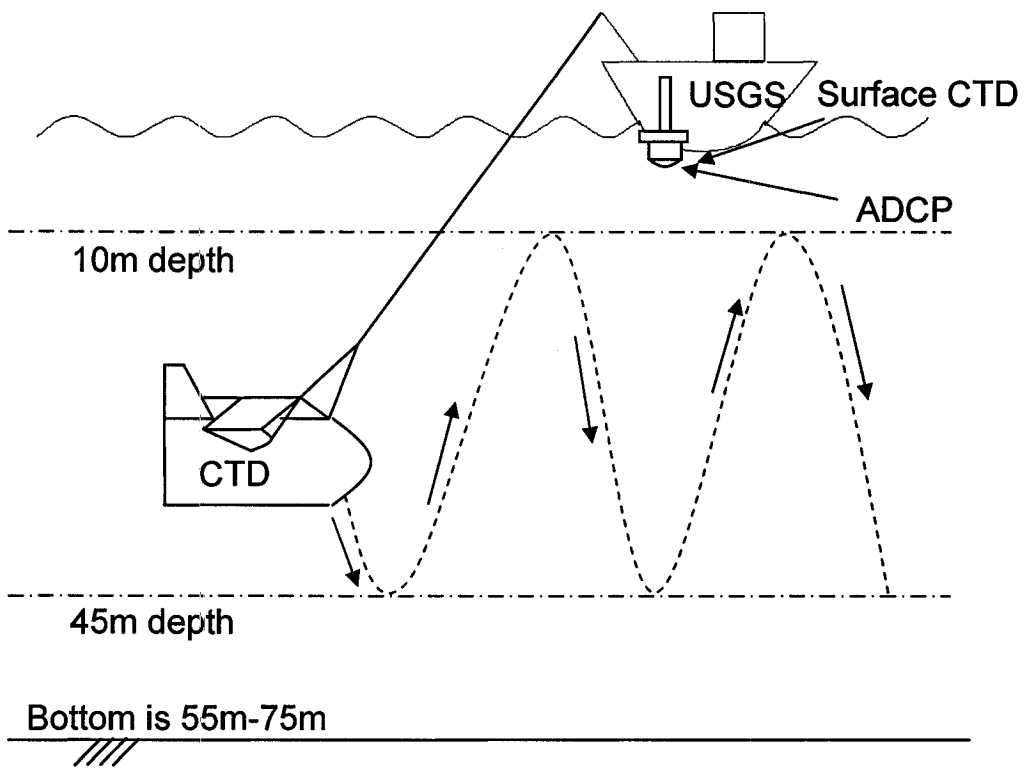
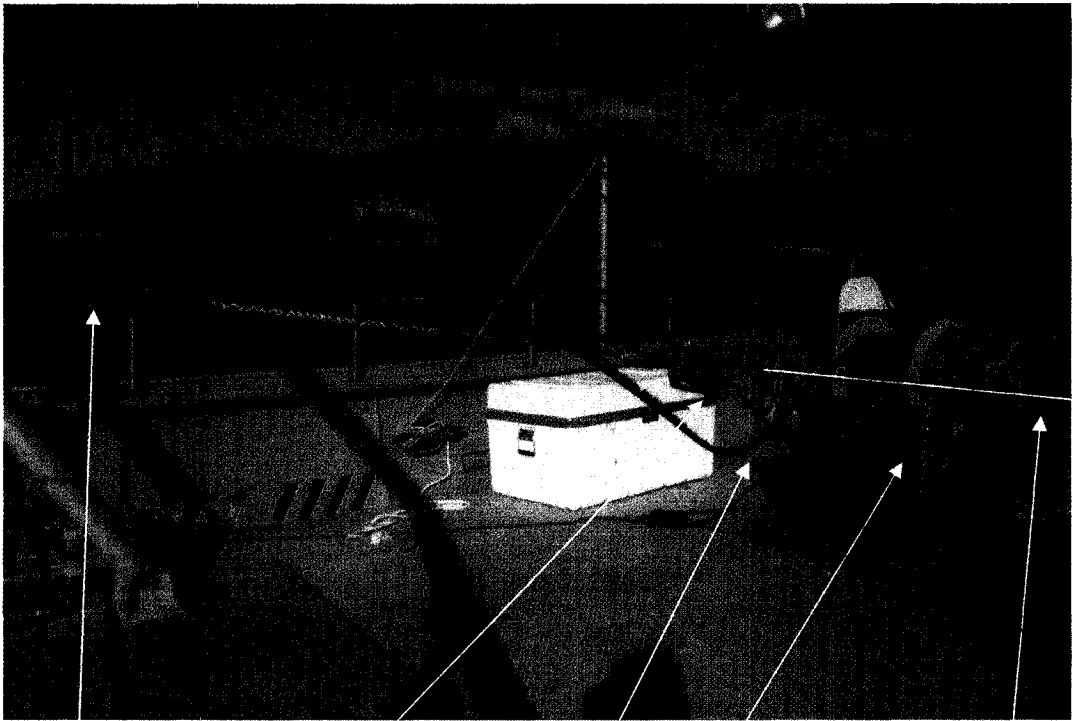


Figure 2.2: Tow-yo Profiling Schematic



Tow-cable under tension

Rope clutch

Tow-cable without tension

Winch

Line from clutch to cleat

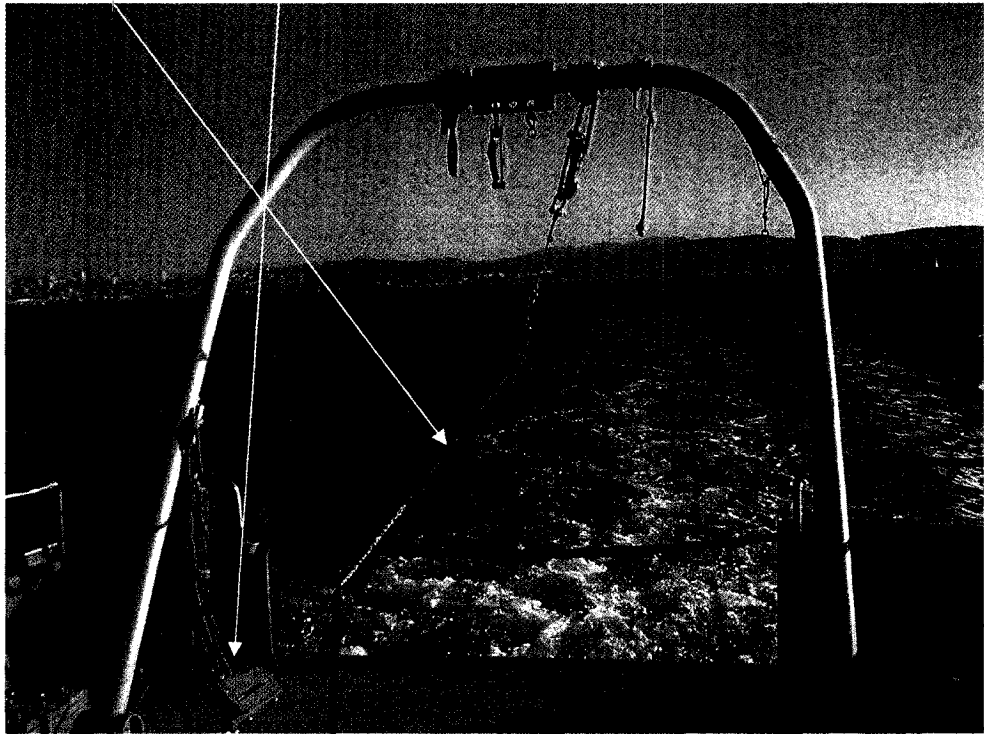


Figure 2.3: Rope-Clutch System

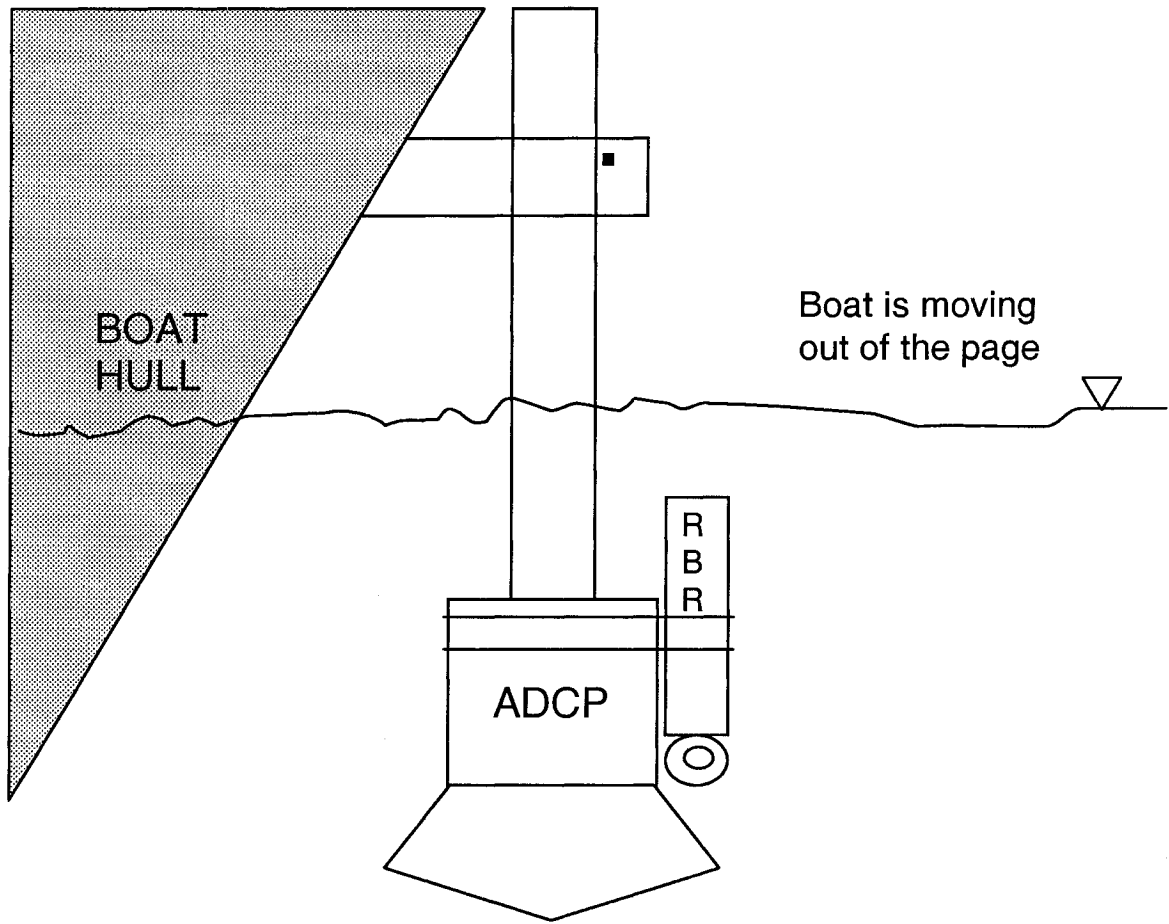


Figure 2.4: Boat-Mounted Instruments



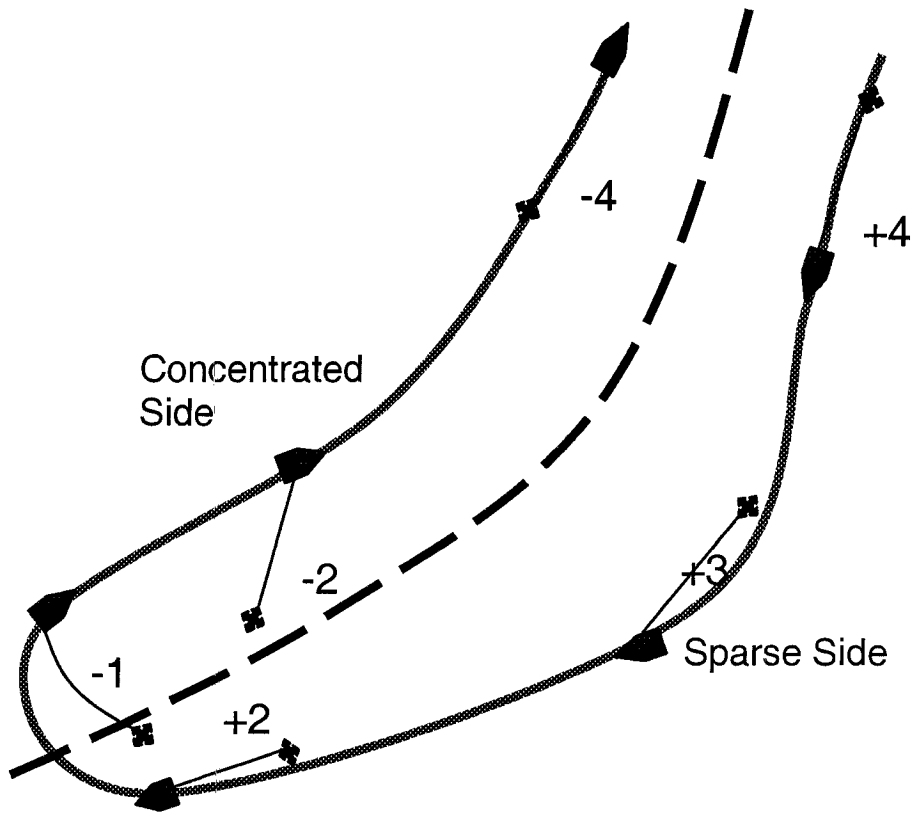


Figure 2.5: Tow-Body Location

The Acrobat does not follow directly behind the boat during turns. Before and after turns it is 200m or four 50m grid cells behind the boat. The integers in the figure are the grid spacing between the boat and the Acrobat (section 3.3). Turning reduces cross-transect data concentration leading into turns and increases concentration coming out of turns.

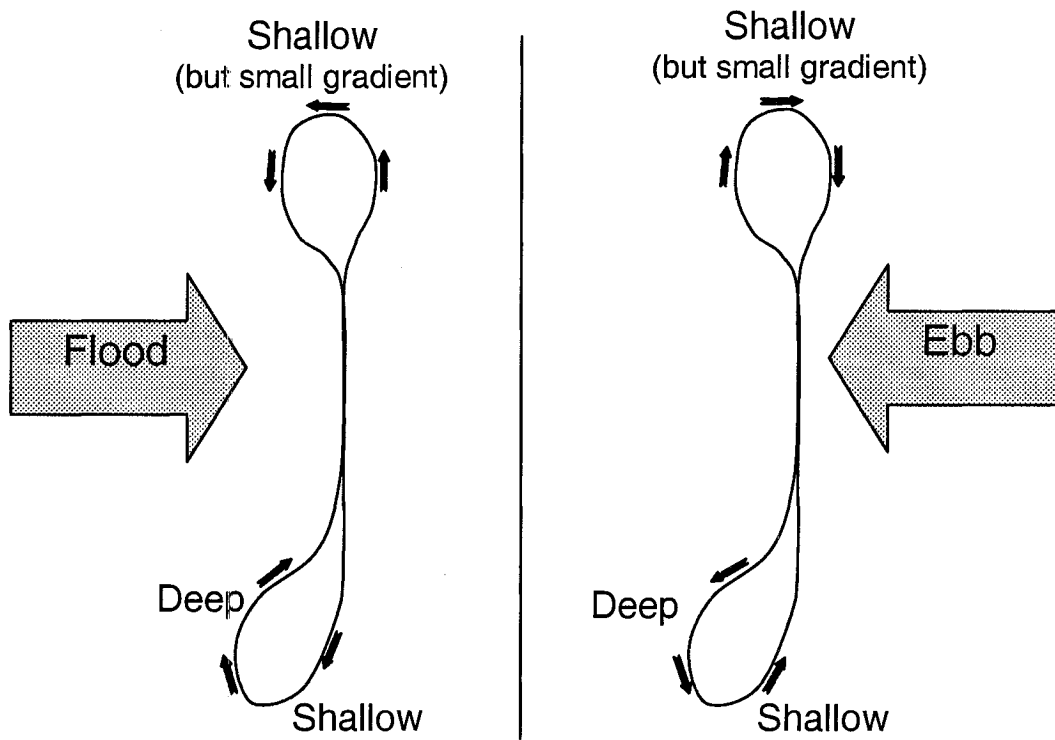


Figure 2.6: Turning Into the Tide

The boat was always turned into the tide to prevent the Acrobat from dropping to the bed during turns.

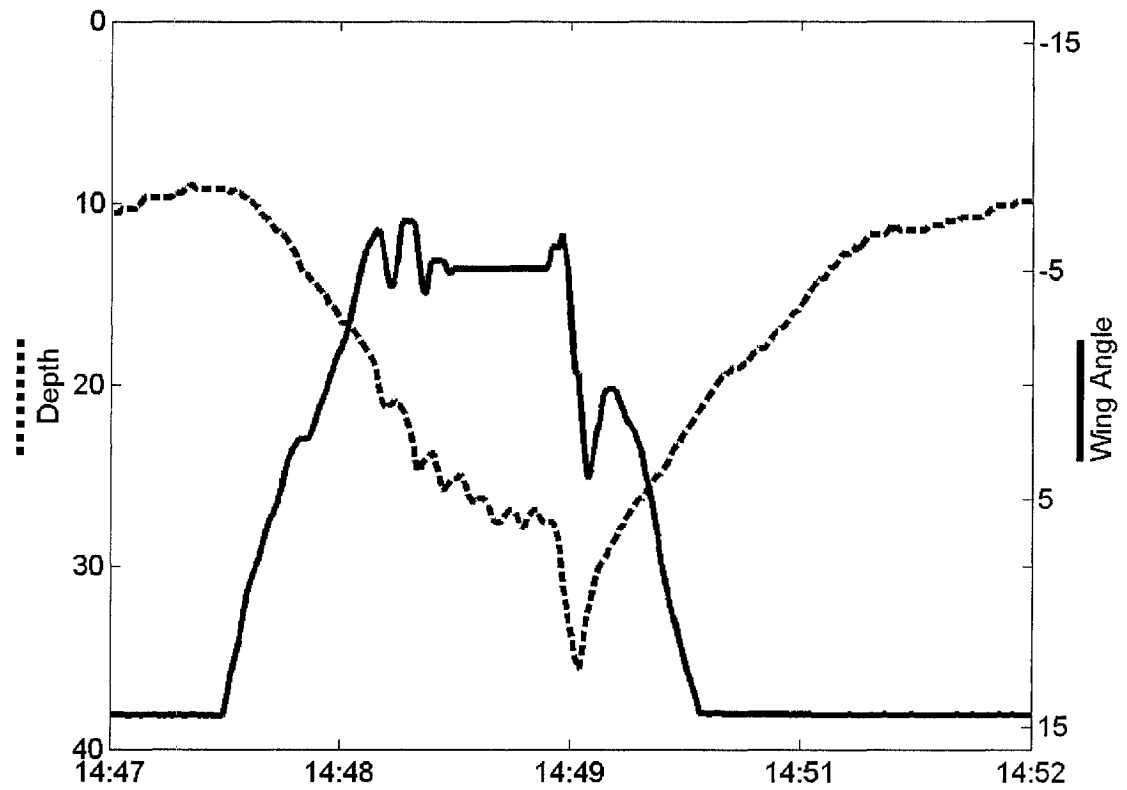


Figure 2.7: Acrobat Instability

The depth of the Acrobat is changed by adjusting its wing angle. The Acrobat glided less stably as it descended. During the dive shown in this figure, the Acrobat dips suddenly at 14:48:50.

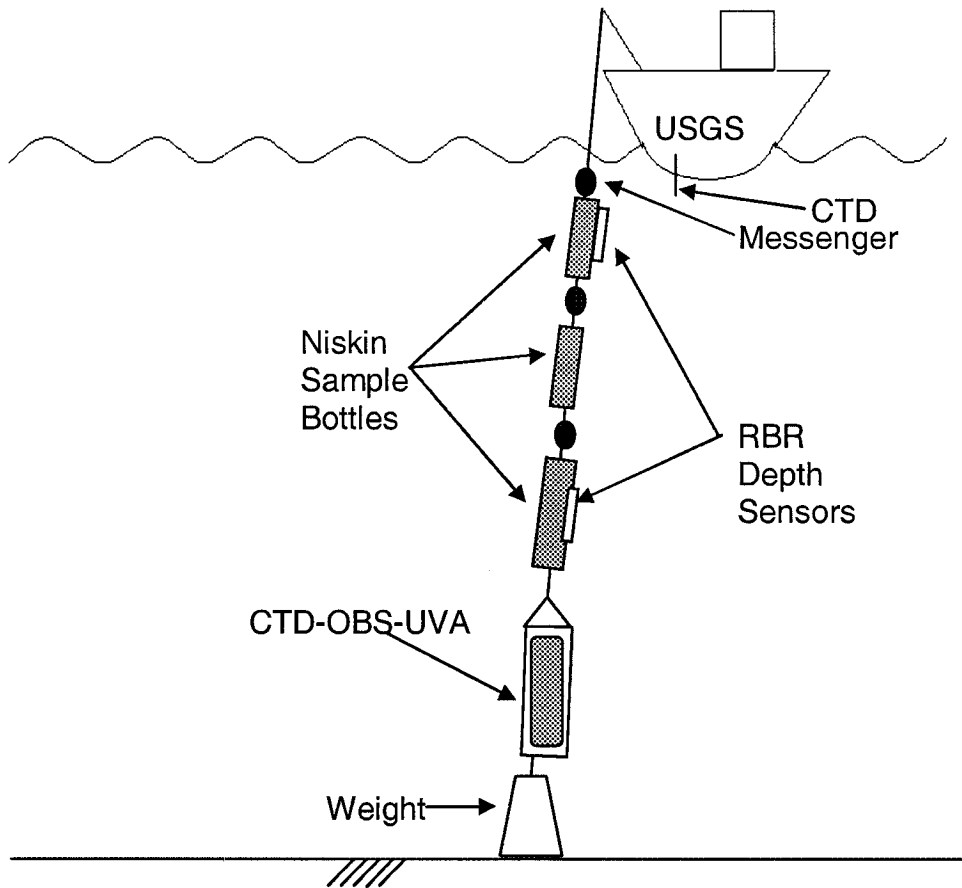


Figure 2.8: Vertical Profiling Schematic

## 3 Characterizing Flow and Exchange

### 3.1 Introduction

This chapter lays out the basic approach to analyzing the data collected by methods described in chapter 2. It will show how the continuous transect data have been transformed into discrete 2D snapshots that can be used to support explanations for Golden Gate circulation patterns. The analyses in chapters 4 through 6 build from the results of this chapter.

### 3.2 2D Grid

The average transect route for this experiment is not a straight cross-channel path (figure 1.6). Instead, it arcs with the intention of following residual isopycnals created by the jet-drain pattern. It ends at our closest shore approaches. The southern end is seaward of the northern end to make the turns in as deep water as possible. Data are projected onto a grid along the mean boat path using cylindrical coordinates with depth as the axial coordinate. Grid cells average  $2.05^\circ$  apart with UTM coordinate (54630m, 4186300m) as the center of the grid coordinate system (figure 3.1). This results in 50 meter average grid spacing. Defining the grid cells by angle instead of by distance makes the flow through the cells relatively similar. The southern cells would have less flow pass through them if the grid cells were defined by a constant 50m width, because the southern end is more arced away from the mean flow direction. Each grid cell includes 10 to 15 ADCP profiles. Inaccuracies in the ADCP's tracking of the bed velocity with respect to the boat vertically correlate the velocity data, so it is important to average horizontally over

several measurements. The grid is 66 cells long, or 3300m, with cell 1 on the south shore and cell 66 on the north shore.

Vertically, the grid spacing is 1 m. It spans from 3 meters above mean lower low water (MLLW) to one of four bottoms. The 19-year tidal range is 2.7m above MLLW to 0.8m below MLLW, with excursions of up to a couple decimeters by winter storms. The Golden Gate Channel has steep rocky sides, so the shore side of each turn is in shallower water than the channel side. Thus, the North-to-South bottom track is different than our South-to-North bottom track. The *R/V Turning Tide* was turned into the current to keep the Acrobat from diving, so the North-to-South and South-to-North bottom differences switch when the tide goes from flood to ebb. The routes taken on each transect can be grouped into North-to-South ebb, North-to-South flood, South-to-North ebb, and South-to-North flood transect tracks. The depths of the four bottom tracks for cells 11-60 are within five meters of each other near the shoals and are almost identical to each other in the center of the channel. Cells 11-60 are significant because those are the cells with data for most transects. The four bottoms are more similar to each other in the fall and summer datasets than in the spring dataset because the improved navigational system allowed tighter turns closer to shore.

### **3.3 SeaBird Gridding**

Gridding SeaBird data required estimation of the distance along the grid path of the instrument package behind the boat. This distance is 200m in the middle of the channel, but less when the boat starts turning (figure 2.5). The distance behind the boat was

estimated during turns for all turns based on average turn path and estimated tow cable angle. Pictures of the tow cable angle from the boat were taken, but the results were difficult to interpret because the angle of the boat with respect to shore was not logged, and it was unclear how much the cable arced under the water. The numbers in figure 2.5 (e.g. +4) indicate how many grid cells behind that boat the Acrobat was assumed to be for each position along the transect path.

The boat-mounted surface CTD logged temperature and pressure reliably, but bubbles often obscured the conductivity measurement. The surface salinity was estimated from the Acrobat's T-S relationship during each transect. Water masses are often distinguished by the T-S relationship [Knauss, 1997]. A line on a T-S diagram indicates mixing of two water masses, such as estuarine and oceanic waters. For transects with continuous surface conductivity measurements, the surface and the Acrobat T-S relationships occur along the same line. Hence, surface salinity could be estimated from surface temperature and the Acrobat's T-S relationship.

### **3.4 Velocity Kriging**

The velocities of unsampled grid cells within each transect are estimated with two-dimensional Ordinary Kriging [Rubin, 2003]. Kriging is an interpolation method based on the spatial correlation of the measurements, which is defined in terms of the covariance:

$$C_v(\underline{r}) = \left\langle \frac{1}{N(\underline{r})} \sum_{i=1}^{N(\underline{r})} (v(x_i) - \bar{v}) \cdot (v(x_{i+\underline{r}}) - \bar{v}) \right\rangle \quad (15)$$

$\bar{v}$  is the transect mean velocity.  $N$  is the number of data points a distance  $\underline{r}$  apart from each other. Brackets indicate the average over many transects. The covariance for  $\underline{r}$  is the correlation between each velocity measurement and all velocity data points  $\underline{r}$  apart from the measurement. The covariance often takes the form of an exponential decay function.

$$C_v(\underline{r}) = C_v^0 e^{-\underline{r}/k} \quad (16)$$

The covariance for zero spatial lag,  $C_v^0$ , is the variance ( $\sigma^2$ ). Data points further away from each other should be less correlated, although not necessarily in the raw velocity data. Tidal pumping correlates the side velocities with each other more than the center velocities, even though the sides are closer to the center than to each other. Similarly, bed friction makes the bottom velocities smaller than the top, which inversely correlates the bottom with the top of the water column. Thus, the covariance is calculated on detrended velocity data. Trends have to be simple and physically meaningful while not assuming too much about the form of the data. Separate covariance functions were found for vertical and lateral correlation, because the lateral correlation occurs over distances about an order of magnitude larger than in the vertical direction, and the lateral grid spacing was larger than the vertical correlation length. Linear vertical trends and quadratic horizontal trends were removed from the velocity data before the covariance calculations. Detrending is also important because Ordinary Kriging works under the assumption that the mean of the data set is spatially stationary. It also assumes that



conditions do not change within the 12 minute transects, which is generally true except, as will be shown, when a front moves across the transect path.

Kriging the unknown velocity  $v_o$  at a point  $x_o$  involves the sum of the velocity at every known point  $v_i$  times a weight  $\lambda_i$ , where 1 is the sum of all weights. To find the weights, one minimizes the variance between the value and the expectation of the value based on its correlation with neighboring points:

$$E = \frac{1}{2} \left\langle \left( \sum_{i=1}^N \lambda_i (v_i - v_o) \right)^2 \right\rangle + \mu \left( \sum_{i=1}^N \lambda_i - 1 \right) \quad (17)$$

where  $\mu$  is a Lagrange Multiplier and  $N$  is now the total number of neighbors to the unknown point. Minimizing the above equation by taking partial derivatives with respect to each weight and the Lagrange Multiplier gives  $N+1$  equations for the unknown velocity that are linear functions of the weights, the multiplier, and the covariance exponential relation between the points. Because the lateral and vertical correlation lengths are different, the covariance relation in two dimensions is:

$$C_v(r) = C_v^0 e^{-\sqrt{\frac{y^2}{k_y^2} + \frac{z^2}{k_z^2}}} \quad (18)$$

Kriging was performed top to bottom in lateral cells 11-60 instead of in all 66 lateral grid cells because there was insufficient data close to the shores. This means analyses using the kriged results miss 11% percent of channel cross section. While the flow through the center of the channel is faster than along the sides, the tidally averaged flow is higher along the sides (except very close to shore), so this data gap may cause a greater than an 11% percent error in net advective flux calculations. On the other hand, the north side of

the transect path wraps behind a bluff (Point Cavallo), which should reduce the flow beyond the north side of our transect path. Similarly, the south side of the path loops through deep water between Fort Point and Presidio Shoal. Spring data are kriged only for cells 11-55 because of the shorter transect path during that field campaign.

Within cells 11-60 (11-55 in spring) there are a few points in time without kriged data, because kriging is done only up to one integral scale from data. The integral scale is three times the correlation or e-folding length. With different integral scales in each dimension, an ellipse defined by the argument in the covariance exponential bounds the reach of kriging. Commercial shipping traffic cut short several transects. Horizontally, correlation lengths are 290m  $\pm$  60m during ebb tide and 140m  $\pm$  15m during flood tide. Irregularly shaped sills seaward of the transect path and tidal pumping cause the difference between ebb and flood lengths. During flood tide, the jet-like flow structure in the center of the channel reduces the horizontal correlation scale. Vertically, correlation lengths are longer during flood tide (21m  $\pm$  3m) than ebb (15m  $\pm$  2m), most likely due to greater ebb tide stratification. Kriging is done only for those transects that extend more than 60% across the channel.

A no slip bottom boundary condition was enforced for columns with velocity data by setting the bed velocity to zero. With the no slip condition, Ordinary Kriging yields a reasonable (log-like) velocity profile. As opposed to linear interpolation from the bottom to the lowest sampled depth, which is what would result from Simple Kriging, the other common kriging method, Ordinary Kriging estimates are biased towards the sampled

parts of the water column. In other words, this method does not screen in the same manner that Simple Kriging does. Ordinary Kriging is able to produce log-like profiles, because the ~5m depth of unsampled near-bed velocity is smaller than both the turbulent bottom boundary layer height and the vertical correlation length (15-20m). The log-layer should be a minimum of around ~15m thick for Ordinary Kriging to work in this case. The log-layer meets this thickness criterion after the first half hour beyond mean slack based on a bottom boundary level thickness calculated from turbulent flow over a flat plate [Crowe *et al.*, 2001]:

$$\text{thickness}(t) = \frac{0.16 \cdot x(t)}{\text{Re}_x^{1/2}(t)} \quad (19)$$

where  $x$  is the tidal excursion  $\left( x(t) = \int_{\text{slack}}^t v dt \right)$  and Reynolds number  $\left( \text{Re}_x = \frac{vx}{\nu_t} \right)$  uses the eddy viscosity from Fischer [1979, p.106]. Stratification could reduce boundary layer growth, however, stratification is weakest and vertical mixing is strongest in the bottom third of the water column. Visually, flow features during the first half hour appear to be at least 15m thick.

### 3.5 Splining, an Alternative to Kriging

The velocity fields could have been filled by splining instead of by kriging. The scalar fields are filled with a combination of both methods. In this section, we will discuss how splined results might differ from kriged results. For this project, we use the TSpline Matlab toolbox (<http://www.soest.hawaii.edu/pwessel>), which is an implementation of the 2D tensioned spline equations developed by Wessel [1998]. Unlike kriging, splining has the advantage of using slopes as well as data points as constraints. This advantage can

be useful in certain circumstances. Splining can be used, for example, in extrapolating salinity results to the bed because one could enforce a no flux (i.e. zero slope) bottom boundary condition. A disadvantage of splines is that they can produce extreme, non-physical values in order to fit data trends (figure 3.2). When interpolating, this can be prevented by adding tension to the spline. Spline tightness can be adjusted to produce nearly identical interpolated values as from Ordinary Kriging, and splining is much more computationally efficient. However, tight splines have a disadvantage. When they extrapolate, they use the data trend from the nearest neighbors (figure 3.2), which can be highly influenced by measurement noise. Ordinary Kriging, in contrast, assumes a stationary mean, so it will not make estimates outside of the values spanned by the actual measurements. Furthermore, Ordinary Kriging also yields an estimate of the uncertainty of each of its point estimates, which splining does not.

### **3.6 Scalar Kriging**

Measured scalar data are sparser than velocity, which complicates interpolation and extrapolation. Three to four sine wave shaped scalar profiles were collected per transect. Continuous temperature and intermittent salinity measurements were made at the surface. Surface salinity data gaps in each transect are inferred from the temperature-salinity relationship present in the Acrobat data for each transect. Kriging to the bed with just the scalar data would make salinity and temperature asymptote towards the cross-section mean at the bed instead of towards higher density values, introducing spurious unstable stratification. Two solutions were explored. First, as was done in the velocity data, vertical trends were removed from the data. Both linear and exponential trends were

tested, but both generated spurious data due to differing cross-channel trends between surface and mid-column data. A more reliable solution involving estimation of near-bed salinity and temperature is used, instead of relying on trend removal. A tight spline interpolates data gaps within the area bounded by the raw data. Then an exponential  $(A - Be^{-Cz})$  is fit to profiles of each column in the convex hull. The form and curvature of these profiles, and thus the near-bed extracted values, agree with the vertical profiles taken in our experiment and by the Naval Postgraduate School the day after our fall experiment (Collins, pers. comm. 2003). The profiles are mostly continuously stratified salinity fields with smoother overall structure than the velocity field. After making near bed estimates, salinity and temperature are kriged to the same area as velocity. The resulting scalar fields are found to approximate the no-flux bottom boundary condition.

### 3.7 Overview of Conditions

All of the analysis from here through chapter 6 relies on the kriged cross-sections to supply salinity, temperature, and velocity snapshots in time. Here we present typical kriged cross-sections and provide a qualitative discussion of the tidal cycle development. Figure 3.3 has snapshots of spring season velocity.

As the flow transitions from slack to flood, water first flows landward near the bed on the south side of the channel (figure 3.3c<sub>1</sub>). This jet expands upwards as it migrates towards the center where it strengthens to  $150 \text{ cm s}^{-1}$  as it joins a smaller jet from the north side. As flood tide continues, the central jet narrows to a width of 1500m, and it separates around a peak in the main sill (figure 3.3a<sub>1</sub>). The jet width is related to the width of the

narrowest portion of Golden Gate Channel, which contracts to 1300m 1km seaward of our transect path. At the beginning of ebb tide, the tide turns seaward first in the upper part of the north side of the channel (figure 3.3d<sub>1</sub>). As the ebb tide structure develops, water continues flowing seaward throughout the channel, with slowest velocities on the north side in front of a sill (figure 3.3b<sub>1</sub>).

The tidal pattern of cross-channel velocity is more complex than the along-channel. We define the along-channel direction (27 degrees north of east) by the mean of the ebb and flood current directions averaged over all transects. At the beginning of flood, cross-channel velocity first switches to the north near the bed on the north side of the channel transect (figure 3.3c<sub>2</sub>). At maximum flood the jet spreads slightly, with the portion south of the sill spreading southward and the northern portion spreading northwards, particularly on the bed behind the sill (figure 3.3a<sub>2</sub>). At the beginning of ebb, water first turns southward at the surface above the main sill (figure 3.3d<sub>2</sub>). In contrast, at maximum ebb southward velocity is highest near the bed on the north side as the flow steers around the sill.

Considering along and cross-channel velocities together, the speed of water at maximum ebb is roughly constant across the cross-section, and the flow is directed inwards towards the center of the channel. Ebb currents take the form of a potential drain (figure 3.3c). This flood jet/ebb drain tidal asymmetry is tidal pumping [*Stommel and Farmer, 1952*]. The ebb tide changes in cross-channel velocity around the sill will be described as effects of a headland eddy that forms on flood tide behind Point Cavallo.

Flow structures during the spring experiment are qualitatively different from those in the fall experiment (figure 3.3ab vs. figure 3.4ab). Spring velocity profiles are, in general, more sheared than fall profiles. This is to be expected due to increased vertical density stratification during spring in response to freshwater flow. Freshwater flow during our spring-runoff data collection period is  $630 \text{ m}^3 \text{ s}^{-1}$ , which is about the typical annual mean flow of  $600\text{-}700 \text{ m}^3 \text{ s}^{-1}$ , and well under the typical annual maximum of  $2500\text{-}3000 \text{ m}^3 \text{ s}^{-1}$ . But freshwater flow during spring-runoff is still more than five times larger than the outflow during our fall experiment ( $120 \text{ m}^3 \text{ s}^{-1}$ ). The 2002 peak spring runoff, which occurred unusually early, was missed. Peak runoff came after a large storm during a warm early January, and preceding a dry late-winter and spring. Nonetheless, there are obvious differences between fall and spring flow structures. Fall experiment data should be representative of the season, because fall outflow is relatively constant both within and between years. Velocity structures from the summer experiment (not shown) are similar to those from the spring experiment.

A summary of conditions during each of the three seasons is provided in table 3.1. The salinity ranges during spring and summer experiments are much higher than the range during the fall experiment, and temperature gradients make large contributions to density gradients only during the fall experiment.

	Spring '02 Runoff	Summer '03 Upwelling	Fall '02 Relaxation
Mean Salinity	30.2	30	32.1
Mean Temperature (oC)	11.9	12.8	14.2
Range of Transect Mean Salinity	28.0-31.8	28.3-32.0	31.5-32.6
Mean Salinity Difference in a Transect	3.1	3.6	0.77

Salinity Change per kilometer	0.23	0.21	0.06
Gauged River Flow ( $\text{m}^3 \text{s}^{-1}$ )	632	460	123
Density Change Due to Temperature	7%	16%	27%

Table 3.1: Summary of Conditions

A water mass analysis based on salinity and temperature suggests there are three water types present at the study site: North Bay, South Bay, and oceanic (figure 3.5). Near low slack, the temperature-salinity relationship diverges based on lateral position in the channel, with the north side of the transect path being less saline at the same temperature. Near high slack, however, the cross-section is characterized by a single T-S relationship. Water with properties in between these end members indicates that mixing has occurred. While along-channel mixing is expected at an ocean-estuary interface, it is notable that there are data in between the North and South Bay end members. Later, in discussion of the lateral density gradient (figure 5.4), we will describe a mechanism for lateral mixing mechanism between these end members. This divergence of the T-S relationship near low slack is accentuated during fortnightly spring tides (compared to neap tides) due to the associated increase in tidal excursion.

Following this overview of the data, we move forward with detailed discussions of tidal variability, residual flow, and exchange to explain and quantify the general features.



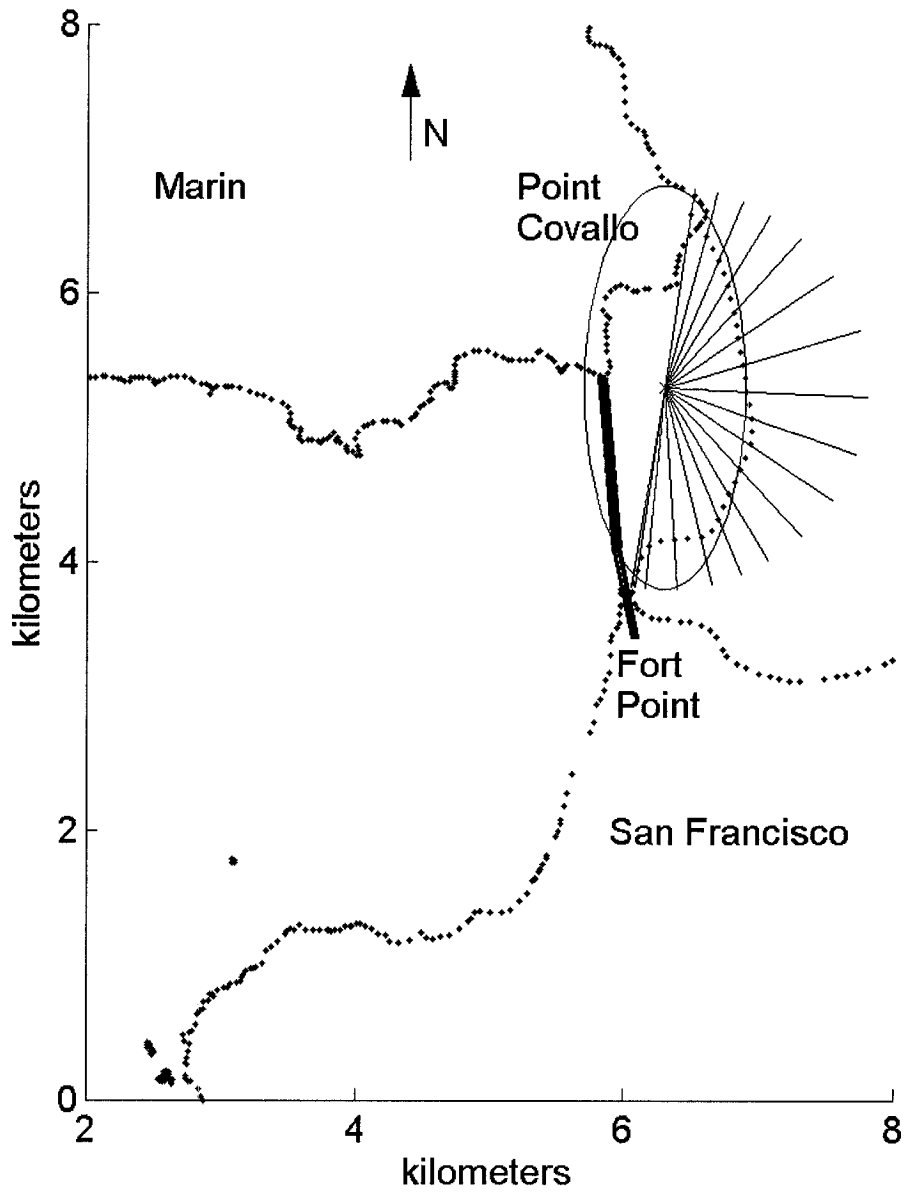


Figure 3.1: Grid Path

Data are projected onto a grid along the mean boat path using cylindrical coordinates with depth as the axial coordinate.

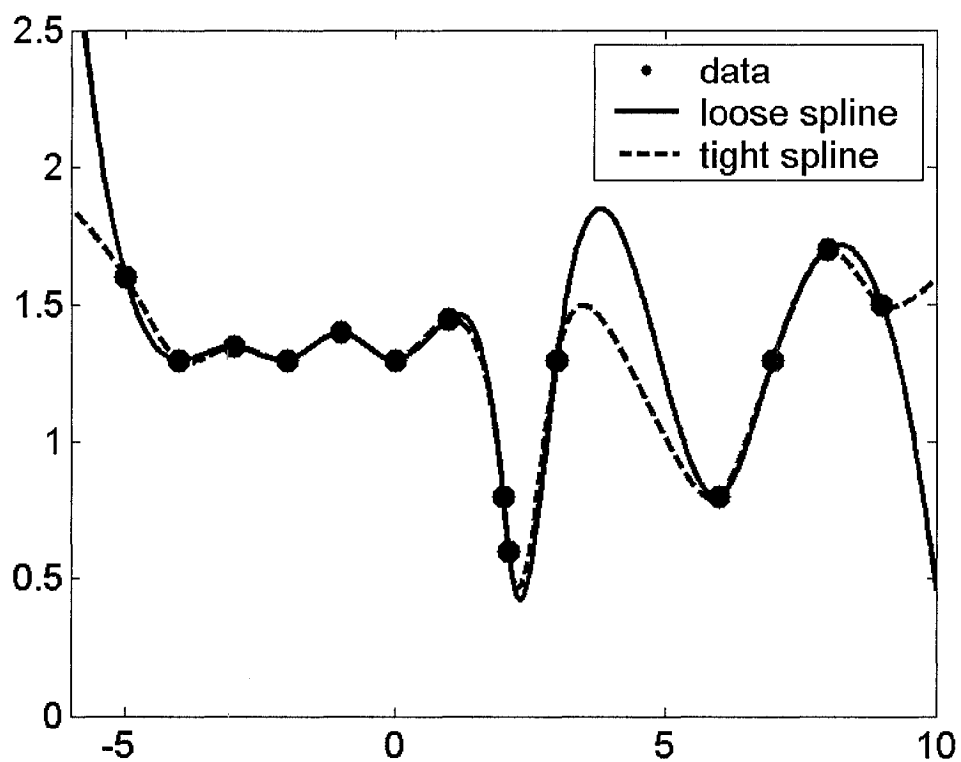
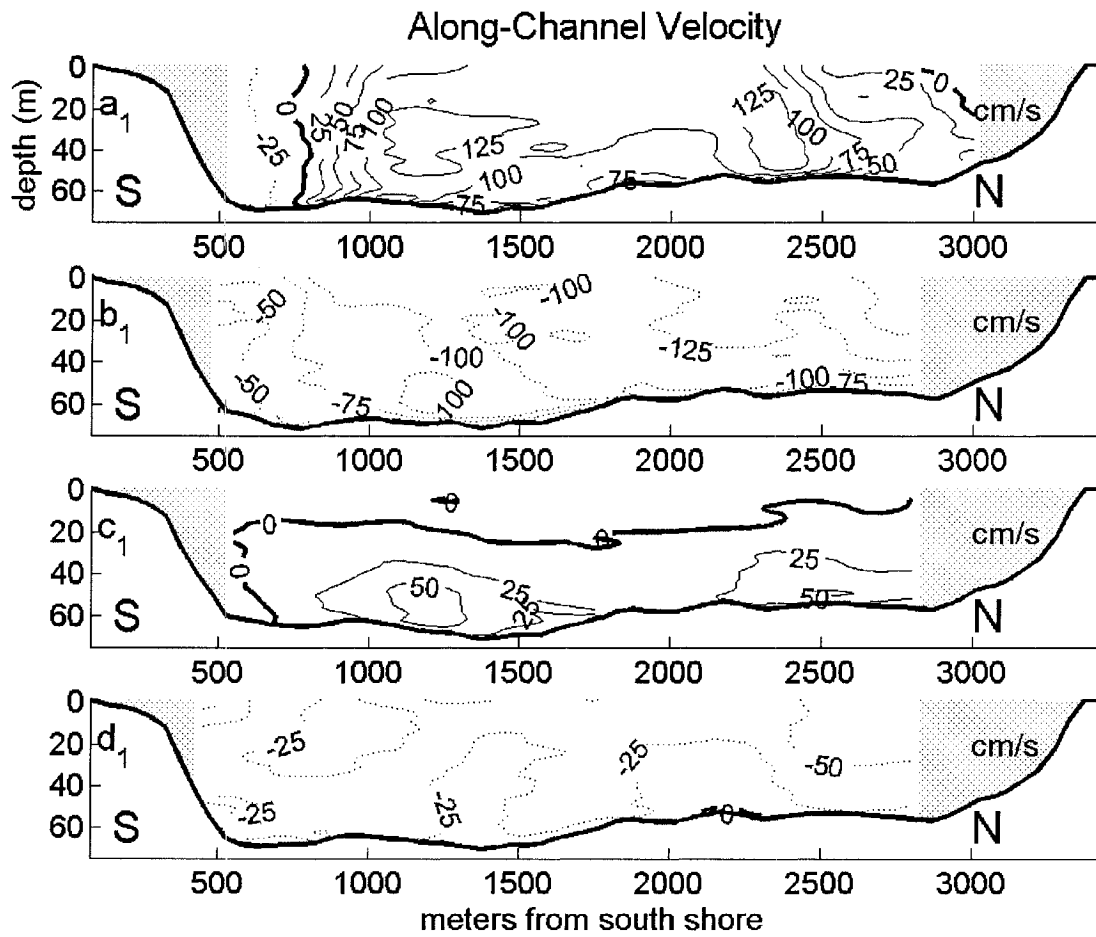


Figure 3.2: Spline Features

Tight splines can accurately interpolate between data points. However, when extrapolation is done with a tight spline, the data trend from the nearest neighbors is used, and the local trend is not always representative of the main trend of the data. These features are illustrated with an artificially created data set.



(The caption for figures 3.3a<sub>1</sub>-3.3d<sub>1</sub> is on the next page)

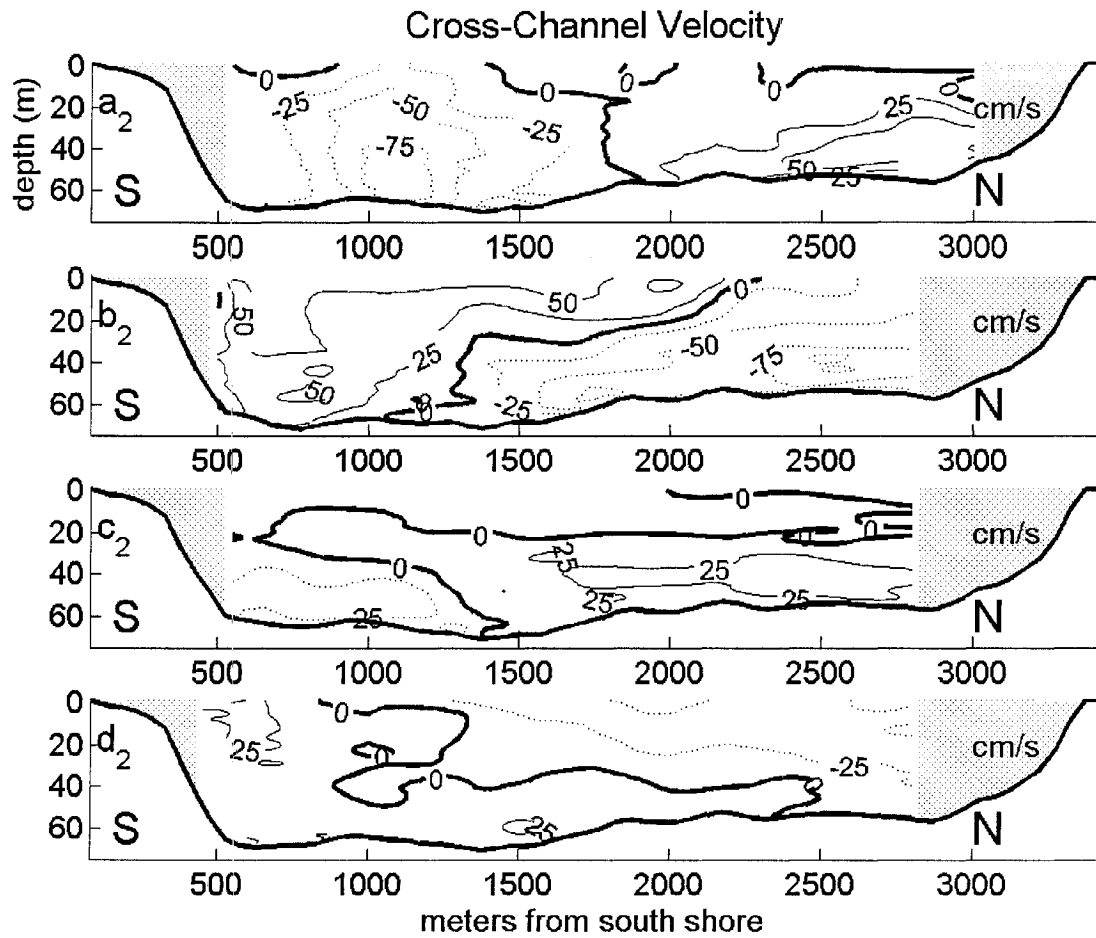


Figure 3.3: Typical Spring-Runoff Velocities

Maximum flood (a), maximum ebb (b), early flood (c), and early ebb (d) velocity cross-sections from the spring-runoff experiment kriged to a grid spanning typical transect paths. Along-channel positive is into the bay (subplots a<sub>1</sub>-d<sub>1</sub>). Cross-channel positive is the northward normal to the along-channel positive (subplots a<sub>2</sub>-d<sub>2</sub>).

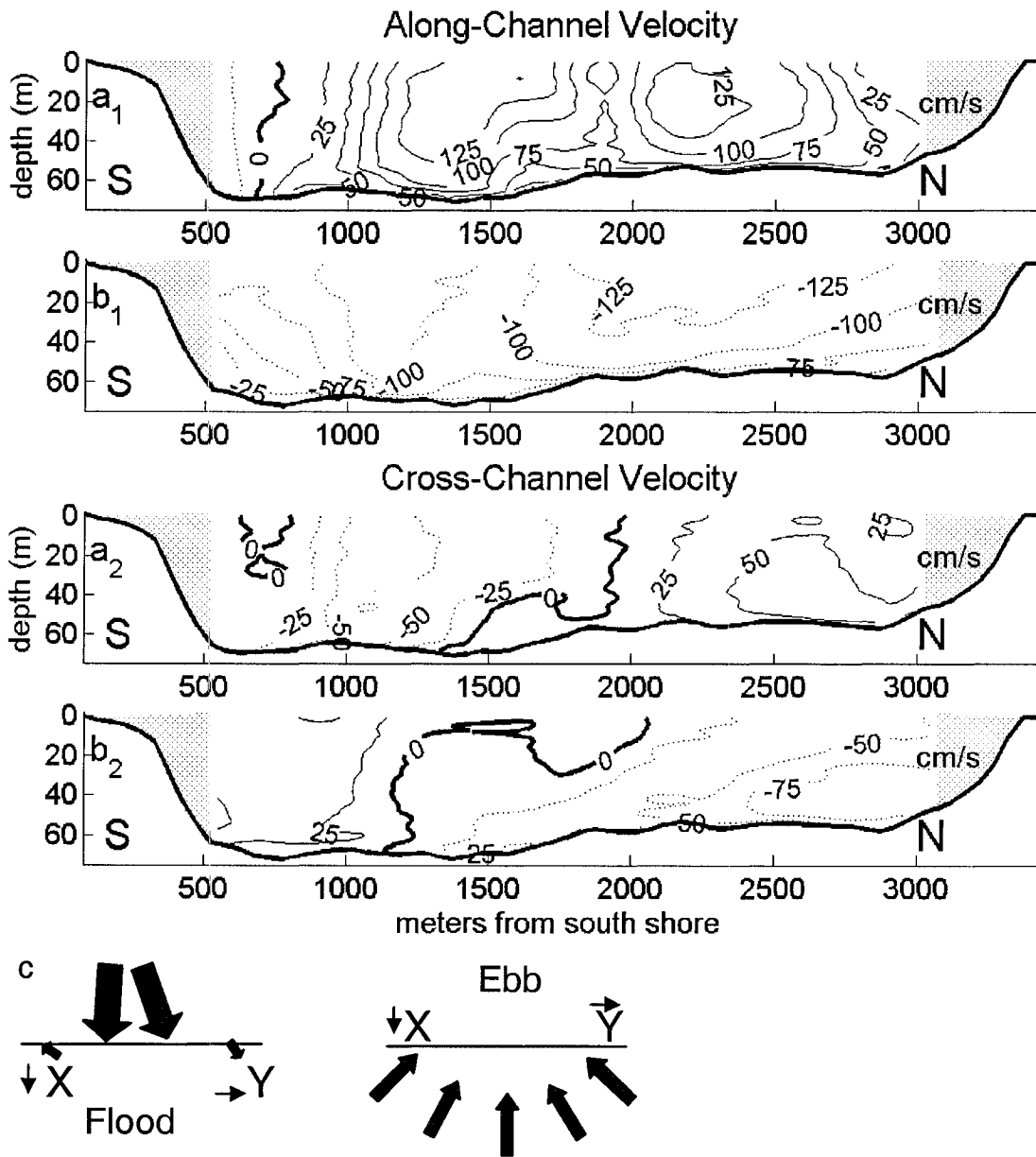


Figure 3.4: Typical Fall-Relaxation Velocities

Maximum flood ( $a_1$  and  $a_2$ ) and maximum ebb ( $b_1$  and  $b_2$ ) cross-sections from the fall-relaxation experiment kriged to a grid spanning typical transect paths. There is less vertical shear than in wetter seasons (figure 3.3). Schematics (c) show typical depth-averaged flow at maximum flood and maximum ebb.

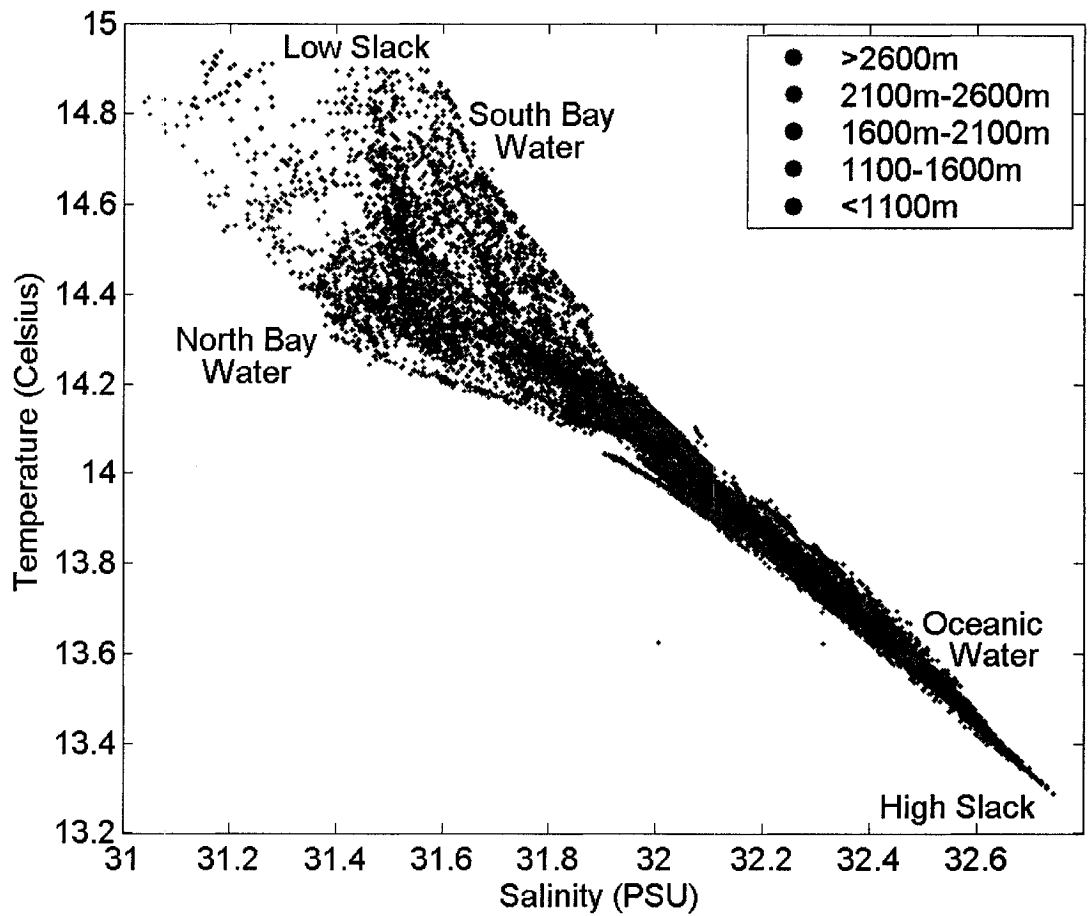


Figure 3.5: T-S Relationship

Grouped by distance along the mean transect path from the south shore, three water masses are distinguishable: the coastal ocean, North Bay, and South Bay. Data are from 11/06/02.

## 4 Tidal Variability

### 4.1 Introduction

If a particle released at the Golden Gate was tracked over a tidal cycle, it would travel as far as 30km, but it would end up close to where it started. In this chapter, we examine the degree to which Golden Gate waters merely slosh back and forth with the tides versus the degree to which tidal asymmetries develop. We start with Principal Component Analysis to isolate and describe the main modes of variability at the transect path, and then we extend our view across western Central Bay with numerical modeling. Tidal pumping is the primary tidal asymmetry at this field site. Therefore, we conclude with an evaluation of the data set against this analytical theory.

### 4.2 Principal Component Analysis

#### 4.2.1 Theory

Principal Component Analysis (PCA) is a statistical method used to isolate correlations that persist in a data set through time [Preisendorfer, 1991]. In this case, the data sets are the kriged velocity, salinity, and temperature cross sections. PCA is used to examine how data from different parts of the transect grid are correlated to each other in time. As a statistical method, PCA results are not biased by *a priori* assumptions about the data. This is different than the physically-based approach that will be used in chapter 5, in which several forcing mechanisms will be compared. The physically-based approach cannot guarantee that the main forcing mechanisms are being considered. In contrast, PCA reveals a rank ordered list of the modes of variability, with the number of modes

equal to the number of grid cells in a transect. Among the top several principal components will be the main spatial structures that vary in time within the data. This ranked list is used as a guide for isolating the main features that will need to be explained with physically-based analysis in future sections.

Next we describe the implementation of PCA on cross-channel velocity,  $v$ , the same analysis performed on the other measured quantities. To reduce noise and to simplify visualizations, the data are first aggregated into 17m deep by 250m wide blocks. These length scales are less than or equal to the data correlation lengths, so data are well correlated within each aggregated block. This reduces the number of spatial degrees of freedom from about 3000 to 45.

To find the correlation between time series of the 45 blocks, we take a more general covariance than the one used for kriging (equation 15), which grouped the covariances by spatial lag. Here, the locations are considered independent.

$$C_{ik} = \frac{1}{N} \sum_{j=1}^N (v_{ij} - \bar{v}_i) \cdot (v_{kj} - \bar{v}_k) \quad (20)$$

'i' and 'k' index the 45 blocks in space. 'j' indexes the N number of transects. The overbar indicates an average over all transects at each location. These temporal means are examined in detail in section 4.2.2. The principal components, also called empirical orthogonal functions (EOFs), are the eigenvectors ( $E_{ik}$ ) of the covariance matrix. Each column, i, is an EOF, so there are 45 EOFs in  $E_{ik}$ . Section 4.2.3 describes the significant EOFs. A significant EOF, or main mode of variability, is an EOF that represents a large portion of the variance of the velocity signal. The square root of each eigenvalue over the



sum of the square roots of all of the covariance matrix's eigenvalues is the fraction of the variance represented by its corresponding eigenvector. One can produce a time series of each EOF from the data and the eigenvectors:

$$A_{ij} = \sum_{k=1}^M E_{ik} v_{kj} \quad (21)$$

$i$  indexes the  $M$  EOFs and  $j$  indexes the transects in time. A time series of a single EOF then shows the temporal variability of spatial structure that spans the entire cross section. Time series for the EOFs are examined in section 4.2.3. In other contexts [e.g. *Stacey et al.*, 2001], complex PCA is performed on velocity vectors, instead of separately on velocity from each direction. This results in half the number of EOFs, but the EOFs contain both along-channel and cross-channel information, making it hard to identify the direction of flow represented by each EOF. Here, velocity is separated in the two directions to produce EOFs with the same coordinates as analyses in proceeding sections.

#### 4.2.2 Empirical Orthogonal Functions

The first two or three EOFs for each measured quantity are shown (figures 4.1-4.3). The EOFs presented have visibly coherent spatial structures, statistically significant M2 tidal variability (section 4.2.3), and they represent a portion of the variability above the Kaiser Criterion [*Preisendorfer*, 1991], which in this case is 2.5% or one over the number of 17m by 250m blocks. From figure 3.3, one can assume that at the Golden Gate the main barotropic signal is stronger in the along-channel than in the cross-channel direction. Thus, secondary features of similar magnitude would represent less of the along-channel variance than the cross-channel variance. As a result, cross-channel EOFs must represent a larger minimum percentage of the variance to be considered significant.

Figure 4.1 shows the first two along-channel velocity EOFs. The first EOF, which describes 92.4% of the along-channel temporal variability, represents barotropic flow (figure 4.1a). During flood tide, it will be shown that this EOF is positive, and thus along-channel velocity is positive (into the bay) over the entire cross-section with strongest velocity in the center. During ebb tide, it will be shown that this EOF is negative, and thus along-channel velocity is negative over the entire cross-section. The second EOF accounts for lateral velocity variability and thus represents the flood jet-ebb drain asymmetry (3.0%), with inflow in the center and outflow on the sides (figure 4.1b). The remaining 39 EOFs account for the remaining 4.6% of the along-channel velocity variance; these functions had little or no coherent spatial structure and are not included in this discussion. The primary cross-channel EOF includes mainly jet-drain flow. It also includes some vertical shear 1500-2500m from the south shore, a location that is adjacent the sill on the north side of the channel (63.4%, figure 4.2a). Cross-channel vertical shear variability is also greater on the north side of the channel in the second EOF (13.6%, figure 4.2b).

The spatial structures underlying the variability of the density field are presented in figure 4.3. The first salinity EOF represents barotropic advection of the longitudinal density gradient. During flood tide this EOF increases or becomes less negative, corresponding with increasing salinity over the entire cross-section, and vice versa during ebb tide. This structure, which describes 89.6% of the density temporal variability, is stronger on the north side of the channel and higher in the water column (figure 4.3a). The second EOF

(5.6%) mainly represents the variability of vertical stratification, but it also includes some center-side asymmetry and lateral variability (figure 4.3b). The third EOF (1.9%) shows lateral variability, with higher density on the south side than the north side and unstable vertical stratification (figure 4.3c). The remaining 38 EOFs account for the remaining 2.6% of the density variance and are neglected in the remaining analysis. The first few salinity EOFs explain a larger percentage of the variance than for velocity due in part to the loss of small-scale variability in the salinity field through the measurement and interpolation schemes. However, it is expected that the salinity field would have less vertical structure than velocity, as there is a no-flux bottom boundary condition for salinity, while the bed provides a momentum sink and establishes near-bed velocity variability.

### **4.2.3 EOF Tidal Variability**

The amplitudes of each EOF multiplied by the spatial structures described in the previous section reproduces the observations, with each of the six study days having an associated EOF amplitude time series. Seasonal differences will be discussed later; here we look at trends across all days. Each of the three data types shows strong M2 tidal variability during all days, so the data are lined by M2 tidal phase. Specifically, the EOFs are lined up by the semi-diurnal zero crossings of the along-channel velocity, and then block averaged with a Butterworth Filter. The filter averages among the eight nearest data points, with more weight on the nearest neighbors. Each filter window is thus likely to include at least one data point from each season. Eight data points span on average 9.6 minutes, but the filter also averages over neighboring windows, giving it a span of closer

to 15 minutes. Error bounds for each EOF amplitude time series show the standard deviation of the mean for the high-frequency residuals within each window.

The first density and along-channel velocity EOFs follow the M2 tidal cycle (figure 4.4a and 4.4c). Thus, the first along-channel velocity EOF represents the barotropic tide. In turn, the first density EOF rises and falls with the M2 tide, so it represents barotropic advection of the mean longitudinal density gradient. Based on the spatial structure of the first density EOF (figure 4.3a), we see a wider tidal range of density on the north side of the channel, most likely because the bay's main freshwater source enters from the North Bay (figure 3.5).

The second EOF for along-channel velocity, which represents lateral velocity differences (as evident in figure 4.1b), is primarily positive, except for a large negative trough as the tide transitions from ebb to flood tide (around hours 0-1 in figure 4.4a). Positive values of this EOF focus the flood jet in the channel center and spread the ebb drain across the channel. Peaking at max ebb and max flood, this EOF varies at double the M2 tidal frequency, so it has M4 tidal variability. The large negative pulse during the ebb-flood transition is a result of frictional phasing between the shallow perimeter regions, where flow reverses first, and the deep channel regions that remain ebbing for a longer period [Valle-Levinson and O'Donnell, 1996]. Then, at the flood-ebb transition, the lateral structure that results from the phasing counteracts the more persistent flood-ebb asymmetry (around hour 7 in figure 4.4a). Further, as a result of frictional phasing, the shoal-channel phasing signal (EOF #2) lags about 30 minutes behind the barotropic

signal (EOF #1), representing the time scale for frictional effects to be communicated over the depth of the channel.

The first two along-channel EOFs also modulate vertical shear, as do the third and fourth EOFs, which are not shown. Instead of discussing a complicated pattern of four EOFs, however, we will examine vertical shear variability across the channel directly in the next section. Similarly, the first three density EOFs each have some vertical and lateral variability, so we will discuss the density gradients later. However, we do note that density EOF #3, which has the most coherent lateral structure, varies strongly at high slack (hours 6-8 in figure 4.4c) in concert with density EOF #2, which has the largest vertical gradients. At low slack (hours -1 to 1 in figure 4.4c), EOF #2 varies more sharply than the others.

The first cross-channel velocity EOF amplitude tracks converging flow on ebb tide and diverging flow on flood tide (figures 4.4b and 4.2a). It is stronger on ebb than flood tide because of the jet-drain asymmetry. The second cross-channel EOF, representing vertical shear, has pronounced peaks at the beginning of ebb (hours 6-8 in figure 4.4b) and flood (hour 0) tides—the same times as the variability in density EOFs #2 and #3. The tidal and density-driven forcing of these two cross-channel vertical shear peaks and their impact on along-channel vertical shear will be developed in section 5.3.

### **4.3 Modeling Tidal Variability**

Large eddy and frontal structures are frequently present in this region of San Francisco Bay due to the interaction of energetic tidal flows with the complex bathymetry in the region. Digital images of the bay's surface (not shown) indicate extensive surface features during the flood tide and in the flood-ebb transition. During the transition from flood tide to ebb tide, any transient features created during the flood tide may affect the structure of the reversal of the tide into the ebb. To evaluate the formation of these features and to visualize how such a feature influences the flood-ebb transition, we use the TRIM [Tidal, Residual, Intertidal Mudflat, *Casulli*, 1990] model. TRIM2D, which models depth averaged properties, and has been calibrated to San Francisco Bay currents and surface elevations [*Cheng et al.*, 1993].

The model is forced with a sinusoidal 0.57 meter M2 tidal amplitude signal that produces the mean tidal range (1.24 m) at the Golden Gate tide gauge. The coastline in figure 1.5 defines the model boundary. The upstream boundary is closed at the west end of the delta for simplicity, which is reasonable because it is far enough away to have little qualitative effect on depth averaged barotropic tidal features near the Golden Gate. The ocean boundary is cut perpendicular to the mean flow direction several kilometers outside the Golden Gate Channel. The angle of the ocean boundary to the channel and its distance from the channel affect the size of modeled barotropic features at our transect path. While the model has been calibrated to an extensive amount of data from the bay and the boundary orientation is logical, more data should be collected seaward of the Golden Gate Bridge to adequately simulate this boundary. Thus, we will use the model merely to illustrate the barotropic features that cross our transect path. The following

results were generated with a 20 second time step on a 100m rectangular grid after allowing the model to spin up for 3 days.

For the first part of flood tide, flow across the entire channel goes east and northeast into the bay (figure 4.5a). As the tide strengthens, an eddy forms along the shoal between Point Sausalito and Point Cavallo. The eddy separates from the shoal just after high tide, and return flow behind it hugs the shore as it travels seaward (figure 4.5b). As the flood jet recedes at the end of flood, eddy return flow pushes across the transect path alongside the main sill and continues to affect the north side of the transect path for the first 1.5-2 hours of ebb tides (figure 4.5c). Afterwards, flow goes westward across the transect path (figure 4.5d).

Although this modeled feature is, by definition, uniform over the depth, as the flood tide eddy moves out from behind Point Cavallo, it is likely to produce a sheared water column as it interacts with the region's complex bathymetry. Thus, while the formation of the eddy is captured with the depth-averaged model, we turn to the measurements to evaluate the influence of the eddy at our transect site. The eddy return flow, which coincides with the cross-channel vertical shear event in the PCA, causes southward flow across the transect path at the surface, increasing north side cross-channel vertical shear (figure 4.6b hours 6-8). After the eddy passes, flow is seaward at the surface, but runs southward on the bottom to get around the sill, decreasing north side cross-channel vertical shear (figure 4.6b hours 8-9 and figure 3.3b<sub>2</sub>). Correspondingly, north side along-channel vertical shear peaks markedly after the eddy passes (figure 4.6a hours 8-9 and -4 to -1).

Using the model calculations and averaging over several tidal cycles shows the eddy's effect on depth-averaged mean velocity (figure 4.7). Flow behind the eddy transports relatively fresh water from Raccoon Strait through the Golden Gate. Eddy return flow combines with a smaller clockwise net circulation between Presidio Shoal and the south end of the Golden Gate Bridge to produce a net cross-channel flow. From the model results averaged over the transect path this cross channel flow is  $-4.9 \text{ cm s}^{-1}$ , which is close to the observed value averaged over all transects ( $-6.5 \text{ cm s}^{-1}$ ).

#### 4.4 Axial Circulation

On the tidal timescale, axial circulation (in the y-z plane) can develop in addition to circulation from headland eddies (in the x-y plane). Axial circulation increases stratification, which in turn suppresses vertical mixing and which can influence vertical shear [*Nunes and Simpson, 1985*]. One would expect stratification to drop during flood tide due to tidal straining of the along-channel density gradient. While lower than ebb tide, flood tide stratification remains relatively constant (figure 5.4, hours 1-5). We suggest that axial circulation replenishes stratification while tidal straining erodes it.

On flood tide in an estuary, if flow is faster in the center than the sides, then the center will become saltier than the sides. At the Golden Gate, this differential advection is caused by the flood jet. We can evaluate the effects of these center-side asymmetries by analogy to flows in estuaries with shoal-channel depth differences [*Lerczak and Geyer, 2004; Nunes and Simpson, 1985; Valle-Levinson and Lwiza, 1995*]. The lateral density



gradient drives flow towards the center at the surface and flow towards the sides at the bed, resulting in convergence and downwelling in the channel center. The cross-channel velocities of the two resulting axial circulation cells stratify the water column (figure 4.8). The circulation is defined by the curl of the velocity (vorticity) within the cell or equivalently by the velocity around the rim of the cell:

$$\Gamma = \int_A \underline{n} \cdot (\nabla \times \underline{U}) dA = \oint_C \underline{U} \cdot d\underline{s} \quad (22)$$

A is the area of the circulation cell bounded by C,  $\underline{s}$  is the distance vector counter-clockwise tangent to C in the plane defined by A, and  $\underline{n}$  is the unit normal to C in the plane defined by A (figure 4.9). The velocity around the rim of the two cells requires vertical velocity measurements, which in this experiment are measured to less percent accuracy than cross-channel velocities because they are over an order of magnitude smaller while having similar magnitude uncertainties. To see the tidal trend of circulation, we thus have to filter over more transects than for the previously described tidally aligned data. Stratification increases as a result of circulation by the product of the lateral density gradient and the vertical shear from the circulation  $\left( \frac{\Delta \rho}{\Delta z} = \frac{\Delta \rho}{\Delta x} \frac{\Delta u}{\Delta z} \Delta t \right)$ .

In section 5.3.2 it will be shown that differential advection is stronger during the second half than during the first half of flood tide. As a result, a lateral salinity difference of 0.5 PSU develops between the center and the sides during the second half of flood tide (figure 4.8). Circulation strengthens around the two axial cells in the expected orientations; however, this calculation involves differences between uncertain quantities, so the value of the circulation's cross-channel velocity scale of  $2 \text{ cm s}^{-1}$  is just an

estimate. The velocity scale is the circulation over the circumference of a cell (C).

Integrating the cross-channel vertical shear from circulation times the center-side density gradient provides an extra  $0.2 \text{ kg m}^{-3}$  of top to bottom stratification during the second half of flood tide.

#### **4.5 Tidal Variability Summary**

There are several prominent tidal asymmetries at this field site. From Principal Component Analysis, it is shown that tidal pumping creates a strong lateral flow asymmetry. Related to the flood jet part of tidal pumping, two axial circulation cells develop during the second half of flood tide. A tidally trapped eddy during high slack transition makes an asymmetry on the north side of the transect path, which is evident in the cross-channel velocity EOF times series. At low slack there is a smaller peak in the cross-channel velocity EOF time series. Next we explore how tidal asymmetries and other factors contribute to residual flow.

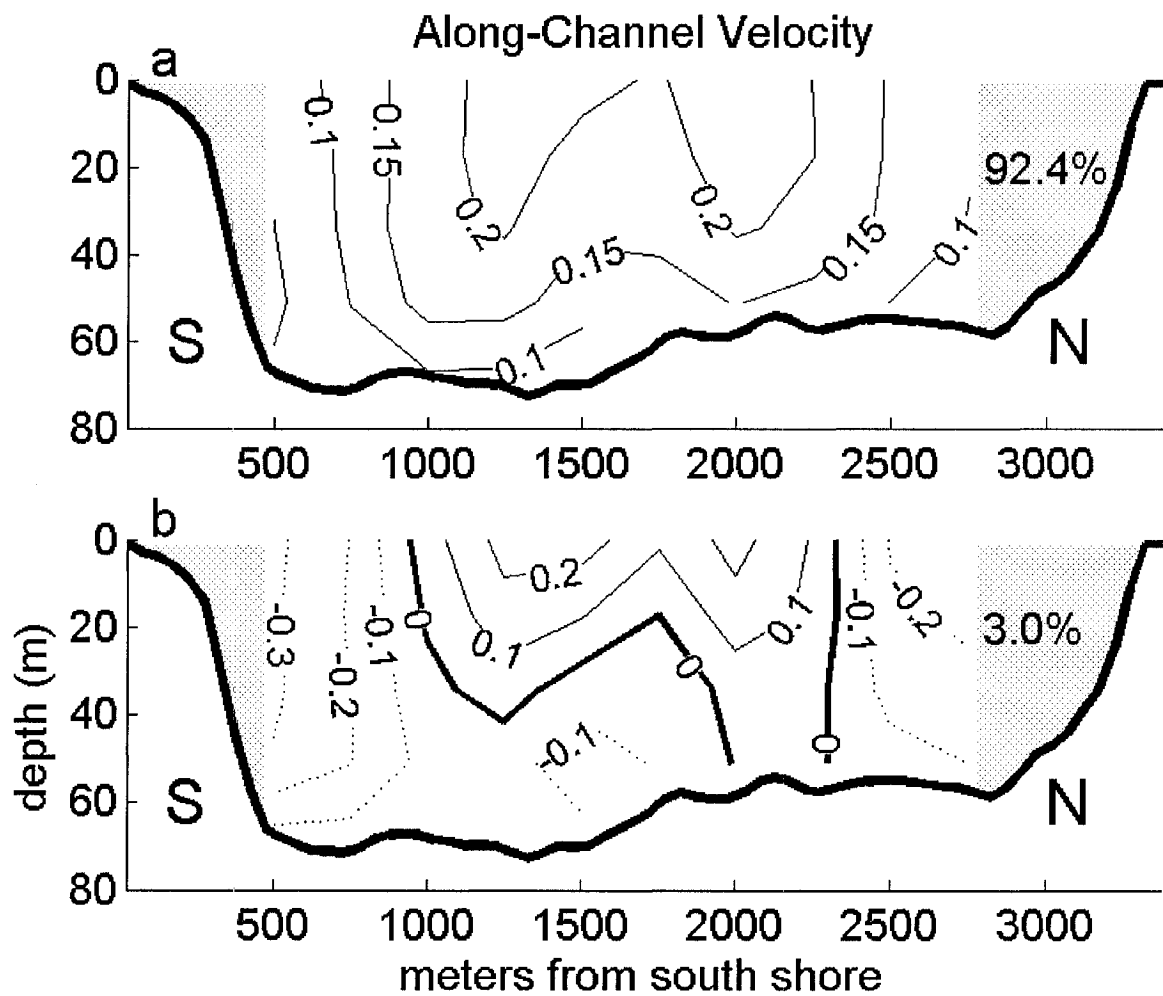


Figure 4.1: Along-Channel EOFs

The first two along-channel EOFs of velocity are listed in order of the variance percentage explained by each EOF. Along-channel positive is into the estuary.

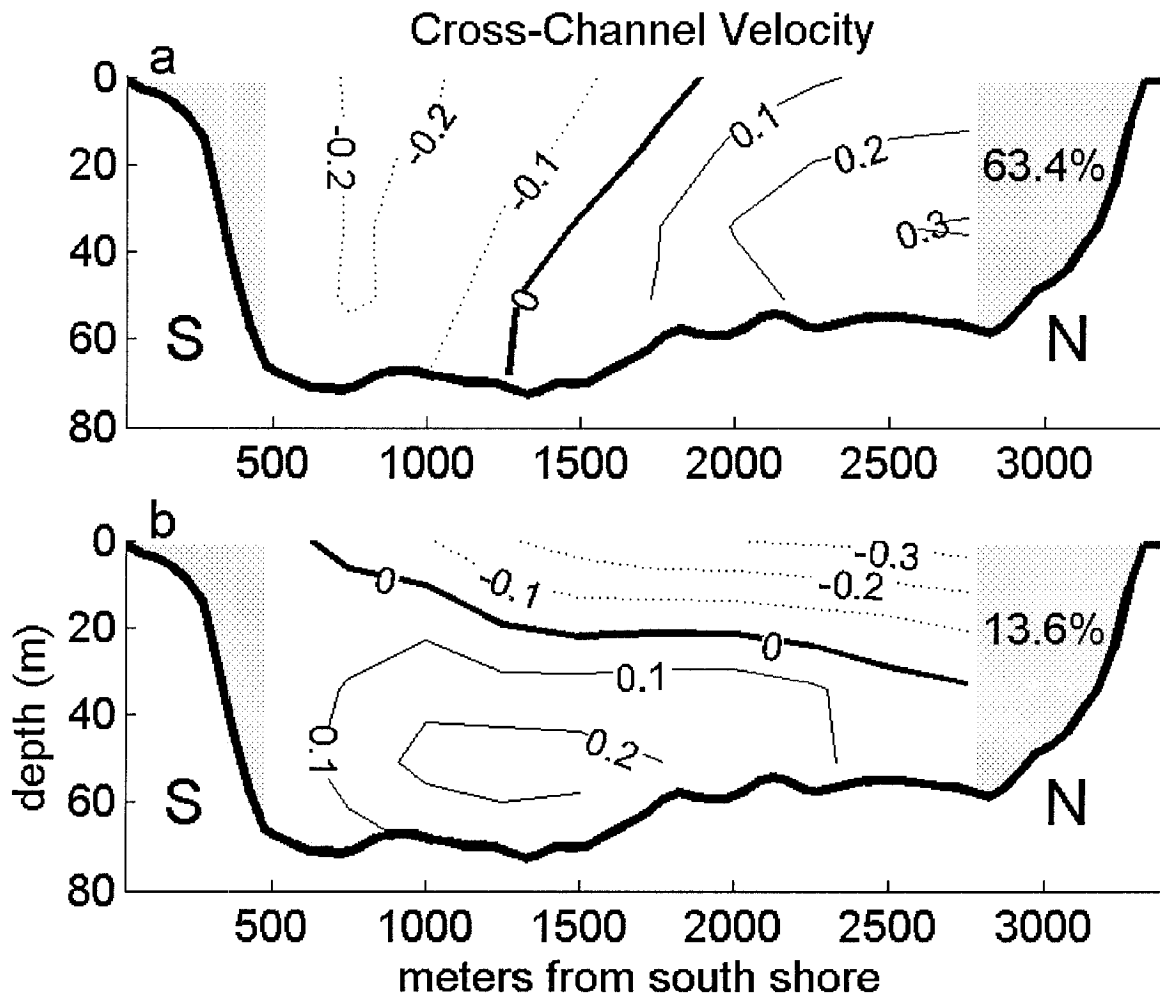


Figure 4.2: Cross-Channel EOFs

The first two cross-channel EOFs of velocity are listed in order of the variance percentage explained by each EOF.

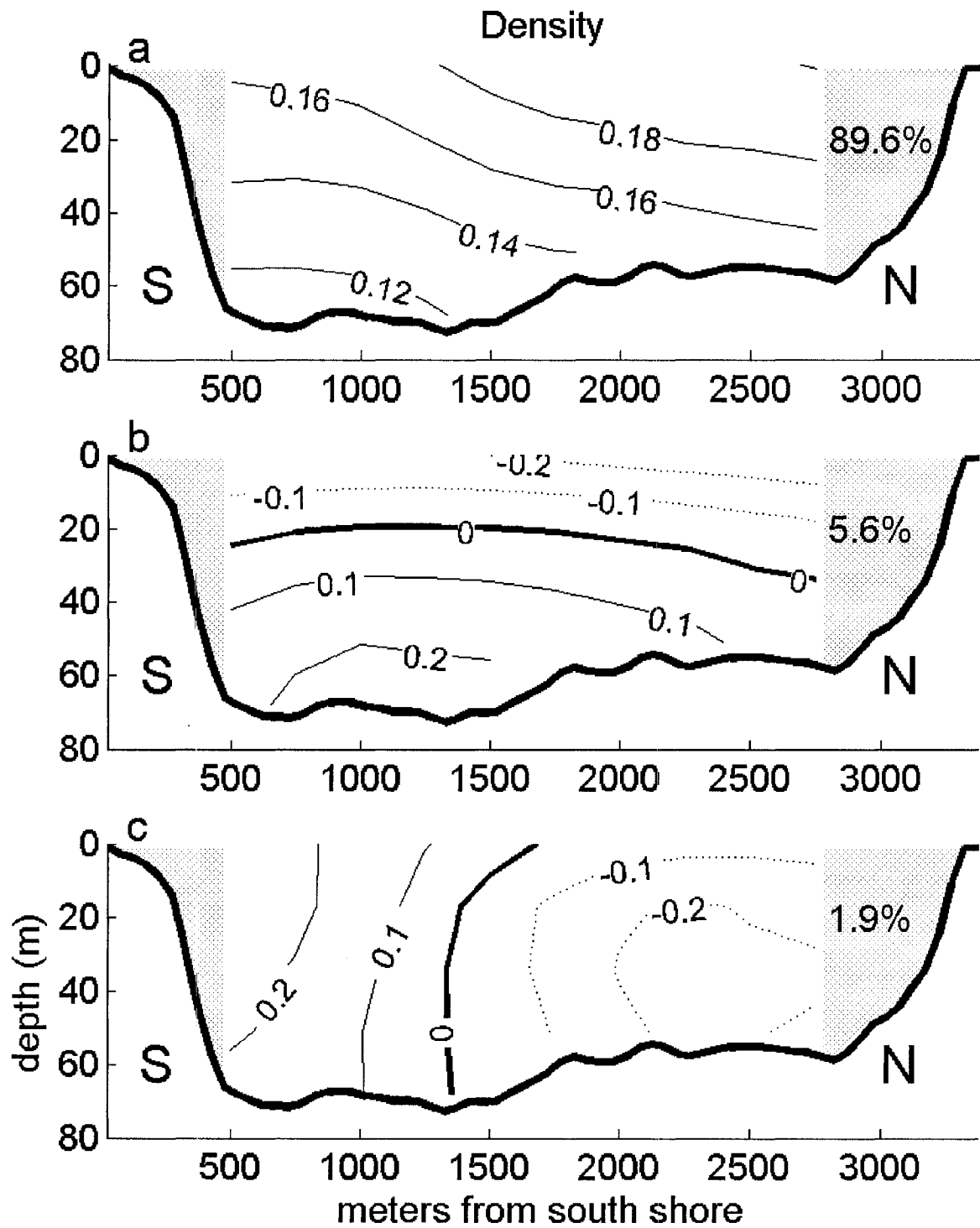


Figure 4.3: Density EOFs

The first three density EOFs are listed in order of the variance percentage explained by each EOF.

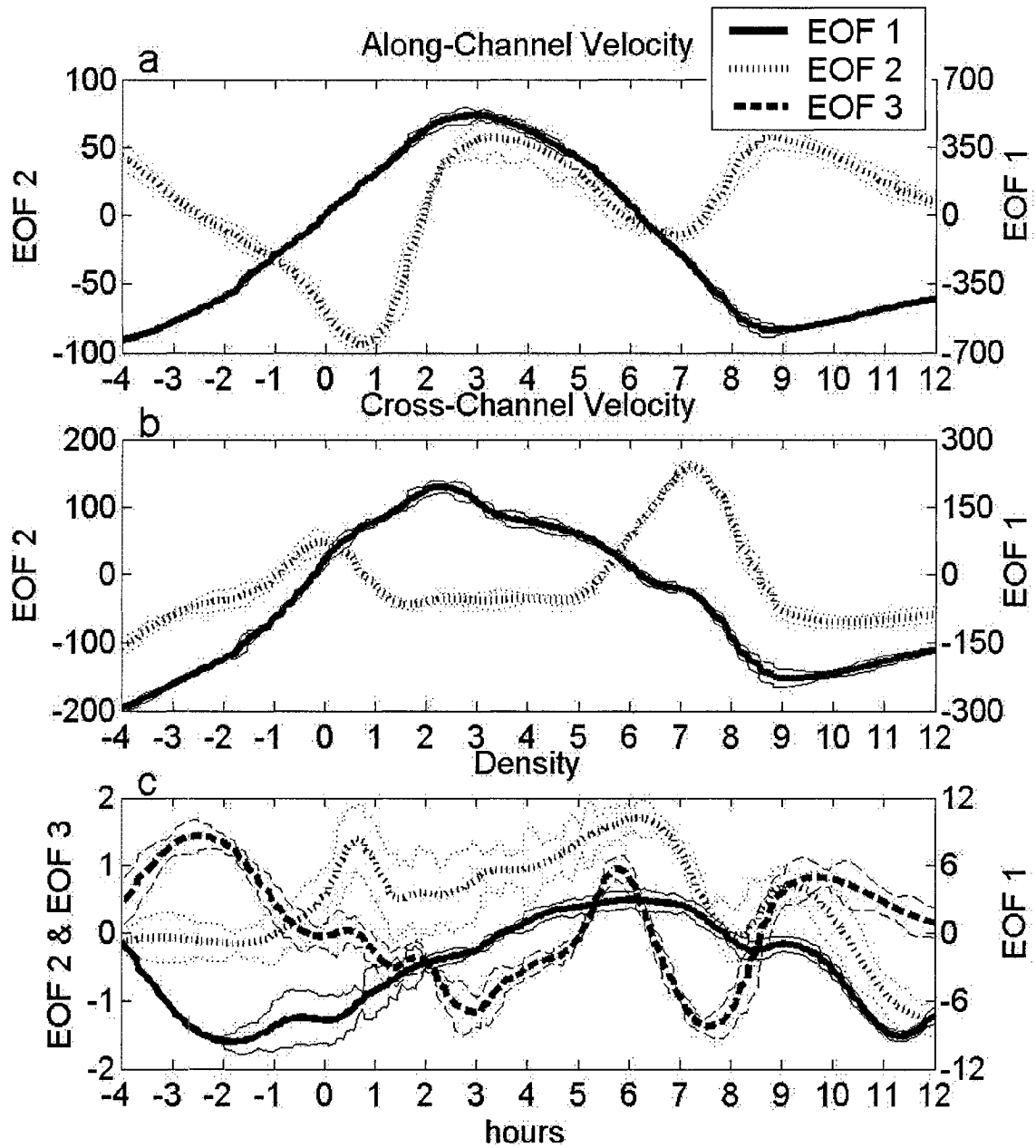


Figure 4.4: Tidally Aligned EOF Time Series

Data for empirical orthogonal functions are lined up by the semi-diurnal zero crossings of the seaward barotropic signal, and then block averaged within windows of approximately 15 minutes. Error bounds show the standard deviation of the mean for the high-frequency residuals within each window.

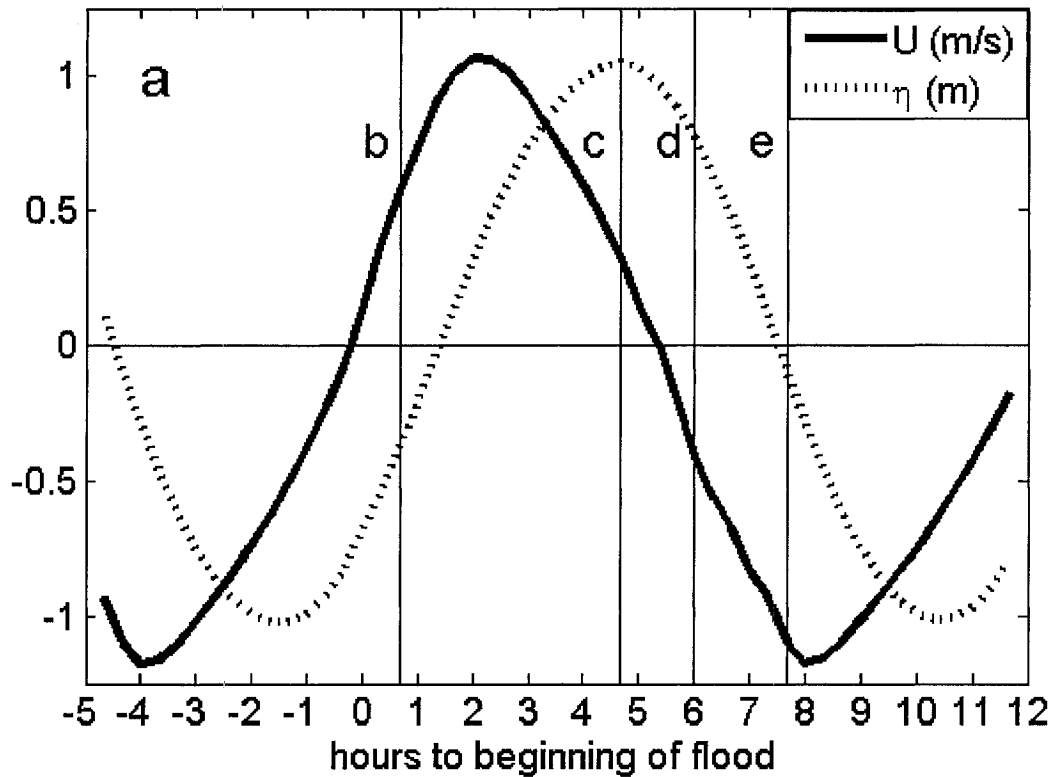
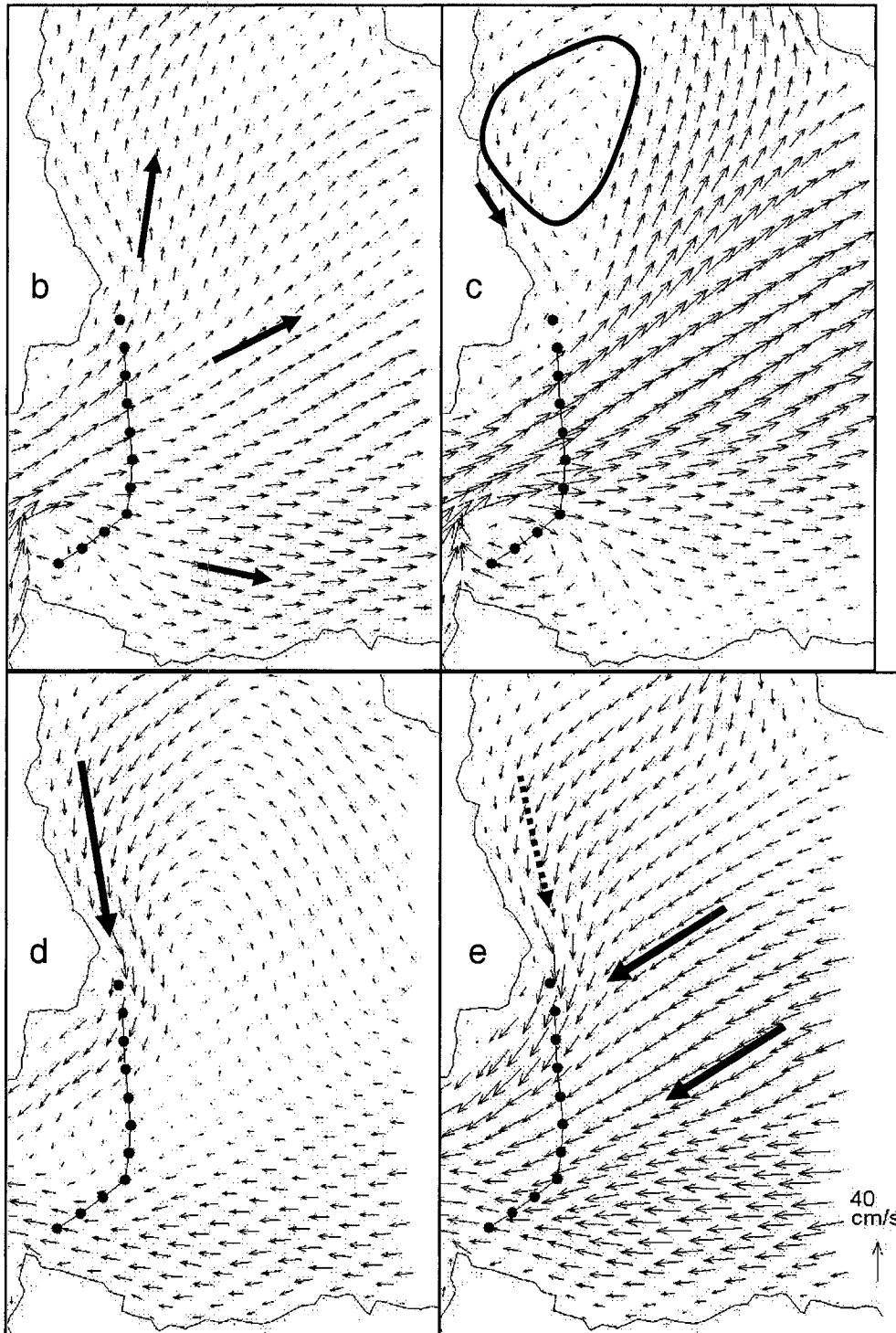


Figure 4.5: Modeled Velocity

(a) Modeled results are plotted with respect to the same time axis as the tidally aligned time series of the measured data (figures 4.4, 4.6, and 4.8). The tidal phase of each snapshot (b-e) can be found from the tidal elevation ( $\eta$ ) and cross-section along-channel velocity ( $U$ ) subfigure (a). Subfigure (b) occurs during the first half of flood tide, in which flooding across the entire channel. In subfigure (c), eddy develops during the second half of flood tide. The eddy persists into the beginning of ebb tide in subfigure (d). Near maximum ebb tide the eddy's effect ceases, as show in subfigure (e). Arrows in subfigures b through e are spaced 200m apart.



(The caption for figures 4.5b-4.5e is on the previous page.)



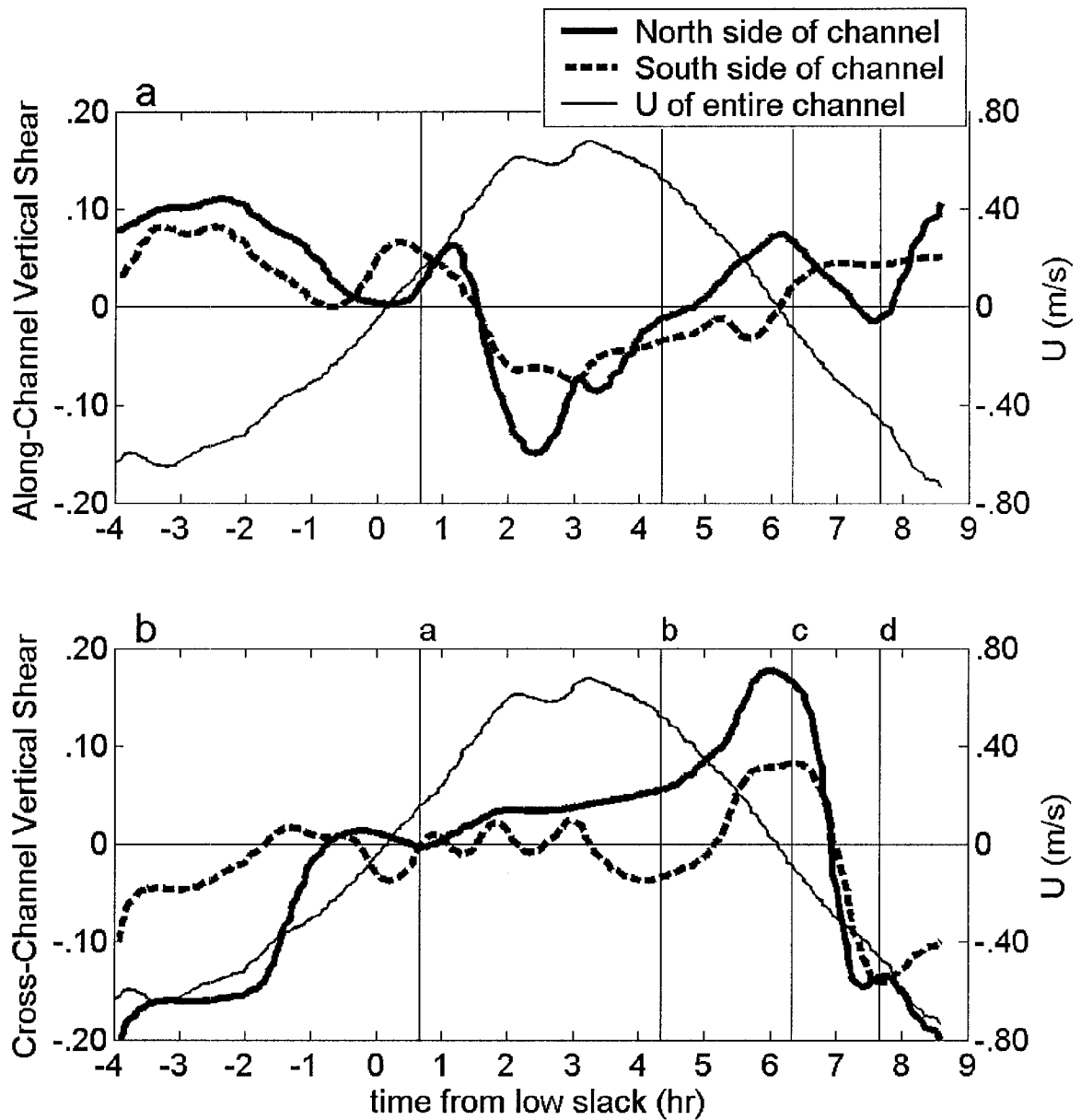


Figure 4.6: Measured Vertical Shear

Along-channel and cross-channel vertical shear data are lined up by the semi-diurnal zero crossings of along-channel mean velocity, and then block averaged. Three-dimensional features in these data illustrate how the tides interact with the sill on the north side of the channel. For example, there is more along-channel vertical shear on the north side of the channel during ebb tide after the passing of the Point Cavallo eddy. Vertical lines correspond to model snapshot times from figure 4.5.

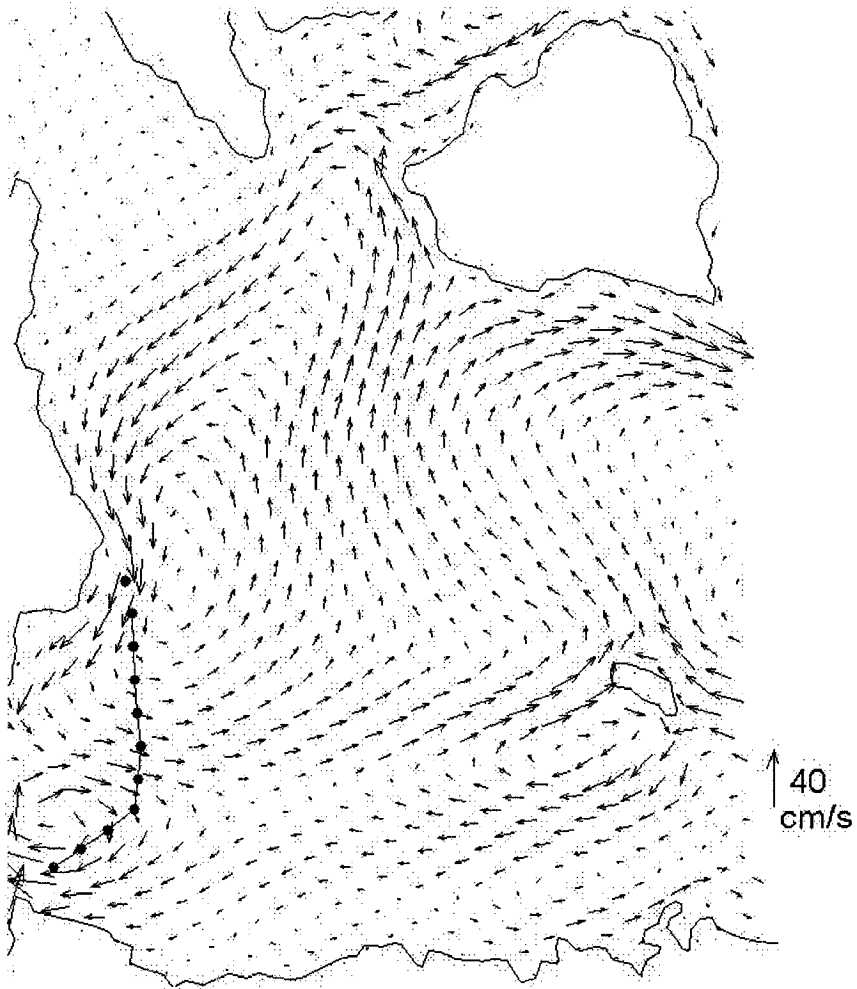


Figure 4.7: Modeled 2D Residual Velocity

Average velocity over 5 M2 modeled tidal cycles. 200m spacing.

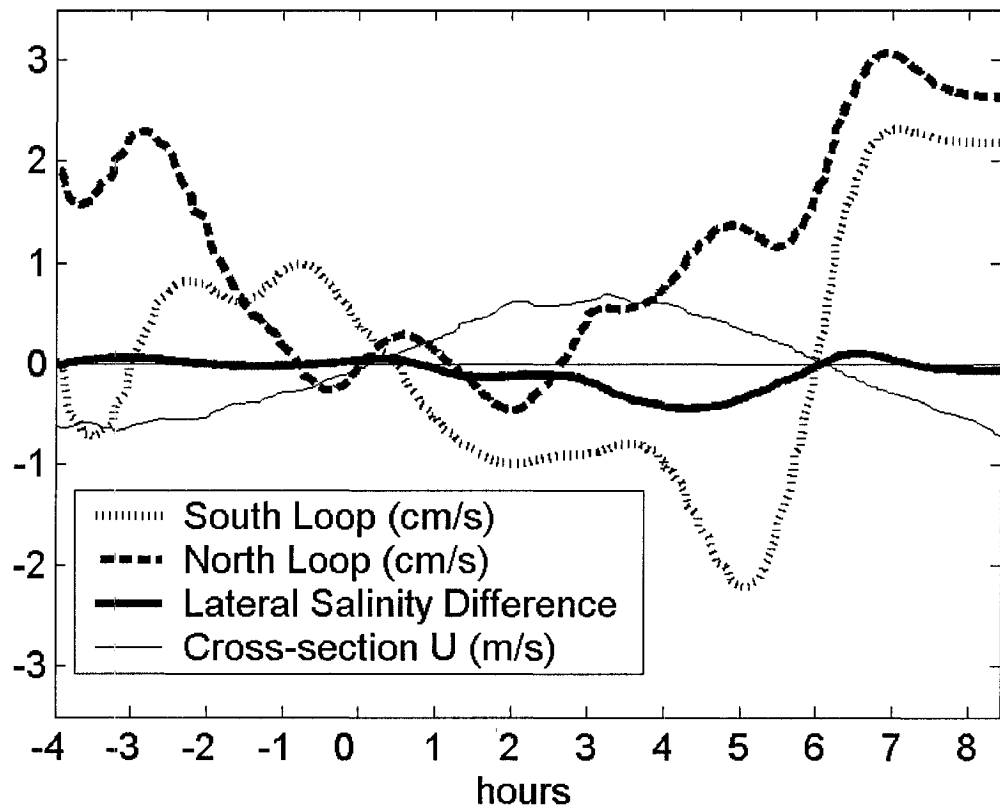


Figure 4.8: Measured Circulation Data

In the second half of flood tide, there are two opposing axial circulation cells associated with a higher salinity in the center of the channel. The velocity scale of each cell is the circulation divided by the circumference of the cell. This density-driven circulation shuts off at the beginning of ebb tide, when the circulation on north side strengthens and on the south side reverses because of influence by a headland eddy and flow around the Point Cavallo sill.

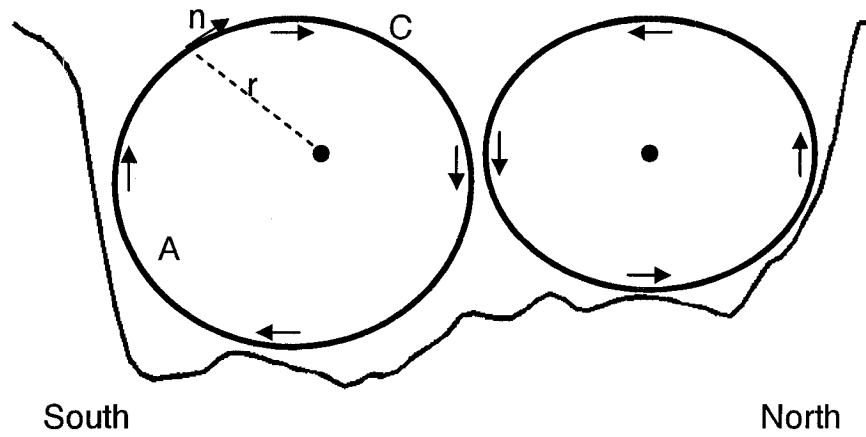


Figure 4.9: Circulation Schematic

In the coordinate system for this and the previous figure, the south side has negative circulation and the north side has positive circulation.  $r$  is the radius of an axial circulation,  $C$  is the circumference, and  $A$  is the Area.

## 5 Residual Flow

### 5.1 Relevant Forcing Mechanisms

Residual flows are found from averages over relevant scales of variability. For example, the cross-section mean velocity changes by over a meter per second every six hours, so one must average over complete M2 tides to characterize net flow. There are many other temporally variable forcing mechanisms at the Golden Gate. We will compare the effect several of them to isolate which ones are important for inclusion in our residual flow calculations.

To compare the effect of each forcing mechanism, we look at the relative magnitudes of each forcing term in the along-channel momentum equation:

$$\frac{\partial u}{\partial t} + u \frac{\partial u}{\partial x} = -g \frac{d\eta}{dx} - \int_{-H}^0 \frac{g}{\rho} \frac{d\rho}{dx} dz + fv + \frac{1}{\rho} \frac{\partial \tau_b}{\partial z} + \frac{1}{\rho} \frac{\partial \tau_s}{\partial z} \quad (23)$$

The mean tidal range is 1.24m and tidal elevation is 90 degrees out of phase 70km inland from the Golden Gate [Walters *et al.*, 1985], so the acceleration scale from tidal forcing is:

$$-g \frac{d\eta}{dx} = 9.81 \frac{m}{s^2} \frac{1.24m}{70km} = 1.8 \cdot 10^{-4} \frac{m}{s^2} \quad (24)$$

At the transect path, a typical along-channel density gradient is  $0.19 \text{ kg m}^{-3} \text{ km}^{-1}$  (table 5.1) and the mean depth is 55m, so the density-driven acceleration scale is:

$$\frac{gH}{\rho} \frac{d\rho}{dx} = \frac{9.81 \frac{m}{s^2}}{1020 \frac{kg}{m^3}} 55m \cdot 0.19 \frac{kg}{m^3 km} = 1.0 \cdot 10^{-4} \frac{m}{s^2} \quad (25)$$

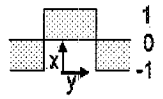
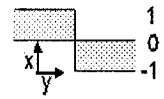
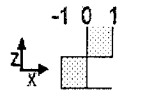
	Tidal pumping lateral shear $\overline{\gamma U(y) - \bar{U}} \left[ \frac{\text{cm}}{\text{s}} \right]$	Along-channel density gradient $\frac{d\rho}{dx} \left[ \frac{\text{kg}/\text{m}^3}{\text{km}} \right]$	Ebb cross-transect density gradient $\overline{\gamma \rho(y) - \bar{\rho}} \left[ \frac{\text{kg}}{\text{m}^3} \right]$	Cross-section mean RMS velocity [cm/s]	Predicted baroclinic velocity (eq. 32) $U_{BC}$ [cm/s]	Measured along-channel vertical shear $\overline{\gamma U(z) - \bar{U}} \left[ \frac{\text{cm}}{\text{s}} \right]$
Fall	12.4	0.06	0.04	46	1.3	2.4
Spring	14.2	0.19	0.16	53	3.4	5.0
Summer	11.9	0.19	0.19	45	3.9	3.9
$\gamma$						

Table 5.1: Baroclinic Scaling Data

At 38 degrees latitude, the Coriolis parameter,  $f$ , is  $9 \cdot 10^{-5} \text{ s}^{-1}$ . In more stratified, straighter estuaries Lerczak and Geyer [2004] show through a model that geostrophy may create lateral circulation. By their analysis approach, this lateral circulation has a magnitude of only a few millimeters per second at the Golden Gate. Integrating over a flood or ebb tide, this results in only as much as a 100m lateral deflection of the tidal currents, much less than bathymetrically induced flow asymmetries.

During summer afternoons winds reach their highest average speed of  $8 \text{ m s}^{-1}$  [Conomos, 1979], driving an order of magnitude smaller acceleration in the channel than from density-driven forcing during the fall-relaxation season, and an even smaller acceleration with respect to tidal forcing.

$$\frac{1}{\rho} \frac{\partial \tau_s}{\partial z} = \frac{C_{10} \rho_{\text{air}} U_{\text{wind}}^2}{H \rho_o} = \frac{0.002 \cdot 1.23 \frac{\text{kg}}{\text{m}^3} \cdot \left(8 \frac{\text{m}}{\text{s}}\right)^2}{55\text{m} \cdot 1020 \frac{\text{kg}}{\text{m}^3}} = 2.8 \cdot 10^{-6} \frac{\text{m}}{\text{s}^2} \quad (26)$$

We do not consider wind-driven residual flow to be significant because tidal and density-driven forcing are so much larger.

Solar forcing can contribute to residual flow by creating stratification, which can promote shear through SIPS. However, we can show that at the Golden Gate solar heating does not contribute a meaningful portion of the stratification on the tidal timescale. From Fischer [1979], the surface mixed layer is related to the net radiation, water heat capacity, density, and mixed layer depth. The nearest incoming radiation measurements are collected every 15 minutes at the San Francisco Airport, which, while only 30 km from the Golden Gate Bridge, is less foggy than the Golden Gate. These radiation measurements should serve as reasonable maximum values. Assuming a 10m surface mixed layer:

$$\Delta\rho = \frac{\beta \bar{H}t}{C_p \rho H_{sml}} = \frac{.21 \frac{\text{kg}}{\text{m}^3} 440 \frac{\text{W}}{\text{m}^2} 36,000 \text{sec}}{4179 \frac{\text{J}}{\text{kg}^\circ\text{C}} 1020 \frac{\text{kg}}{\text{m}^3} 10\text{m}} = .08 \frac{\text{kg}}{\text{m}^3} \quad (27)$$

This is ~5% of spring and summer stratification, and ~20% of fall stratification. However, the effect of solar heating on stratification is likely to be smaller than these percentages because of vertical mixing. Thus, not surprisingly, surface and Acrobat temperature to salinity relationships are indistinguishable. Solar forcing contributes a small amount to daily residual flow variability at the Golden Gate.

On longer time scales, solar forcing does significantly change the character of water masses passing through the Golden Gate. Winter freshets can be cooler than the ocean, but generally the shallow bay waters are warmer. Water retained in the South Bay is always warmer than both North Bay and oceanic waters because of solar heating. South Bay, with a mean depth of 4.6m, is shallower than the rest of the bay (10.7m,

<http://sfbay.wr.usgs.gov>) and the retention time of water in South Bay is longer than for the rest of the bay [*Uncles and Peterson, 1996*]. The influence of density gradients caused by solar heating of South Bay on residual flow will be discussed in sections 5.3.5 and 5.4.

It would be interesting to measure exchange on the freshet time scale to characterize the estuarine adjustment time [*MacCready and Geyer, 1999*]. Monismith et al. [2002] show that it takes about 12 days for the north side of the estuary (from Delta outflow to the Golden Gate) to adjust its salt fields to a storm freshet. However, the data used for this analysis is sparse near the Golden Gate, so it has not yet been shown how freshet pulses are phased with exchange increases at the Golden Gate. It would not be possible to run transects continuously for 12 days, nor could one complete transects during a storm. Over the course of single day field campaigns, freshet effects are visible from USGS moored salinity time series data as slow (linear in time) changes to the along-channel salinity gradient.

## **5.2 Residual Fields**

Figure 5.1 shows the means over all transects of along-channel velocity, cross-channel velocity, and density. The contour plots are of forty-one 17x250m blocks instead of the 45 mentioned in the previous section because the spring experiment data are included. The spring experiment did not include the northern 250m of the transect path that was included in the summer and fall data sets, and blocks without data during the spring season are not shown in figure 5.1. The landward residual flow pattern (figure 5.1a) is



indicative of flood jet-ebb drain asymmetry, with net landward flow in the center and seaward flow on the north and south sides. Net flow towards the center in the cross-channel residual (figure 5.1b) is also part of the jet-drain asymmetry. The stronger net southward flow trend across the grid is due to local bathymetry and will be discussed in the modeling section. In terms of vertical trends, flow is somewhat more seaward at the top and into the bay at the bottom, consistent with the expected baroclinic circulation.

The lateral density gradient (estimated from figure 5.1c),  $\left(\frac{\partial\rho}{\partial y}\right)$ , is largest towards the north shore, from a combination of South Bay-North Bay differences and the jet-drain asymmetry reducing density on the channel sides. Density, which we calculate from the seawater EOS Matlab toolbox, is a function of salinity, temperature, and depth, although in this experiment (as in most estuaries) it is mainly a function of salinity. We plot density instead of salinity or temperature because density is dynamically more important than salinity or temperature for driving residual flow. Additionally, temperature and salinity have similar signals (figure 3.5). In contrast, salinity will be discussed more than density in chapter 6 because salt exchange is that chapter's main topic. Considering all three of the residual fields together, one can see the impact of residual flow on exchange. The jet-drain asymmetry creates net seaward flow of fresher water through the transect sides and net landward flow of saline water through the transect center.

### **5.3 Residual Flow Mechanisms**

#### **5.3.1 Quantifying Mechanisms**

As has been demonstrated in the preceding sections of this chapter, the residual flow structure at the Golden Gate includes shears of along-channel velocity in both the vertical and lateral directions. The magnitudes of these shears and the quantities that influence them are summarized in table 5.1 for each of the three seasonal conditions (spring, summer, and fall). Along-channel lateral shear is dominated by the jet-drain asymmetry, so it is quantified as the mean of the residual lateral deviation from the cross-section mean times the cross-channel sign of the jet-drain residual structure ( $\gamma$  in table 5.1). Cross-transect density gradients and along-channel vertical shear are quantified similarly from the spatial variability of temporal averages. The along-channel density gradient is:

$$\frac{d\rho}{dx} = \frac{1}{U} \frac{d\rho}{dt} \quad (28)$$

where  $\rho$  and  $U$  are cross-sectionally averaged quantities and the time derivative is estimated through a first-order finite difference. Vertically-sheared residual flow is strongest during the spring experiment and weakest during the fall experiment, with the summer experiment falling between these two values. The fall experiment had the smallest values, consistent with its weak along-channel density gradient and small freshwater flow. The spring and summer along-channel density gradients, however, have similar values, with temperature contributing more to the density variability in the summer (table 3.1) due to cold oceanic conditions around the height of summer upwelling (<http://www.pfeg.noaa.gov>). In the following sections we will show that four mechanisms cause our observed lateral and vertical residual shear: tidal pumping, traditional density-driven circulation, sill-induced vertical shear, and vertical shear due to the cross-channel density gradient.

### 5.3.2 Lateral Shear from Tidal Pumping

Based on the modeling analysis in 4.3, as well as the tidal pumping structure defined in 1.5.2.1 and described in several earlier sections, we expect lateral shear to be caused by tidal processes. Mean along-channel velocity is seaward at the edges and landward in the center for each season. The results in table 5.1 are consistent with this expectation: summer and fall lateral shear have similar magnitudes, which underscores the density independence and tidal dependence of the mean lateral shear; the spring value is 15-20% larger than summer and fall's because the root-mean-square tidal velocity,  $U_{rms}$ , is 15-20% larger during this season. This is consistent with Stommel and Farmer's [1952] picture of jet-drain exchange (figure 1.4). Velocity at any point within the jet or drain scales linearly with  $U_{rms}$ . Specifically, if velocity at the mouth is:

$$U_{mouth} = U_o \sin\left(\frac{2\pi t}{T}\right) \quad (29)$$

where  $U_o$  is the maximum velocity and  $T$  is the tidal period, then the velocity at any point in the jet during flood is:

$$U_{jet} = U_{rms} \sqrt{2} \sin\left(\frac{2\pi t}{T}\right) \quad (30)$$

In Stommel and Farmer's development, the ebb tide velocity is presented as a radial drain that fills an entire half-circle (i.e., the channel walls make a 90 degree angle as they enter an infinitely wide bay). In reality, particularly at our site, the ebb tide potential flow is also constrained by the local bathymetry, and is more accurately represented by a conically shaped bay (with apex angle  $\theta$ , figure 5.2a). For this case, the ebb drain velocities along-channel and cross-channel are:

$$U_{\text{drain}} = \frac{U_{\text{rms}} a \sqrt{2} \sin\left(\frac{2\pi t}{T}\right)}{\theta \cdot (r_b + d_t)} \cos \varphi \quad (31)$$

$$V_{\text{drain}} = \frac{U_{\text{rms}} a \sqrt{2} \sin\left(\frac{2\pi t}{T}\right)}{\theta \cdot (r_b + d_t)} \sin \varphi \quad (32)$$

where  $r_b$  is the radial distance to a virtual mouth for the radial flow and  $d_t$  is the actual distance from the mouth to the transect path. For our transect path, the apex angle is 56 degrees, the distance from the apex to the Golden Gate Bridge ( $r_b$ ) is 2.1km, and the distance from the bridge to the transect path ( $d_t$ ) is 1.1km. These residual flows increase linearly with  $U_{\text{rms}}$ , making mean lateral shear of along-channel velocity also scale linearly with  $U_{\text{rms}}$ .

We can model the time variability of velocity along our transect path by assuming a sinusoidal velocity at the mouth (equation 29), and a flood tide velocity given by (30) and an ebb tide velocity given by (31 and 32). This simple model picks up many features of our data (figure 5.2b,c). In the along-channel direction, the center floods much faster than the sides, but the sides have some along-channel velocity early in the flood tide. As the jet develops and separates from the sides during the latter part of the flood, however, the velocity along the sides drops to near zero, which is consistent with the simple jet-drain model presented here. During ebb tide, this simple model underestimates the lateral shear by both overestimating the velocity along the edges and underpredicting the velocity in the center, which is a result of the fact that friction does not act uniformly during the ebb due to the depth variations across the channel. In the cross-channel

direction, the model predicts zero cross-channel flow during flood tide, but clearly the jet spreads laterally due to the interaction of the flood tide jet with the local bathymetry, which creates non-zero cross-channel velocities across most of the channel. On ebb, flow is much stronger on the north side than on the south, whereas the model predicts a lateral symmetry. This is likely due to the eddy structure that was discussed in section 4.3. As such, we conclude that the traditional jet-drain description of tidal exchange is appropriate as a rough estimate, and is altered due to the complex bathymetry at the site.

Comparing the data to the traditional jet-drain description highlights flow differences from the first to the second half of flood tide. In the first half of flood tide the jet spreads radially. Then the jet focuses in the center of channel and separates from the sides. The central jet moves across rather than around the central peak of the sill during the second half of flood tide. From the oblique photography, starting at max flood surface features such as instabilities and along-channel fronts form at the center peak of the sill and the south tower. The change in flow pattern between the two halves of flood tide also leads to axial circulation in the second half of flood tide (section 4.4). The author found the source of this transition while making visual observations from the Marin Headlands in fall 2003. During the second half of ebb tide, a tidally trapped eddy forms southwest of the bridge (south of Fort Point along Baker Beach to Lands End). It is not until max flood that this eddy crosses underneath the bridge, releasing the central jet from the south shore. This Baker Beach eddy has been described by Rubin and McCulloch [1979]. At the same time, the north side of the jet separates eastward off Point Cavallo instead of just steering northward into Richardson Bay and Raccoon Strait.

### 5.3.3 Traditional Density Driven Shears

To isolate the sources of residual vertical shear, we first consider steady baroclinic circulation. The velocity scale for this residual flow process derives from a balance between density forcing and tidally-induced mixing [e.g. *Dyer, 1997*]:

$$\overline{|U(z) - \bar{U}|} = U_{BC} = \frac{.011g \frac{d\rho}{dx} H^3}{\rho_o \nu_t} \quad (33)$$

where  $\nu_t = 0.067\sqrt{C_d}U_{rms}H$  [*Fischer et al., 1979*]. By this formula, the vertical shear should be reduced during strong tidal forcing, with maximum values of the baroclinic circulation during weak tidal forcing [*Bowen and Geyer, 2003*]. In our case, however, vertical shear increases with tidal energy (table 5.1, comparing spring and summer  $U_{rms}$ ), suggesting that physical processes other than steady baroclinic exchange are likely to contribute to vertical shear in the residual flow.

A residual flow field with similar vertical structure to baroclinic flow can also be created through SIPS [*Simpson et al., 1990*]. A dimensionless group that is indicative of the importance of this process to residual flow is the horizontal Richardson number:

$$Ri_x = \frac{g \frac{d\rho}{dx} H^2}{\rho_o U_*^2} \quad (34)$$

Modeling results have shown that the critical value of this parameter is about 0.3 or 0.4, while field results in northern San Francisco Bay suggest a slightly higher  $Ri_{xcrit}$  of 0.5 [*Monismith et al., 1996; Monismith et al., 2002*]. Estimates of  $Ri_x$  for the spring and summer experiments (0.4 and 0.5) are around the critical value while  $Ri_x$  is 0.16 during

fall, which would suggest that SIPS may be an important process for establishing residual vertical flow during spring and summer, but not during fall. However, the stratification event during spring and summer that appears to trigger residual flow (figure 5.3, discussed below) follows a period of small vertical shear in the along-channel velocity, indicating this stratification must be created by a process other than longitudinal straining. In the traditional model of SIPS, the degree of stratification, and therefore the strength of residual flow it creates, varies inversely with tidal forcing [*Stacey et al.*, 2001], just as the baroclinic velocity scale does. Therefore, the strength of this residual flow in spring and summer is the reverse of what is expected based on the SIPS mechanism. In order for periodic stratification to contribute to this residual shear, we require a stratifying mechanism that increases in strength with tidal forcing; we consider such a mechanism in section 5.3.5.

#### **5.3.4 Sill Induced Vertical Shear**

The sill on the north side of the channel induces a net vertical shear consistent with the residual flow. The ebb tide flow is sheared by its interaction with the sill, while the flood tide jet has less interaction with the sill due to its position primarily to the south of the sill. The result is a vertically sheared residual flow profile that is directed down-estuary at the surface. Residual vertical shear from this mechanism should scale linearly with  $U_{rms}$  for the same reasons as outlined above for the lateral tidal pumping shear. However, summer experiment residual vertical shear is 30% less than in spring, while summer  $U_{rms}$  is only 15% less (table 5.1). This discrepancy may be due to experimental uncertainty as well as difficulties in accounting for spring sampling deficiencies. The

spring shear result reflects our estimation of the effect of a shorter transect path and stronger ebb than flood tidal velocities during the spring experiment. Comparing summer and fall data sets, stratification appears to have a small effect on sill-induced shear by altering the shape and timing of the Point Cavallo eddy. Velocity fronts at the boundary of the eddy are stronger and the eddy cross the transect path earlier in the tidal cycle during summer, which combine to slightly increase the amount of time during ebb that flow is directed across the sill. The details of this phasing are developed in chapter 6.

### **5.3.5 Shear by Asymmetric Frictional Phasing**

The dynamics that create a second large source of residual vertical shear are summarized in figure 5.3. A pulse of vertical shear is created at the start of the flood tide (label 'd' in figure 5.3), which is a result of the flood tide beginning first at the bed. The vertical mixing of this flood jet, which eventually reduces and eliminates the vertical shear, is slowed by vertical stratification that develops around slack water (label 'c'). To evaluate the mechanism that creates this stratification, figure 5.3 also includes the along-channel and cross-channel vertical shears. The stratification peak is seen to follow a minimum in along-channel vertical shear, and a peak in lateral vertical shear (label 'b'), suggesting it is a lateral flow that creates the stratification at slack water. The lateral flow that stratifies the water column is preceded by the development of a lateral density gradient (label 'a'). The lateral density gradient is a result of the multiple water masses that are mixing in the environment (figure 3.5). As the ebb tide progresses, the north side of the channel freshens further than the south side, with the eventual density gradient depending on the tidal excursion and the difference in the two longitudinal density gradients.



At the end of the ebb tide, turbulent mixing is reduced as the tide decelerates and the lateral density gradient relaxes across the channel. As a result, the lateral vertical shear peaks during spring and summer for 1-2 hours starting at the end of ebb, which is approximately one hour after the lateral density gradient peak (label ‘b’). The dynamics of this lateral exchange are described by:

$$\frac{\partial V}{\partial t} = \frac{g}{\rho_0} \frac{\partial \rho}{\partial y} (H - z) + \frac{\partial}{\partial z} \left( v_t \frac{\partial V}{\partial z} \right) \quad (35)$$

the steady baroclinic scaling from equation 33, but with the lateral density gradient replacing the longitudinal. Based on the measured parameters, we expect this exchange velocity to have a magnitude of approximately  $15 \text{ cm s}^{-1}$ , which is consistent with the observed peak magnitude ( $\sim 11 \text{ cm s}^{-1}$ ). To evaluate the time it would take for this steady balance to be reached, we consider the acceleration of the flow by the baroclinic pressure gradient (balancing the first two terms in equation 35). The resulting timescale for this flow to develop is estimated to be 30 minutes based on a constant acceleration from the baroclinic pressure gradient, which is also consistent with the timescale for vertical mixing (an estimate of the time for the third term to be significant). The magnitude and timing of the stratification peak ( $\sim 0.6 \text{ PSU}$ ) agrees well with the integration of the product of lateral vertical shear and the lateral density gradient.

Even in an unstratified water column, however, there will be a vertical phase lag in the tidal velocities due the timescale for vertical mixing [*Simpson et al.*, 2000]. The presence of stratification limits vertical mixing of momentum and strengthens the frictional

phasing, leading to enhanced vertical shear. Starting from the along-channel momentum balance, assuming that vertical variability and barotropic forcing dominate, we have:

$$\frac{\partial u}{\partial t} = -g \frac{\partial \eta}{\partial x} + \frac{\partial}{\partial z} \left( v_t \frac{\partial u}{\partial z} \right) \quad (36)$$

As an initial estimate, we can use Munk and Anderson's [1948] Richardson Number parameterization of the effect of stratification on mixing to show that the vertical turbulent viscosity,  $v_t$ , is 55% less in summer than fall, which would increase the phase lag by about a factor of two in the summer relative to the fall. In order to examine the development of shear at the transition to flood tide in more detail, we integrate the along-channel momentum equation over two layers: the lower layer extending from the bottom ( $z=0$ ) to a height  $h$ , and the upper layer extending from  $z=h$  to the surface at  $z = H$ . The equations for the layer-averaged velocities are:

$$\frac{\partial u_{\text{bot}}}{\partial t} = -g \frac{\partial \eta}{\partial x} + \frac{v_t}{h} \frac{\partial u}{\partial z} \Big|_h + \frac{v_t}{h} \frac{\partial u}{\partial z} \Big|_0 \quad (37)$$

$$\frac{\partial u_{\text{top}}}{\partial t} = -g \frac{\partial \eta}{\partial x} - \frac{v_t}{H-h} \frac{\partial u}{\partial z} \Big|_h \quad (38)$$

Finally, we can define the evolution of the shear between the two layers

( $\Delta u = u_{\text{top}} - u_{\text{bot}}$ ) as the difference between these two equations:

$$\frac{\partial \Delta u}{\partial t} = -\frac{Hv_t}{h(H-h)} \frac{\partial u}{\partial z} \Big|_h + \frac{u_*^2}{h} \quad (39)$$

where  $u_*^2 = v_t \frac{\partial u}{\partial z}$ . Bed stress and interfacial exchange are the two terms that define the evolution of the shear. Bed stress decelerates the lower layer without affecting the upper layer. Interfacial exchange homogenizes the two layers.

In an unstratified water column (e.g. during a flood tide), these two terms act in opposition, with the bed stress acting to create shear and the interfacial exchange acting to destroy it. The presence of stratification during the acceleration or deceleration of the tide reduces the magnitude of the interfacial term, leading to an increase in the along-channel shear. The dynamics captured by equation 39 are evident in figure 5.3, where the along-channel shear is tracking the barotropic forcing during the ebb tide until the stratification develops (at point “c”). At that point, the interfacial stress term is reduced, along-channel shear develops (at point “d”).

To evaluate this process more quantitatively, we adapt Monismith and Fong’s [1996] two-layer boundary layer thickness model to include the effect of tidal straining on stratification. Specifically, Monismith and Fong define the entrainment between the two layers following Sherman et al. [1978], and they model shear instability effects following Price et al. [1986]. After these processes are applied, we adjust the density according to advection of a linear density gradient; for example, in the bottom layer:

$$\rho_{\text{bot}}^{n+1} = \rho_{\text{bot}}^{n*} + u_{\text{bot}}^{n+1} (t_{n+1} - t_n) \frac{d\rho}{dx} \quad (40)$$

The model was run with the same mixing coefficients as Monismith and Fong, and this experiment’s depth, stratification, cross-sectional mean velocity, and phasing between the barotropic pressure gradient and cross-sectional mean velocity. The model is initialized with no shear at the beginning of the low slack stratification peak, which corresponds to a  $55 \text{ cm s}^{-1}$  ebb tide. It predicts that frictional phasing creates an  $11.4 \text{ cm s}^{-1}$  vertical shear peak in summer and only a  $4.9 \text{ cm s}^{-1}$  shear peak in fall, which is consistent with our data,

and confirms our understanding of the interaction of stratification with barotropic tidal forcing.

To summarize this process, vertically sheared residual flow is created by a periodic stratification event that occurs at the end of ebb tide and the associated shear during the early flood tide. This stratification results from the relaxation of a lateral density gradient that is defined by the differential advection of low-density waters during the ebb tide. As such, the strength of this gradient, and the strength of the resulting residual flow, depends directly on the strength of the tidal forcing, with larger tides resulting in larger lateral density gradients and stronger residual flow. More directly, this process scales with the cross-channel density gradient that is created during the ebbing tide. If freshwater input to

the estuary was constant in time, then  $\frac{d\rho}{dy}$  would vary linearly with  $\frac{d\rho}{dx}$ . However, as will

be shown in 5.4,  $\frac{d\rho}{dy}$  also varies seasonally with freshwater input, while  $\frac{d\rho}{dx}$  adjusts to

freshwater input changes within a few weeks. The tidal dependence of this process is the reverse of what is expected from baroclinic scaling or traditional SIPS-induced shear.

Large ebb tides advect large cross-channel density gradients to the transect path, increasing along-channel vertical shear.

### **5.3.6 Shear from Axial Circulation**

In section 4.4 it was shown that axial circulation created  $0.2\text{kg m}^{-3}$  of stratification during the second half of flood tide. Here we examine whether this extra stratification accentuates an along-channel shear at the end of flood, similar to, but in the opposite

direction of, the shear created at the end of ebb. First, however, we validate the values for the circulation velocity scale. Following Nunes and Simpson [1985] and analysis from section 5.3.5 (equations 33 and 35), we estimate cross-channel circulation velocity scale as  $1.2 \text{ cm s}^{-1}$  from a balance between the baroclinic pressure gradient and vertical mixing.  $1.2 \text{ cm s}^{-1}$  is in agreement with the measured velocity shown in figure 4.8. This is smaller than the low slack cross-channel circulation (section 5.3.5) for two reasons: there is less baroclinic forcing, and vertical mixing is higher because this event occurs through stronger phases of the tide.

$0.2 \text{ kg m}^{-3}$  of stratification is far less than the  $1.6 \text{ kg m}^{-3}$  loss of stratification expected from straining of the along-channel density gradient (using data in figure 5.3). Thus, axial circulation is only one of the reasons for the maintenance of stratification through flood tide. Even if it created  $1.6 \text{ kg m}^{-3}$  stratification, this mechanism would not significantly alter along-channel shear by increasing flood-ebb frictional phasing. The intruding Point Cavallo eddy makes ebb tide start at the surface instead of at the bed. If anything, this extra stratification would act in opposition to traditional frictional phasing by confining the eddy to the surface layer, allowing it to avoid obstruction by the main sill.

Momentum from the eddy swamps any along-channel shear effect from axial circulation during flood-ebb transitions.

### **5.3.7 Vertical Shear Source Comparison**

The proportion of vertical shear due to each source can be approximated from the fall and summer data in table 5.1. Steady baroclinic circulation scales linearly with  $\frac{d\rho}{dx}$ . For this

rough estimate we assume that the two other density-driven processes, traditional SIPS and asymmetric frictional phasing, also scale linearly with  $\frac{d\rho}{dx}$ . In contrast, sill induced vertical shear is not significantly density dependent. Thus,

$$\begin{aligned} U_{\text{VerticalShear}} &= k \frac{d\rho}{dx} + U_{\text{Sill}} \\ U_{\text{DensityDriven}} &= k \frac{d\rho}{dx} \end{aligned} \quad (41)$$

By comparing the fall and summer shear velocities and along-channel density gradients, we calculate that 21% of the residual vertical shear is density-driven in the fall experiment, while 46% of it is density-driven in the summer. Integrating over the wet and dry season vertical shear peaks in figure 5.3 (hours  $-0.5-2.5$ ), frictional phasing increases contribute  $0.5 \text{ cm s}^{-1}$  to the summer residual shear, which is one third of the density-driven shear. We argue, therefore, that sill-induced shear, asymmetric frictional phasing shear from the lateral density gradient, and traditional vertical shear producing processes all contribute significantly to residual vertical shear.

#### 5.4 Seasonal Variability of Residual Flow Dynamics

In this section, we consider the annual cycle of residual flow at the ocean-estuary boundary. The laterally sheared residual velocity was demonstrated to be a function of tidal forcing and independent of the density forcing (table 5.1). As such, it should be relatively independent of season. Furthermore, since both vertically-sheared and laterally-sheared residual flow depend directly on the strength of the tidal flows, we would expect an increase in ocean-estuary exchanges during spring tides and a decrease during neaps. Vertically sheared residual flow also depends on density forcing, as was

described in the previous sections. The remainder of this section examines how this vertical shear flow varies seasonally.

While most of the density-driven portion of the vertically sheared residual along-channel flow is created by the along-channel baroclinic pressure gradient  $\left(\frac{d\rho}{dx}\right)$ , it is also a function of the lateral density gradient in the Golden Gate channel, which is created by differential advection of salt during ebb tides. The strength of the resulting gradient is therefore a function of the tidal prism and the salinity distribution in Central Bay, specifically the difference between the salinity at the boundaries between Central Bay and North and South Bays. Uncles and Peterson [1996] used a modeling approach to evaluate the dynamics of salinity in San Francisco Bay at long timescales and concluded that the region around the Richmond-San Rafael Bridge (North Bay-Central boundary) responds to a freshwater pulse in approximately 10 days while the head (south end) of South Bay takes 50 days for its maximum salinity response, and there is a similar time lag in returning to background salinity. Therefore, while the along-channel density gradient in our field site just reflects the freshwater flow history of the previous few weeks, the cross-channel gradient also reflects flows from previous months.

To evaluate this expectation, we compile density measurements taken every 15 minutes from 1989 through 2002 (<http://sfbay.wr.usgs.gov/access/wqdata> 2004) into an average annual cycle. Figure 5.4 presents the density at Point San Pablo (two kilometers north of the Richmond-San Rafael Bridge), Presidio Shoal (adjacent to our transect path), and the San Mateo Bridge [South Bay (figure 1.5)]. The Point San Pablo to Presidio Shoal

gradient is equivalent to  $\frac{d\rho}{dx}$ , while the San Mateo Bridge to Point San Pablo difference is related to  $\frac{d\rho}{dy}$ . The key feature in the annual cycle is that summer density in South Bay remains depressed months after the runoff peak. Also, in the fall, evaporation raises South Bay density, which strengthens  $\frac{d\rho}{dy}$ . Inclusion of this lateral forcing, and the associated changes in residual shears, results in an annual cycle of density-driven vertical shear that is different from that predicted by traditional baroclinic scaling. Vertical shear from asymmetric frictional phasing augments density-driven vertical shear by a small percentage in summer and a large percentage in the fall.

At the same time, this annual cycle is modulated by short-term changes in Delta inflow. In our data collection, for example, even though freshwater flow was similar in spring and summer, the lateral gradient was greater in the summer than the spring. The key difference is that Delta inflow was dropping more rapidly during the week before our spring than our summer experiment. As a result, North Bay density was increasing faster during spring than summer, but the South Bay boundary density remained lower in spring than summer because it had not yet received information about this event, lowering cross-transect density gradients during spring.

## **5.5 Residual Flow Summary**

The evaluation of detailed velocity and salinity transects has allowed us to identify several mechanisms that create residual flow at the Golden Gate ocean-estuary interface.



In the lateral direction, on the landward side of the Golden Gate Channel, traditional tidal pumping creates an asymmetry in the tidal flows, with flow predominately into the estuary in the center and out of the estuary along the perimeter. This structure was reinforced by the creation of a large eddy during the flood tide that remained as a coherent structure into the beginning of the ebb tide. Because this residual flow is a result of tidal flows interacting with bathymetry, its lateral variability is largely independent of season, and provides a baseline value for the residual circulation. The vertically-sheared residual flow was more variable by season, with a maximum value occurring in the spring, and four mechanisms were identified that create this circulation. First, traditional baroclinic circulation and SIPS create residual flow that depends on the longitudinal (along-channel) density gradient. These two mechanisms explain the difference between summer and fall residual flows, but do not explain the maximum in vertical shear during the spring since the density gradients were similar in the spring and summer. Examination of the lateral (North-South) density gradient indicates that an additional source of periodic stratification is lateral baroclinic flow in the channel, which is established by the differential advection of salt into the channel from North Bay and South Bay waters. This stratification creates an additional source of residual flow that is active during spring: that is, an increase in the vertical phase lag of the tidal flows during the early portions of flood tide. The residual circulation at this complex site is therefore a result of the interaction of tidal flows, bathymetry and density forcing, with each of these three driving forces being significant contributors. Without considering all of these mechanisms, the annual cycle of residual exchange will not be properly predicted, particularly the maximum exchange that occurs during the spring season.

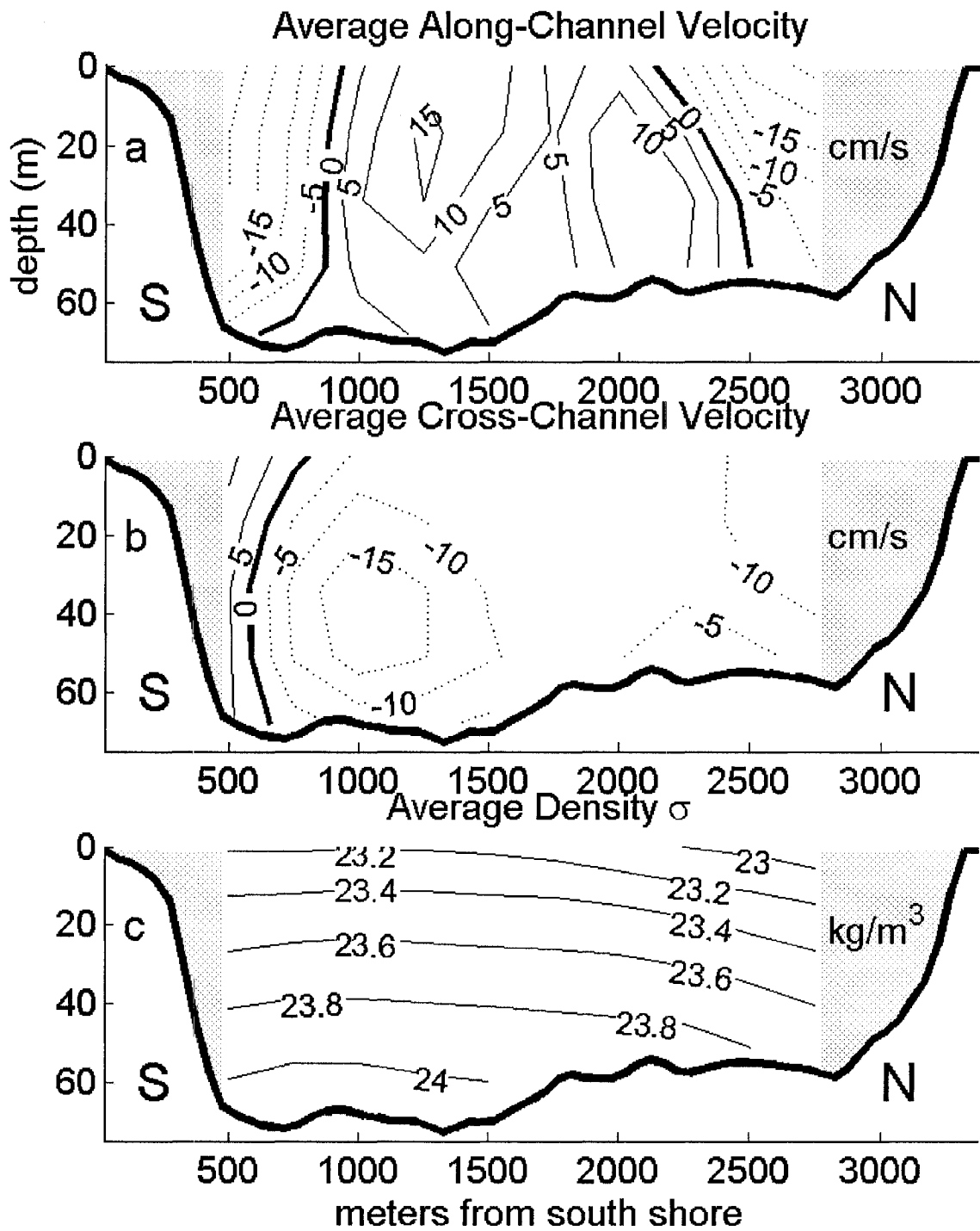


Figure 5.1: Average Velocity and Density

Average is over all data for all seasons. Positive velocity is into the bay and northward across the channel.  $\sigma$  is the water density minus the density of freshwater.

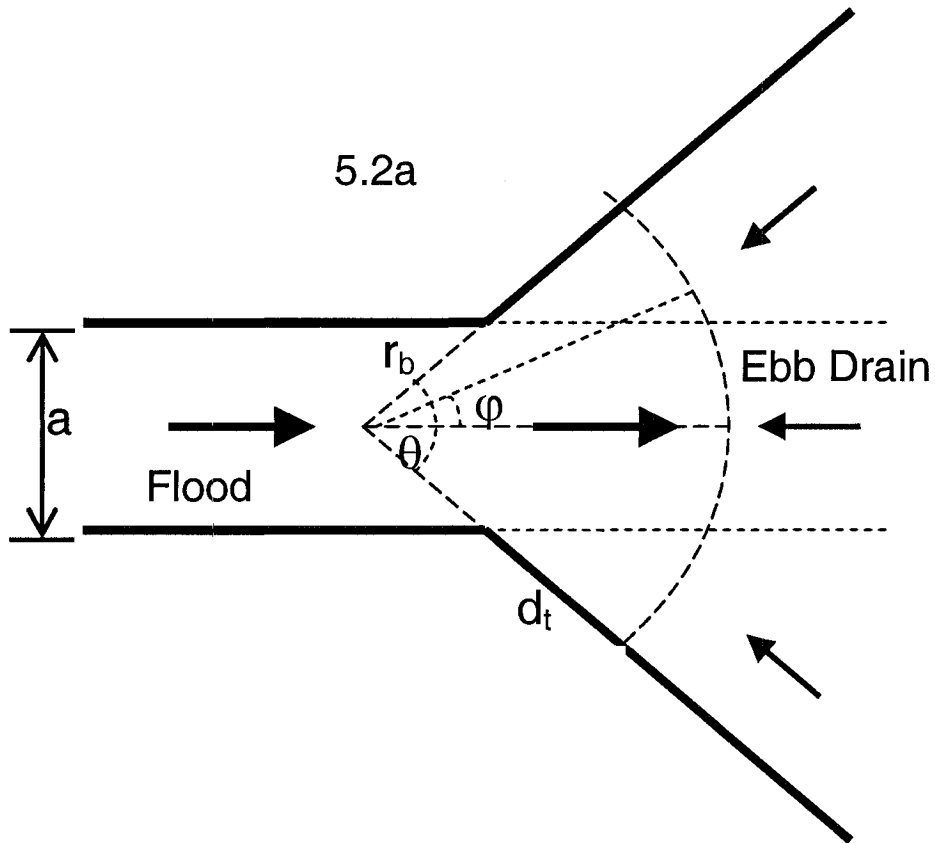


Figure 5.2a: Conical Tidal Pumping Schematic

The diagram is of tidal pumping between a channel and a conical embayment. As with figure 1.4,  $a$  is the width of the channel.  $r_b$  is the radial distance to a virtual mouth for the radial flow and  $d_t$  is the actual distance from the mouth to the transect path. The virtual mouth is defined by apex angle  $\theta$ .

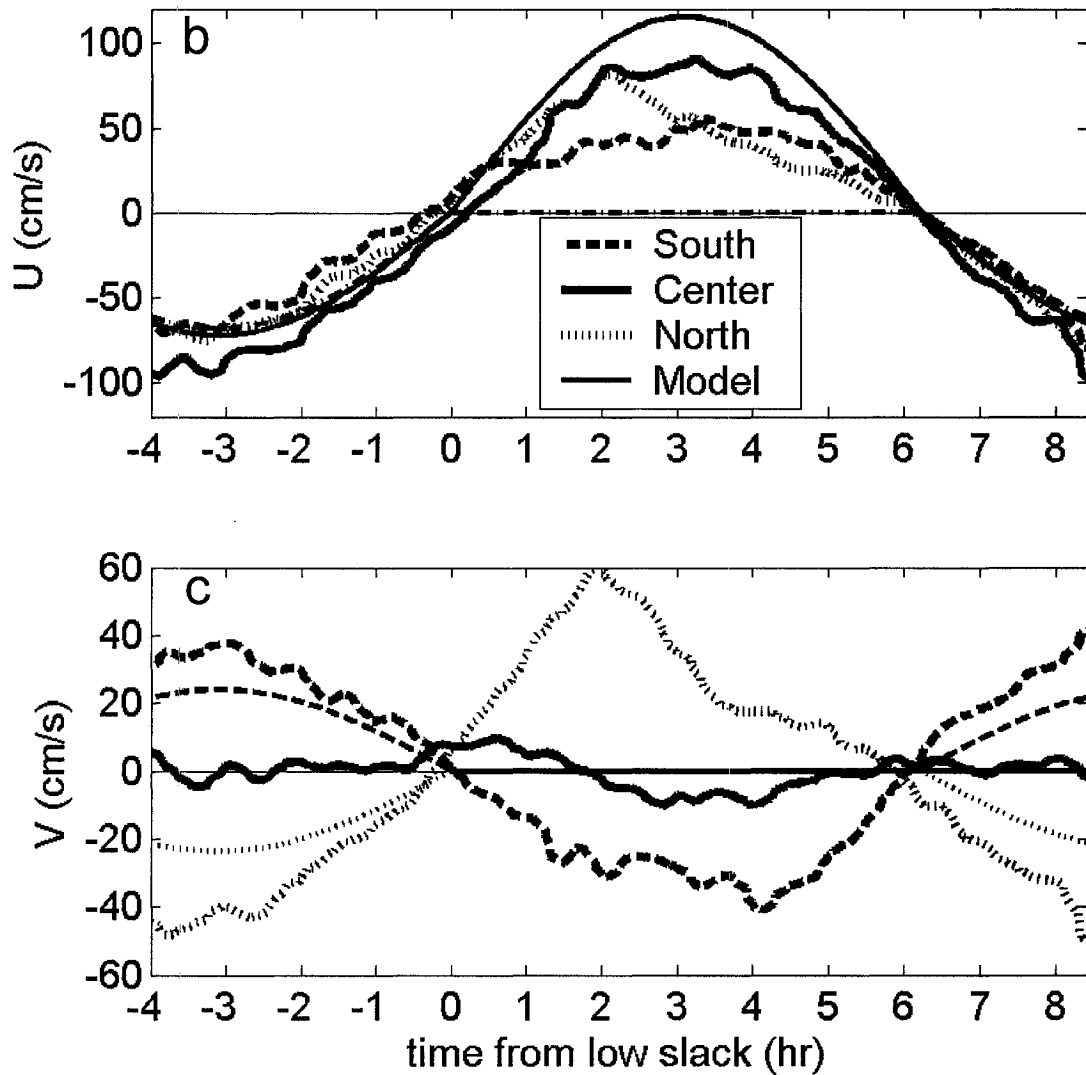


Figure 5.2 b & c: Conical Tidal Pumping Results

In 5.2b and 5.2c, the simple model of tidal pumping based on 5.2a is compared to along-channel ( $U$ ) and cross-channel ( $V$ ) velocity averages taken across summer and fall transects.

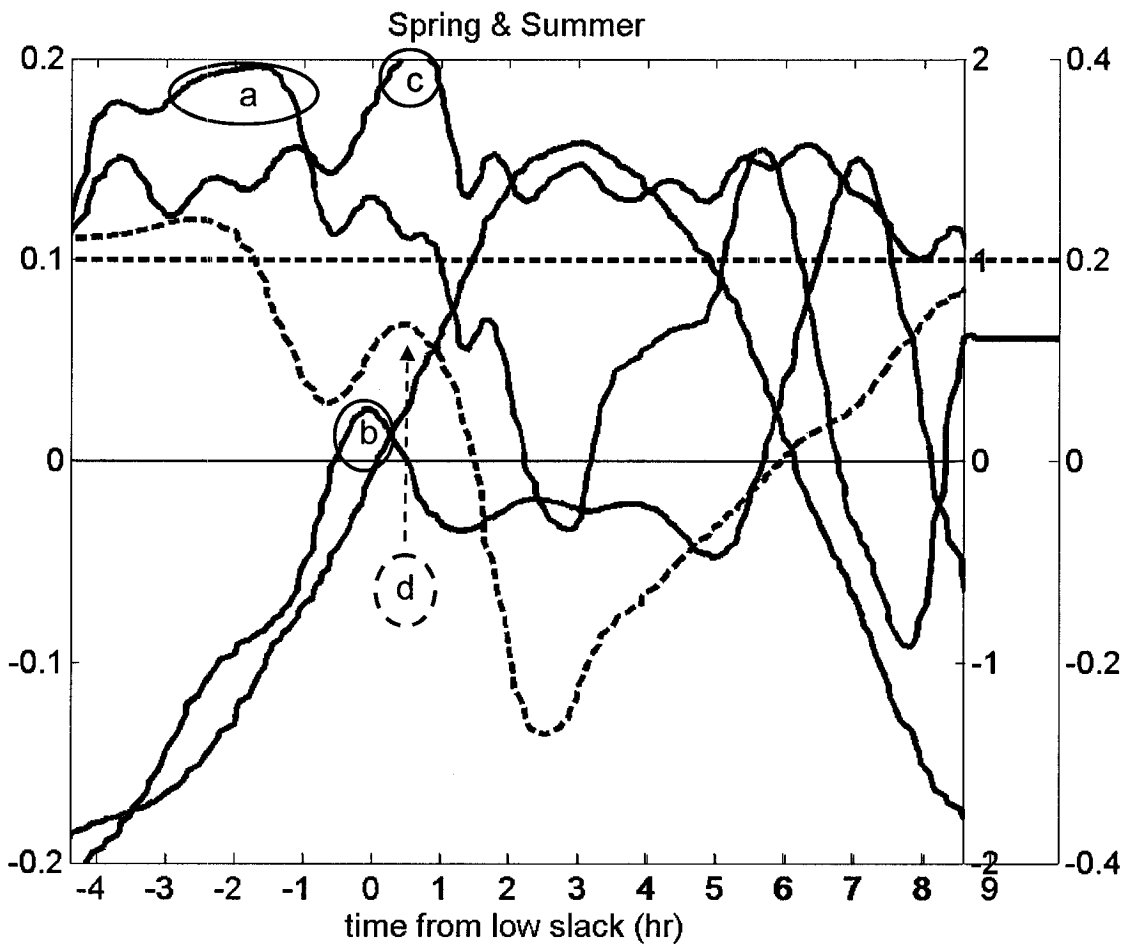
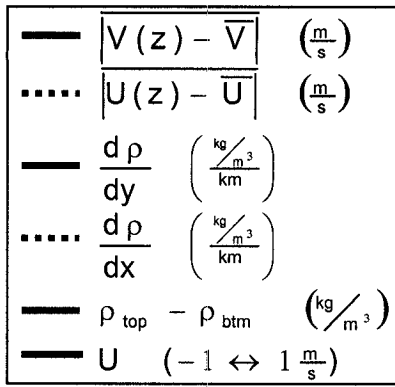


Figure 5.3: Low Slack Frictional Phasing

During wet seasons, North Bay vs. South Bay differences establish lateral density gradients (a) at end of ebb that are larger than the longitudinal gradient. Lateral density gradients drive cross-channel exchange flow at slack (b), which in turn creates stratification (c). Stratification strengthens frictional phasing at the start of flood (d).

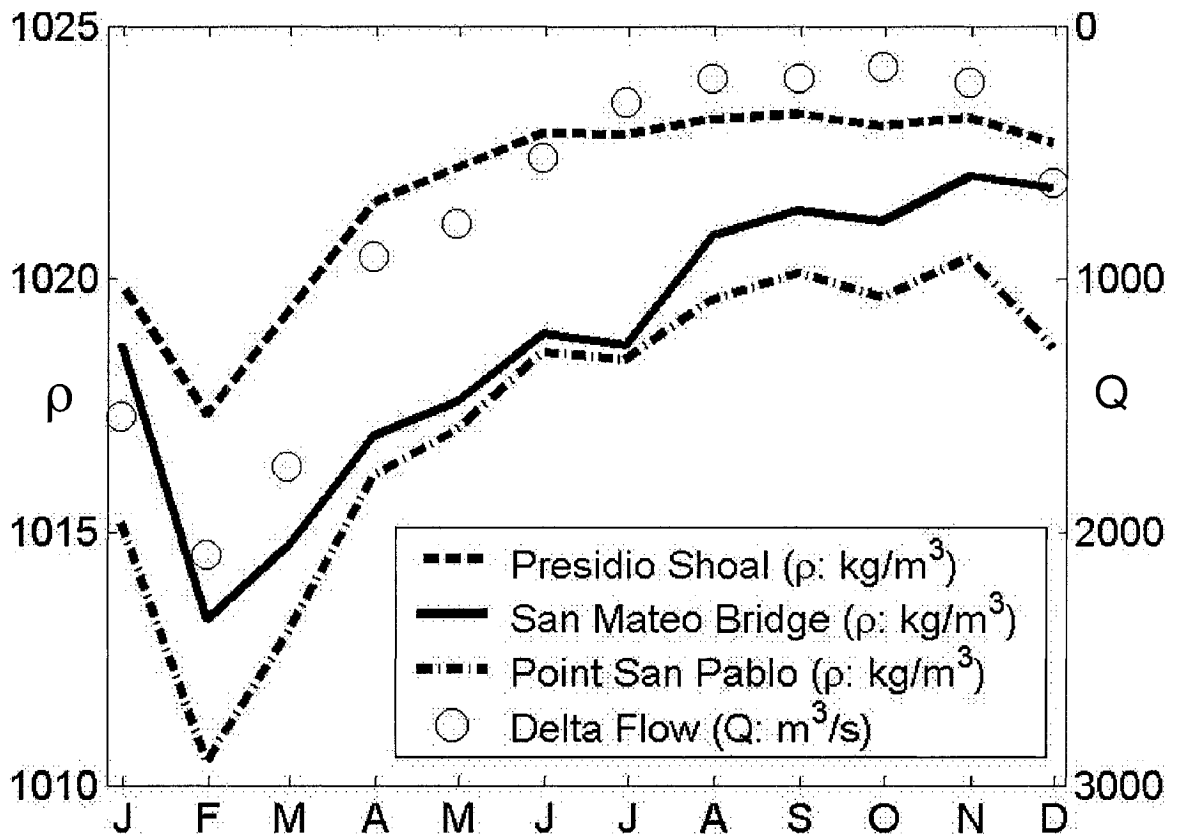


Figure 5.4: Seasonal Bay Density Response to Outflow

Density of South Bay waters at the San Mateo Bridge remain depressed through the summer, while North Bay waters at Point San Pablo respond more quickly to freshwater inflow.

## 6 Scalar Exchange

### 6.1 Introduction

Many estuaries are characterized by a bathymetric constriction at their mouth that impedes exchange with the coastal ocean. The net exchange of a scalar, such as salt, chlorophyll or suspended solids, influences conditions along the axis of the estuarine ecosystem, as well as in the adjoining coastal ecosystem. The tidally-averaged salinity field in a coastal estuary is classically described by a combination of two tidally-averaged independent processes: gravitational circulation and longitudinal diffusion [*Hansen and Rattray, 1965; Hansen and Rattray, 1966*]. MacCready [2004] updates this model by deriving more physically realistic longitudinal diffusion coefficients—particularly near the mouth. The estuary mouth is of special importance because it is generally deeper and more bathymetric variable than the rest of the estuary. Density-driven circulation increases with depth and the interaction of tidal flows with bathymetric variability causes tidal trapping and fosters other tidal diffusive processes.

MacCready notes that the challenge of characterizing exchange is more than finding the right diffusion coefficients. These tidally averaged formulations must also capture the scaling of processes with subtidal variability [*MacCready and Geyer, 1999*]. For example, to simply model the along-channel salt field in San Francisco Bay one needs a density-driven process that scales more strongly with the longitudinal density gradient than traditional gravitational circulation [*Monismith et al., 2002*].

As has been done in other large estuaries, such as the Columbia [*Kay et al.*, 1996] and the Chesapeake [*Austin*, 2002], we focus our analysis at the mouth of San Francisco Bay, which features a narrow constriction. Chapter 5 describes mechanisms that create residual flow, which include tidal pumping, steady baroclinic flow, tidal trapping of an eddy during the flood-ebb transition, and enhanced frictional phasing by the lateral density gradient on the ebb-flood transition. Scalars at the ocean-estuary interface, such as salt, are transported by these flow mechanisms. Here, we characterize the effect of each mechanism on salinity exchange under different oceanic conditions, tidal forcing, and freshwater input.

Cross-sectionally integrated salt transport can be described quantitatively using the advection-diffusion equation [*Geyer and Nepf*, 1996; *Kay et al.*, 1996], with rivers advecting salt seaward and dispersive processes carrying salt into the bay. For this chapter, we consider net exchange of a scalar to be the mass exchange rate over a fortnightly tidal cycle, although for the spring season we consider net exchange over only two days. Net exchange is then:

$$\frac{\partial \langle \bar{S} \rangle}{\partial t} = -\langle \bar{U} \rangle \frac{\partial \langle \bar{S} \rangle}{\partial x} + \frac{\partial}{\partial x} \left( K \frac{\partial \langle \bar{S} \rangle}{\partial x} \right) \quad (42)$$

where  $\langle f \rangle$  indicates a tidal average,  $\bar{f}$  indicates a cross-sectional average, the x coordinate is along the main channel, and U is the along-channel velocity. Following Fischer's [1972] seminal work, mechanisms causing dispersive flux can be identified by



decomposing flux into temporal and spatial correlations. In the following pages we describe the traditional flux mechanisms that are observed in estuaries.

### 6.1.1 Baroclinic Exchange

Longitudinal density gradients in estuaries lead to baroclinic exchange flow (equation 33). Following Monismith et al. [2002], we can summarize the velocity scale for this exchange flow as:

$$U_{BC} \approx \frac{g \frac{d\rho}{dx} H^3}{\rho_o v_t} \quad (43)$$

where  $H$  is local depth and  $v_t$  is a constant tidally-averaged vertical mixing coefficient.

This velocity structure strains the density field, converting the longitudinal salinity gradient into vertical stratification, which scales as:

$$S_{BC} \approx U_{BC} \frac{\frac{dS}{dx} H^2}{v_t} \quad (44)$$

where we have assumed a turbulent Prandtl number of one, such that  $v_t$  is the appropriate mixing coefficient for both momentum and salt.

Finally, the along-channel flux of salt due to this process scales as the product of the steady velocity and stratification scales (as in equation 14):

$$F_{BC} \approx \left( \frac{g \frac{d\rho}{dx} H^3}{\rho_o v_t} \right)^2 \frac{\frac{dS}{dx} H^2}{v_t} = \frac{(g\beta)^2 \left( \frac{dS}{dx} \right)^3 H^8}{v_t^3} \quad (45)$$

where for illustration we assume density gradients are dominated by differences in

salinity  $\left( \beta \frac{dS}{dx} = \frac{1}{\rho} \frac{d\rho}{dx} \right)$ . The baroclinically-driven flux of salt is thus a strong function of

density forcing and the local depth, and depends inversely with the strength of turbulent mixing due to tidal flows.

A similar flux is created due to periodic stratification of the water column by tidal straining [SIPS, *Simpson et al.*, 1990]. In this case, the ebb tidal flows strain the density field, again converting the longitudinal gradient into stable vertical stratification. This stratification reduces mixing and increases vertical shear. When averaged with the flood tides the residual flow and corresponding salt flux that results have the same form as the baroclinic flow [*Bowen and Geyer*, 2003; *Stacey et al.*, 2001]. In this case, however, the scaling group is less well-defined than in equation 45 due to the sensitive dependence of shear on stratification through a reduction in the vertical mixing coefficient.

### **6.1.2 Tidal Pumping and Trapping**

Tidal pumping, as defined by Stommel and Farmer [1952], is an exchange process in addition to being a residual flow mechanism. This jet-drain flow structure results in a net exchange of scalars between two embayments, which in this case are the coastal ocean and the Central Bay subembayment of San Francisco Bay (figures 1.4 and 1.5).

The actual form of this exchange, and how it will appear in a flux decomposition, depends on where the analysis is applied. In the interior of the subembayment, transects across the jet-drain structure will result in a tidally-averaged 'steady' exchange flow, with net flow into the estuary in the center (in the jet) and out of the estuary along the

perimeter (influenced by the drain). This jet-drain exchange creates lateral salinity gradients, which then result in a net salt flux.

If the analysis is applied at the actual constriction instead, the velocity structure between flood and ebb tide is symmetric, assuming that the river flow rate is much smaller than the root-mean-squared tidal flow rate. In steady state, however, the net salt flux through the constriction must be equal to the flux measured just inside the embayment. In the constriction, therefore, the phasing between velocity and salinity will be shifted, with more saline flood tides and fresher ebb tides. The fact that the velocity and salinity fields are not in quadrature results in a net flux related to the phase shift between the tidal variations of velocity and salinity. In this context, two periodic signals are in quadrature if they are 90 degrees out of phase of each other, such as  $\sin(x)$  and  $\cos(x)$ .

In the region adjacent to the mouth of an estuary, both of these tidal flux structures are likely to be evident due to partial lateral mixing of the scalar across the study location. In the region adjacent to the mouth of San Francisco Bay, both of these tidal flux structures are likely to be evident due to partial lateral mixing of the scalar across the study location. Although both processes will appear different in the flux decomposition, one as a spatial correlation and the other a temporal correlation, they arise from essentially the same mechanism: tidal flows interacting with a bathymetric constriction, and will be considered 'tidal pumping' in the discussion below.

Similarly, tidal trapping at the mouth is distinguished from tidal pumping here by the manner in which the flood jet mixes into the estuary. In trapping, the flood jet entrains estuarine water in an eddy on the landward side of a headland. If the eddy remains a coherent structure as it moves into the contraction on the ensuing ebb tide, then tidal trapping exchange may be partitioned between unsteady cross-channel flux, steady cross-channel flux, and unsteady cross-section averaged flux (defined in equation 59).

### **6.1.3 Shear Dispersion**

In addition to the fluxes created by density-driven flows and tidal flows interacting with the local bathymetry, the combination of shear (in the vertical or lateral direction) and turbulent mixing leads to a net flux that can be loosely categorized as shear dispersion [Fischer *et al.*, 1979]. The effectiveness of this mechanism depends on the extent of cross-sectional mixing that occurs within a single tidal phase; if mixing is incomplete, the shear can actually reverse the dispersion on the ensuing tidal phase [Ralston and Stacey, 2005; Zimmerman, 1986].

### **6.1.4 Exchange Process Summary**

In this presentation, tidal trapping and pumping are functions of only tidal forcing and the local bathymetry, with no influence from density forcing. Similarly, steady vertical exchange, traditionally assumed to be due to baroclinic forcing, is a function of the local depth, and does not depend on bathymetric variability in the vicinity of the measurements. In this chapter, we present observations of exchange through the mouth of San Francisco Bay, where we will find that these processes can not be completely

decoupled. Instead, density forcing is found to influence the magnitude of the net tidal fluxes, and bathymetric variations modify the vertical exchange.

## **6.2 Analysis Methods**

The goals of our analysis are to quantify tidally-averaged salt fluxes and to identify the mechanisms that govern net exchange between the ocean and estuary. In this section, we outline the spatial and temporal decomposition of the data sets which will be used to separate these mechanisms. To provide reliable temporal averages, we use harmonic analysis, also outlined in this subchapter.

### **6.2.1 Flux Decomposition**

The traditional approach to decomposing estuarine fluxes [*Fischer, 1972; Jay et al., 1997; Prandle, 1985*] emphasizes vertical structure by first averaging in the lateral dimension, preserving vertical variability. In this experiment, however, the flow is highly three-dimensional, and the lateral variability may make an equally important contribution to the net flux. The choice of averaging order becomes particularly important in non-rectangular channels that have both lateral and vertical variability in flow and scalar concentrations. We consider in this section the implications of this choice. The notation will use overbars for spatial averages, where a double overbar refers to a cross-sectional average; when a single overbar is used, there will be a superscript defining the direction of averaging (h for lateral; v for vertical). Brackets will denote temporal averages; we assume that the temporal averaging operator removes all diurnal, semi-diurnal, and tidal-monthly tidal motions.

First, the cross-sectional and temporal mean,  $\langle \bar{u} \rangle$ , is separated from the raw velocity

$(u(y, z, t))$ :

$$u_1 = u - \langle \bar{u} \rangle \quad (46)$$

Next we extract cross-section averaged velocity deviation from the mean ( $u_1$ ) and steady shear ( $u_3$ ), leaving unsteady shear fluctuations ( $u_4$ ).

$$u_2 = u_1 - \bar{u}_1 \quad (47)$$

$$u_3 = \langle u_2 \rangle \quad (48)$$

$$u_4 = u_2 - u_3 \quad (49)$$

Combining, the raw velocity is decomposed as:

$$u(y, z, t) = \langle \bar{u} \rangle + \bar{u}_1(t) + u_3(y, z) + u_4(y, z, t) \quad (50)$$

Further decomposition of  $u_3$  and  $u_4$  depends on the method of spatial averaging. Fischer, Jay, and Prandle [1972; 1997; 1985] average laterally first to find baroclinic flow and unsteady vertical shear, with the remainders becoming lateral steady and unsteady shears.

$$u_5(\mathbf{z}) = \bar{u}_3^{-h} \quad (51)$$

$$u_6(\mathbf{y}, \mathbf{z}) = u_3 - u_5 \quad (52)$$

$$u_7(\mathbf{z}, t) = \bar{u}_4^{-h} \quad (53)$$

$$u_8(\mathbf{y}, \mathbf{z}, t) = u_4 - u_7 \quad (54)$$

Rattray and Dworski [1980] and Dyer [1997] explore the possibility of averaging first vertically. Rattray discusses examples of the coordinate system dependence (e.g. Cartesian, sigma) of the two methods described above. Dyer reviews several examples where lateral exchange is comparable to or larger than vertical exchange, underscoring the importance of determining the proportion of vertical to lateral exchange. We use apostrophes to denote this alternate approach, and we refer to it as method 2.

$$u_{5'}(\mathbf{y}) = \bar{u}_3^v \quad (55)$$

$$u_{6'}(\mathbf{y}, \mathbf{z}) = u_3 - u_{5'} \quad (56)$$

$$u_{7'}(\mathbf{y}, t) = \bar{u}_4^v \quad (57)$$

$$u_{8'}(\mathbf{y}, \mathbf{z}, t) = u_4 - u_{7'} \quad (58)$$

where the primed subscripts indicate those calculated by method 2.

Multiplying flow by salinity and averaging over the cross-section and time gives the flux of salt through the channel. The processes associated with the scalar flux terms are advection from river flow (a) and dispersive flux, which includes tidal pumping (b), steady vertical exchange (c), steady lateral exchange (d), and unsteady vertical and lateral shear exchanges (e & f).

$$\begin{aligned}
\text{US} &= u_0 s_0 + \left\langle \overline{u_1 s_1} \right\rangle + \overline{u_5 s_5}^v + \overline{u_6 s_6} + \overline{\langle u_7 s_7 \rangle}^v + \overline{\langle u_8 s_8 \rangle} \quad (\text{Method 1}) \\
\text{US} &= u_0 s_0 + \left\langle \overline{u_1 s_1} \right\rangle + \overline{u_5 s_5} + \overline{u_5 s_5}^h + \overline{\langle u_8 s_8 \rangle} + \overline{\langle u_7 s_7 \rangle}^h \quad (\text{Method 2}) \\
&\quad \quad \quad \text{a} \quad \quad \quad \text{b} \quad \quad \quad \text{c} \quad \quad \quad \text{d} \quad \quad \quad \text{e} \quad \quad \quad \text{f}
\end{aligned}$$

(59)

Neither flux decomposition method directly separates dispersive flux by the residual flow creation processes, but both can be used to identify the amount of each process during each season.

The two flux decomposition methods yield different results for non-rectangular channels. In method 2, for example, if there is a lateral trend and no vertical trend to the mean data, then method 2 will not record a vertical trend (figure 6.1a). Method 1, however, will result in a vertical trend because the process of lateral averaging (equation 51) will preferentially create a vertical trend (figure 6.1b). Using artificial data sets with specified vertical or lateral trends, we illustrate this result using the steady vertical flux ratio in figure 6.2, which asymptotes to infinity as vertical shear and stratification approach zero. Overall, the ratio of steady vertical exchange from the first method to the second method increases with the ratio of lateral velocity and salinity gradients to vertical ones

$\left( \frac{\text{lateral trend}}{\text{vertical trend}} \right)$ . The signs of the linear velocity gradient and salinity gradient trends

used in the figure are the same as in the data set, with negative (seaward and fresh) at the top and north sides of the channel. The transect grid is also the same as in this data set, with deeper water on the south side of the channel. For this cross-section and trend pattern, steady vertical flux is always greater in method 1 than in method 2, steady lateral



flux is always smaller in method 1 than in method 2, and both steady lateral and vertical fluxes are always positive.

The lateral flux pattern is similar to the vertical flux pattern. The ratio of steady lateral exchange from the first method to the second method increases with the ratio of lateral velocity and salinity gradients to vertical ones (figure 6.2). Together, the sum of the vertical and lateral steady method 1 fluxes is up to 7% larger for the same lateral and vertical gradients as for method 2 (figure 6.2). We conclude that the choice of averaging method affects steady flux results in non-rectangular channels, so we will discuss fluxes calculated from both methods.

### 6.2.2 Harmonic Analysis

To extract residual exchange, we have observations from a single neap and spring day. Due to subtle tidal asymmetries, and the non-uniform sampling interval, a straight temporal average of the observations would not adequately resolve the subtidal fluxes. Instead, we rely on the integration in time of harmonics, where observed velocity and salinity signals are fit with the expected tidal frequencies. The harmonic fitting is detailed in this section.

The main velocity tidal harmonics measured at a Golden Gate current station over two years are M2 (12.42 hrs period,  $106.0 \text{ cm s}^{-1}$ ), S2 (12 hrs,  $28.9 \text{ cm s}^{-1}$ ), N2 (12.66 hrs,  $24.8 \text{ cm s}^{-1}$ ), K1 (24 hrs,  $22.2 \text{ cm s}^{-1}$ ), O1 (25.8 hrs,  $18.4 \text{ cm s}^{-1}$ ), and M4 (6.21 hrs,  $10.0 \text{ cm s}^{-1}$ ) [Walters *et al.*, 1985]. To reduce the number of parameters we chose to omit

N2 from our harmonic calculations because we found virtually the same quality of fit for our data (measured by  $R^2$ ) by removing either it or S2. Even though it is a small part of the cross-section mean signal, we keep the M4 harmonic due to the role of mixing as a function of tidal velocity magnitude. Typical  $R^2$  for velocity and salinity are 0.97 and 0.90 respectively.

Harmonics are fit to the center 2500m of the 3300m of our cross-section, on which the grid spans the cross-section arcs to follow the mean boat track. It is broken up into 17m deep by 250m wide (j,k) blocks, as described in chapter 3.  $U(j,k,t)$  as applied to this analysis is velocity perpendicular to the grid. For each block, we minimize:

$$\sum_{t=1}^N \left( U(j,k,t) - A_0(j,k) - \sum_{i=1}^5 (A_i(j,k) \sin(\omega_i(j,k)t + \theta_i(j,k))) \right)^2 \quad (60)$$

where  $A_i$  and  $\theta_i$  represent the amplitude and phase of the  $i^{\text{th}}$  tidal harmonic, which has tidal frequency  $\omega_i$  and  $A_0$  is the tidally-averaged velocity (i.e. frequency zero).

In the estimation of the unknown amplitude and phase parameters, we constrain the five amplitudes to proportions similar to published velocity and sea surface tidal harmonics [Walters *et al.*, 1985]. Spring experiment results are more sensitive to constraint choices than results from the other seasons because that data set includes only semidiurnal neap data.

To verify this harmonic approach, we fit harmonics to similarly sparse surface height measurements at the Golden Gate, and then compared the resulting surface height time

series to a full 12' minute interval data set (table 6.1). We performed identical verifications yielding similar results with salinity and temperature time series data taken by USGS at the south end of the transect path and Angel Island every 15 minutes for several months [Cuetara, pers. comm. 2004]. Harmonic fits to two days of data spaced one week apart produces similar results as harmonic fits to two continuous weeks of data. The second row of each of the two sections contains the  $R^2$  values for two weeks of data against a two week time series generated from the two day harmonic fit. Spring  $R^2$  values are lower because data were taken on consecutive days instead of days one week apart.

Tide Height	Summer	Fall	Spring
fit to 2 weeks	0.979	0.950	0.934
fit to 2 days	0.963	0.931	0.753
Salinity	Summer	Fall	Spring
fit to 2 weeks	0.915	0.825	0.738
fit to 2 days	0.881	0.778	0.621

Table 6.1:  $R^2$  Values of Harmonic Verification

### 6.3 Net Fluxes

Accurately describing the net scalar flux at a location like the Golden Gate is confounded by the fact that the instantaneous flux is two orders of magnitude larger than the net flux. In this section, we compare the advective flux out of the estuary to the dispersive flux into the estuary based on a volume integration of (equation 42):

$$\langle \text{Volume} \rangle \frac{\partial \langle \overline{S} \rangle}{\partial t} = -\langle \overline{Q} \rangle \langle \overline{S} \rangle + \text{Dispersive} \quad (61)$$

where the dispersive flux terms are all of the components described in equation 59 times area.

### 6.3.1 Advective Flux

Advective flux is the mean flow times the difference in mean salinity at the upper and lower ends of the estuary. Mean salinity at the upper end is near zero, 20-34 PSU less than at the Golden Gate. Our mean salinity from harmonics is within 0.1 PSU or 0.3% of the data mean for each season. Mean flow from our data is known to a much lower percent accuracy because it is only ~1% of the RMS instantaneous flow ( $\sim 60,000 \text{ m}^3 \text{ s}^{-1}$ ). Furthermore, there is a net seaward flow out the side of our transect path, so the harmonic results systematically underpredict net advective flux. Instead of using harmonics, we estimate mean flow from a mass balance from river and tide gauges.

The main flow contribution comes from the Delta [DWR, 2004]. 10% of the annual freshwater flow derives from rivers and streams downstream of the Delta, although their contribution occurs mainly within weeks of winter storms. Some of these streams are gauged continuously, but most are not. Flows of streams not gauged during our experiment are estimated by comparing their hydrographs during the times they were gauged to those of the adjacent continuously gauged streams. Streams downstream of the Delta contributed less than 2% of the inflow during each of our field campaigns. We make a similar estimation of local municipal wastewater outflow, which acts as a

freshwater source, based on outflows from East Bay Municipal Utility District, Santa Clara County MUD, and San Francisco MUD. Local municipal utility district (MUD) outflow was  $\sim 10 \text{ m}^3 \text{ s}^{-1}$ , 9% of the fall experiment flow, and less than 3% of spring and summer experiment flows. The volume of the bay varies during each 30-hour study due to meteorological effects (e.g. storm surges) and fortnightly or longer tidal changes. Bay volume change and its resulting effect on mean flow out of the bay is found from a low-pass filter on the bay's five tide gauge signals (Golden Gate, Alameda, Redwood City, Chevron Pier, and Port Chicago). Volume change is the surface area times the elevation change, a large contribution in the spring experiment (23%), but not in the fall or summer experiments (<2%). Evaporation is a big portion of advective flux (20%) only during the fall experiment [Conomos, 1979]. Summing these sources gives the advective flux to within a few percent (table 6.2). Advective flux is:

$$\langle \overline{Q} \rangle = Q_{\text{Delta}} + Q_{\text{Local Rivers}} + Q_{\text{MUD}} - \text{Area} \cdot \left( \frac{d(\text{Elev.})}{dt} + \text{Evap. rate} \right) \quad (62)$$

where each Q term represents a freshwater source, and the last two terms account for bay volume loss.

	Spring '02	Summer '03	Fall '02
Advective (DWR)	-18.5	-12.2	-4.4
Dispersive (Method 1)	28.2	23.0	3.5
Dispersive (Method 2)	28.8	23.2	3.5
Average % Difference	40%	46%	27%
dS/dt (data, Salinity per day)	0.21	0.14	-0.005
dS/dt (box model)	0.17	0.19	-0.002

Table 6.2: Advective vs. Dispersive Fluxes

Scalar fluxes are measured in thousand  $\text{PSU m}^3 \text{ s}^{-1}$ . Salinity is the ratio of conductivity to the conductivity of a standard concentration of potassium chloride at a standard temperature and pressure. Salinity is expressed as a unitless quantity on the Practical Salinity Unit (PSU) scale. For estuaries, salinity is close to a measure of concentration (mass per volume). A concentration times a flow ( $\text{m}^3 \text{ s}^{-1}$ ) has units of mass flux ( $\text{kg s}^{-1}$ ).

### **6.3.2 Advective vs. Total Dispersive Flux**

We compare the advective and dispersive fluxes for both averaging methods during each season. All of the dispersive flux totals for each season and method are within 50% of corresponding advective fluxes, indicating our dispersive flux values are of the right order (table 6.2). Dispersive flux totals include cross-section averaged unsteady correlations and steady lateral and vertical correlations (equation 59 b, c, and d). Dispersive flux totals from the two averaging methods are within two percent of each other for each season. The signs of the net salt fluxes are also correct because they are into the bay during experiments when river flow decreased (spring and summer), and out of the bay for the fall experiment, when river flow increased slightly (by  $35 \text{ m}^3 \text{ s}^{-1}$ ).

Net flux values are checked quantitatively with a simple box model (equation 61). Net salt flux is equal to the change in salinity of Central Bay in time. Only Central Bay water is exchanged at the Golden Gate during any 25-hour time period, so our box considers Central Bay salinity. We consider the salinity variability of Central Bay based on local observations. Salinity has been measured continuously every 15 minutes at four points in

Central Bay for the last several years by USGS [Cuetara, pers. comm. 2004, and

sfbay.wr.usgs.gov 2005].  $\frac{\partial \langle \bar{S} \rangle}{\partial t}$  is the trend of the diurnally-filtered mean of the three

signals.  $\frac{\partial \langle \bar{S} \rangle}{\partial t}$  from the box model is within 30% for the spring and summer experiments

(table 6.2). Smaller salinity changes and instrument fouling make  $\frac{\partial \langle \bar{S} \rangle}{\partial t}$  uncertainty 50%

for the fall experiment, while it is 5% during the wet seasons. Nonetheless, calculated net salt fluxes match the rise of Central Bay salinity well, considering the short data set length and the dynamically complex field site.

## 6.4 Dispersion Processes

As described in the introduction, we can associate physical processes to one or more of the terms in the flux decomposition (equation 59). In this section, we quantify each mechanism separately by integrating the harmonics associated with the various spatial structures.

### 6.4.1 Tidal Pumping

Tidal pumping as observed at a contraction is calculated from the temporal correlation of cross-section mean salinity and velocity. The net flux created by this mechanism is from subtle shifts in the phasing of velocity and salinity.

To be specific, we describe the cross-sectional average of salinity in terms of harmonics as:

$$\bar{S}(t) = \sum_{i=1}^5 A_i^{\bar{S}} \sin(\omega_i t + \theta_i^{\bar{S}}) \quad (63)$$

and of velocity as:

$$\bar{U}(t) = \sum_{i=1}^5 A_i^{\bar{U}} \sin(\omega_i t + \theta_i^{\bar{U}}) \quad (64)$$

where the summation is over the 5 tidal harmonics described above (with frequencies  $\omega_i$ ).

Here  $A_i^{\bar{S}}$  and  $A_i^{\bar{U}}$  represent the amplitudes of the tidal variability (for harmonic  $i$ ) of the cross-sectionally averaged salinity and velocity, respectively. Finally,  $\theta_i^{\bar{S}}$  and  $\theta_i^{\bar{U}}$  represent the phase associated with each harmonic component. Integrating these harmonics over time gives the net tidal pumping flux, where it is seen that net flux is defined by the relative phase of salinity and velocity:

$$\begin{aligned} & \sum_{i=1}^5 \frac{\text{Area} \cdot \int_0^{2\pi/\omega_i} A_i^{\bar{U}} \sin(\omega_i t + \theta_i^{\bar{U}}) A_i^{\bar{S}} \sin(\omega_i t + \theta_i^{\bar{S}}) dt}{2\pi/\omega_i} \\ & = \text{Area} \cdot \frac{1}{2} \sum_{i=1}^5 \cos(\theta_i^{\bar{U}} - \theta_i^{\bar{S}}) A_i^{\bar{U}} A_i^{\bar{S}} \end{aligned} \quad (65)$$

As shown in table 6.3, and as predicted by Walters et al. [1985], tidal pumping salt flux is the largest contributor to dispersive flux during all three seasons.



	Spring '02		
	Method 1	Method 2	+/-
Pumping	21.2	21.2	11%
Steady Vertical	4.7	4.2	11%
Steady Lateral	2.3	3.5	13%
Total	28.2	28.8	8%
	Summer '03		
	Method 1	Method 2	+/-
Pumping	18.9	18.9	11%
Steady Vertical	2.1	1.5	19%
Steady Lateral	2.0	2.8	27%
Total	23.0	23.2	9%
	Fall '02		
	Method 1	Method 2	+/-
Pumping	2.8	2.8	19%
Steady Vertical	0.3	0.2	30%
Steady Lateral	0.4	0.5	48%
Total	3.5	3.5	17%
Scalar fluxes are in thousands of PSU*m <sup>3</sup> /s			

Table 6.3: Dispersive Flux Decomposition

This flux, however, scales more strongly with freshwater flow than standard tidal pumping theory. In Stommel and Farmer's classic geometric explanation of jet-drain tidal pumping [1952], tidal pumping flux scales linearly with the along-channel salinity

gradient  $\left( \text{Flux} = K \frac{d\bar{S}}{dx} \right)$ . Tidal pumping increases with tidal excursion, and thus with

root mean squared (RMS) velocity, by a proportion dependent on a channel's geometry (figure 1.4). Tidal pumping flux during the spring experiment is greater than during summer, consistent with the spring experiment having a higher RMS velocity at a nearly identical salinity gradient. Spring experiment RMS velocity is higher than in summer and fall because of instrument limitations, so our detailed look at the effect of changing freshwater flow on tidal pumping will be between just the summer and fall experiments.

Summer experiment tidal pumping flux is 6.8 times fall's despite only a 3.5 times larger

$$\frac{\overline{dS}}{dx} \text{ (table 3.1 and 6.2), where } \frac{\overline{dS}}{dx} \text{ is change in salinity over tidal excursion } \left( \frac{\Delta \overline{S}}{\overline{U} \Delta t} \right).$$

Since the summer and fall experiment velocities are the same in magnitude, the tidal pumping discrepancy implies a change in the relative phase of mean salinity and velocity signals from fall to summer. We will first show how tidal pumping depends on the timing of the salinity and velocity signals, and then discuss two sources for a seasonal change in this timing.

We emphasize the velocity to salinity phase relationship by writing tidal pumping flux as a function of one tidal harmonic.

$$\frac{1}{2} \sum_{i=1}^5 \cos(\theta_i^q - \theta_i^s) A_i^q A_i^s \cong \frac{1}{2} A_i^q A_i^s \cos\left(\frac{\pi}{2} - \phi\right) \quad (66)$$

where  $\phi$  refers to a shift in the phase of salinity away from quadrature. To tidally pump salinity into the bay, salinity must follow velocity by less than 90 degrees. If salinity and velocity are in quadrature, tidal pumping flux will be zero, as the salinity field is simply advected back-and-forth by the tidal velocities. To find this mean salinity to velocity phase lag, we use the harmonics generated from fits to all of each season's mean salinity and velocity data. From a long time series recreated from the five component harmonics, we define the time lag as the time from zero crossings of  $\frac{\overline{dS}(t)}{dt}$  to zero crossings of  $\overline{U}(t)$ .

Fall and summer experiment lags are 15 and 29 minutes, which correspond to 4.5 and 9 degree phase lags in a system with only M2 tides. Doubling the phase lag between

seasons nearly doubles tidal pumping flux, so the phase lag change is a large portion of the total dispersive flux.

The effect of seasonal phase change on tidal pumping flux is larger than the calculated uncertainty (table 6.3). Uncertainty of the tidal pumping flux is estimated as the standard deviation of the difference between measured and harmonic cross-section mean tidal flux.

$$\sigma_{TP} = \text{Area} \cdot \text{std} \left( \sum_{t=1}^N \left( \overline{U}(t) - \langle \overline{U} \rangle \right) \left( \overline{S}(t) - \langle \overline{S} \rangle \right) - \sum_{i=1}^5 A_i^{\overline{U}} \sin(\omega_i t + \theta_i^{\overline{U}}) A_i^{\overline{S}} \sin(\omega_i t + \theta_i^{\overline{S}}) \right) \quad (67)$$

A portion of the calculated tidal pumping phase lag originates from the harmonic analysis, which integrates over short duration recurring features. For example, there is a reversal of the lateral salinity gradient at the beginning of every ebb tide (hours -1 to 3 in figure 6.3) caused by a tidally trapped eddy entering the channel from the north side [Chapter 5]. The dip and rise of salinity of north side salinity from the eddy adds a small phase shift to the harmonic fits, distributing the effect of the eddy across the entire tidal cycle. Integrating over this small feature adds to the tidal pumping flux (equation 59b) while reducing the unsteady lateral shear flux (equation 59f). Thus tidal pumping flux includes two residual processes, traditional tidal pumping and tidal trapping of an eddy.

To isolate the source of the seasonal phase lag change, we first examine how the phasing between salinity and velocity varies across the channel. The phase lag between  $S(t)$  and  $U(t)$ , as well as the root-mean-square values of  $U$ , and  $S$  are shown for six parts of the transect path: the top and bottom of the south, center, and north sections (figure 6.4). The largest contribution to tidal pumping is from the upper center of the channel, mostly

because of the large lag there, but also because of a higher velocity range. In classic flood jet-ebb drain flow, as well as in this data set, ebb begins at the channel sides. Water entering from the sides is fresher than the flood jet, thus the lowering of cross-section mean salinity precedes high slack tide, creating the aforementioned lag. Radial flow also moves fresher water into the channel's center. The center of the channel has higher salinity than the sides at the end of flood because of its larger tidal range (deeper water, less side and bottom friction). The center also turns from flood to ebb later than the sides, so the salinity signal precedes the velocity signal by more in the center than the sides, increasing the  $S(t)$  to  $U(t)$  lag. A similar argument can be made for jet-drain pumping creating more  $S(t)$  to  $U(t)$  lag in the center at low slack. Seasonally, phase lag is higher on the bottom and north of the channel during the summer experiment than during fall. It will be shown that lag increases during wet seasons on the north half of the channel at high slack and on the bottom half of the channel at low slack.

#### **6.4.1.1 Flood-Ebb Tidally Trapped Eddy**

To analyze subtidal lags related to tidal pumping, we look directly at time series data instead of at harmonic reconstructions. Seasonal tidal pumping phase change derives from a salinity signal change, not a velocity signal change. Mean slack tide averages 1¼ hours after high and low tides during wet and dry season experiments (77 and 79 minutes in summer, 75 and 79 minutes in fall). This lag produces a flux into the bay from tidal Stokes Drift that is nearly as large as the total dispersive flux. Tidal Stokes Drift, which is the channel width times the temporal correlation of tide and velocity, is included in the advective flux (equation 59).

A tidally trapped eddy forms during the second half of flood tide between Point Cavallo, Angel Island, and Tiburon (figure 1.6). Its seaward side has lower salinity than the adjacent flood jet waters. As the tide decelerates, the eddy moves out into the channel near the end of flood tide. By entering the channel before the end of flood, the eddy starts a decrease in mean salinity before ebbing of mean velocity starts (figure 6.3 at time = - 1 hr.). Fresher surface water from the seaward side of the eddy crosses the transect path at the same time as cross-channel vertical shear starts increasing. Cross-channel vertical shear is indicative of the Point Cavallo eddy moving north to south in the top half of the water column. We specify the time at which the eddy enters the channel as when the northernmost 500m of the transect path goes from northward to southward velocity across the channel. This time minus the time of mean high slack is the lag. Summer has a 16 minute longer lag than fall.

The landward (upstream) side of the tidally trapped eddy has a sharper transition, so it is apparent in several signals, such as the vertical shear and the lateral salinity gradient. Transitions in each of these data sets indicate the landward side of the Point Cavallo eddies that move through the transect path in the fall experiment lag on average 16-19 minutes behind the eddies from the summer experiment. The lags are averages of the lags for the 3 to 5 occurrences during each season. As we will quantify in section 6.4.1.2, a large portion of the summer experiment tidal pumping phase lag, and thus a large portion of net exchange, is contributed by the seasonal phase lag shift of both sides of the eddy.

The seasonal phase lag shift between tidal velocity and salinity is due to the complex interaction of bathymetry and density forcing. The eddy is strongest near the surface of the transect path because it sets up in shallow water. It is advected by baroclinic flows when it moves into the deep channel bordering its south and east sides. The seaward side of the eddy is less dense than channel water as it draws mainly from fresher water northeast of the flood jet. The landward side of the eddy draws saline water from the jet, creating a density front. Correspondingly, stratification peaks on the north side as the first half of the eddy crosses the transect path, and drops as the salty back half crosses (hours 0 to 2 in figure 6.3c). Both the seaward and landward sides of the eddy advect seaward by baroclinic exchange.

A scaling of the seasonal change in barotropic acceleration shows that this mechanism is sufficient for causing the phase lag increase. Cross-channel acceleration of the eddy by the gravitational circulation is slowed by friction.

$$\frac{\partial V}{\partial t} = -\frac{gH}{\rho_o} \frac{\partial \rho}{\partial y} - \frac{C_d}{H} V^2 = \frac{10 \frac{m}{s^2} \cdot 55m \cdot 0.15 \frac{kg}{m^3}}{10^3 \frac{kg}{m^3} \cdot 1000m} - \frac{0.0025}{55m} (45 \frac{m}{s})^2 = 7.3 \cdot 10^{-5} \frac{m}{s^2}$$

(68)

Assuming acceleration is constant and the eddy edges are accelerated for an hour, they will move seaward into the channel 475m ahead of where they would be in the dry season.

$$d = \frac{1}{2} \frac{dV}{dt} t^2 = \frac{1}{2} 7.3 \cdot 10^{-5} \frac{m}{s^2} \cdot 3600^2 s^2 = 475m$$

(69)

This puts the eddy 18 minutes ahead in the tidal cycle.

$$\Delta\text{lag} = \frac{d}{U_{\text{tidal}}} = \frac{475\text{m}}{.45\frac{\text{m}}{\text{s}}} = 18\text{min} \quad (70)$$

In this analysis, friction has been neglected, as it is an order of magnitude smaller than the baroclinic forcing. In summary, density forcing moves a tidally trapped eddy 15-20 minutes ahead in the tidal cycle. This eddy is a major feature in exchange for more than three hours of every M2 tidal cycle.

#### 6.4.1.2 Ebb-Flood Frictional Phasing

Tidal pumping is stronger during wet seasons also because of increased frictional phasing around low slack tide. Mean salinity starts increasing 43 minutes earlier in the tidal cycle during wet seasons (hours 5 to 7 figure 6.3c). Data in figure 6.3 are aligned to high and low slacks, and data in between slacks are scaled to a 6.21 hour (M2) interval, so that short and long semi-diurnal tides can be compared.

Again, mean velocity phasing does not vary seasonally; however, near-bed velocities reverse 15-20 minutes earlier in the summer than in the fall experiment.  $\frac{dU}{dz}$  and  $\frac{dV}{dz}$  also flood 15-20 minutes earlier and with higher magnitudes during wet seasons. As described in chapter 5, the strong lateral density gradient during the wet season drives a lateral exchange flow  $\frac{dV}{dz}$ , which increases stratification. Thus, stratification at low slack is proportionally higher in the wet season by more than the along-channel density

gradient.  $\left(\frac{d\langle\bar{S}\rangle}{dz}\right)$  is 3.5 times larger in the wet than in the dry season, while  $\left(\frac{d\langle\bar{\rho}\rangle}{dz}\right)$  is 4.7

times larger overall and 6.8 times larger just after low slack.) This additional stratification strengthens along-channel shear and increases the vertical frictional phasing at low slack during wet seasons. As a result, most of the seasonal phase lag change in salinity is in the bottom half of the water column.

### 6.4.1.3 Tidal Exchange Ratio

Tidal Exchange Ratio (TER) is an aggregate measure of tidal exchange applied to estuary mouths where tidal pumping is the main exchange mechanism. TER through the Golden Gate has been estimated by Largier [1996] and found experimentally by Parker [1972]. Parker's experiment was done in early fall to maximize the proportion of tidal pumping to baroclinic exchange. Both estimates are a few times higher than our findings (table 6.4 and figure 6.5), which can be explained by relating TER to tidal pumping flux.

	Tidal Range (m)	Maximum Salinity	Minimum Salinity	Flood Salinity	Ebb Salinity	Ocean Salinity	TER
Fall FOGG (24hr*2)	2.45	32.6	31.5	32.21	32.15	34.3 +/- .5	0.03
Summer FOGG (24hr*2)	1.97	32.1	28.3	30.76	30.33	34.3 +/- .5	0.11
Spring FOGG (12hr*2)	1.63	31.8	28.6	30.52	30.14	34.3 +/- .5	0.09
Parker Fall Pt. Bonita Neap (12 hr)	1.10	33.8	32.8	33.34	33.09	34.53	0.17
Parker Fall Pt. Bonita Spring (12hr)	1.75	33.9	32.0	33.26	32.63	34.59	0.32

Table 6.4: Tidal Exchange Ratios

FOGG, which stands for Flux Observations at the Golden Gate, refers to the data from this experiment.



The tidal exchange ratio is the ratio of a flood and ebb scalar concentration difference and an oceanic and ebb concentration difference (equation 3). We use salinity as the tracer for calculating our flood and ebb concentration averages (table 6.4). For offshore salinities, we use typical depth-averaged values for non-El Niño years [Collins *et al.*, 2002; Parker *et al.*, 1972]. Parker calculated TER from repeated vertical profiles at four stations across ocean side of the Golden Gate Channel (Point Bonita) as well as oceanic salinity values from a concurrent survey of the Gulf of the Farallones. The 2002 fall experiment's tidal salinity range is similar to Parker's, yet our difference between mean ebb and flood salinities is much less. Parker's experiment, which pre-dates ADCPs, understandably did not accurately measure when the tide turned. By assuming a large  $\frac{d\bar{S}(t)}{dt}$  to  $\bar{U}(t)$  lag, TER was over-estimated at Point Bonita, which Largier calculates should have a TER roughly double that of the TER at the Golden Gate Bridge. Parker's TER result implies a tidal pumping flux 5-9 times tidal pumping flux from our fall experiment, however, advective flux was only twice our fall experiment's advective flux. As shown in section 4, tidal pumping flux is roughly proportional to advective flux for low to moderate flows. While not previously described as such, Parker's data set shows evidence of an ebb-flood tidally-trapped eddy, which would further complicate interpretation of the salinity to velocity lag, and thus reinforce our interpretation that tidal pumping and trapping often co-occur. Particularly on the stronger of the two measured tides, salinity across the channel dips about 2.5 hours after the salinity minimum, indicating that a mass of previously ejected water reenters the channel.

Largier [1996] suggests larger TERs than Parker's by attributing tidal exchange to ebb jet-flood drain geometric exchange (figure 1.4). In this model, the jet does not spread laterally or entrain water through its sides. Despite its hourglass surface appearance, jet-drain exchange is not as large as suggested by this idealization because the channel cross-sectional area contracts only by a factor of 2 at the Golden Gate (figure 6.6). Similarly, the ocean side of the channel is much deeper than the horseshoe-shaped ebb bar, which bounds half the volume of the tidal prism. The jet spreads laterally after going through both of these contractions because the channel shallows. Lateral spreading of the jet reduces jet-drain geometric exchange.

Hydrodynamics may have had a role in shaping the channel so that its cross-sectional area has become relatively constant. While the bed surface of the Golden Gate Channel deepens dramatically at the Golden Gate Bridge contraction, the depth to bedrock is relatively constant throughout the channel at 80-100m below MSL [*Carlson and McCulloch, 1970; Chin et al., 2004*]. Along the shoals there is up to 80m of sediment overlaying the bedrock. The channel bottom surface is bedrock at the Golden Gate Bridge contraction. As the channel widens on either side, there is less exposed bedrock, thicker sediment deposits, and finer surface sediments [*Carlson and McCulloch, 1970*]. At cross-sectional area minima there are higher tidal velocities and thus higher shear stresses, which in turn scour away sediment. Channel morphology is influenced by this cross-sectional area constraint only when sea level is high enough to intrude through the channel. The Golden Gate Channel has carried a shallow non-tidal river during low sea level stands (glacial maximums), and has been a tidal inlet only during the last few

interglacial periods. A geologically young feature, San Francisco Bay was created over the last 1-2 million years by tectonic lowering [Atwater *et al.*, 1999].

#### **6.4.2 Steady Fluxes**

Steady vertical and lateral fluxes comprise 18-26% of the total flux for each season (table 6.3). Steady vertical fluxes are 10 times larger in the summer than in the fall, and our estimates of spring steady vertical fluxes are another factor of 2 larger than the summer. We note, however, that the spring values are biased by sampling primarily during energetic tidal phases. The lateral steady fluxes show a similar, but weaker seasonal variation, with summer values exceeding fall values by a factor of about 5.

Choice of averaging method provides larger differences between steady fluxes within seasons than uncertainty for the steady dispersive fluxes. Steady terms differ by up to 40% depending on averaging method (table 6.3), as predicted in the discussion of figure 6.2. The steady flux ratios calculated from the data are in close agreement with the theoretical values presented in figure 6.2 for both vertical and lateral components. The vertical steady flux ratios during each season are near to and have the same trend as the vertical steady flux ratio calculated for a wide range of linear lateral and vertical salinity and velocity gradients. Similarly, the lateral steady flux ratios for each season map to the lateral steady flux ratios calculated for a wide range of linear lateral and vertical salinity and velocity gradients. The data do not match the theoretical values exactly because actual steady shear and salinity gradient trends are not linear, and because of experimental error.

We estimate the effects of experimental error on the flux components by their sensitivity to changes in harmonic constraints, to changes in the number of harmonic parameters, and from a Monte Carlo simulation based on the variances of the residuals between the velocity and salinity data and the harmonic fits. Uncertainty values from sensitivity and Monte Carlo analyses are less than or equal to those in table 6.3, which are calculated by propagating uncertainty of the same residuals [Taylor, 1997]. For steady vertical flux:

$$\sigma_{\text{steady vertical}}^2 = \sum_{v=1}^N \text{Area}_v \sqrt{\sigma_{R_{sv}}^2 (\bar{U}_v^h - \bar{U})^2 + \sigma_{R_{uv}}^2 (\bar{S}_v^h - \bar{S})^2} \quad (71)$$

$v$  indexes 17m vertical blocks.  $\sigma_{R_{sv}}^2$  is the variance of the residual of horizontally averaged salinity at a vertical bin  $v$ . Uncertainty from pumping is smaller because spatial averaging over a larger area reduces noise, and because the mean tidal velocity and salinity signals are stronger than the residual flow signals. The sum of the steady fluxes for method 1 are 1-2% higher than for method 2, opposite of the trend predicted in figure 6.2 (dotted line), although within the uncertainty bounds.

Uncertainties are small enough for us to glean some physical results from the steady fluxes. The proportion of steady vertical exchange to steady lateral exchange increases with outflow as it should because freshwater outflow increases baroclinic exchange more than it increases tidal pumping exchange. Tidal pumping creates steady lateral exchange from net seaward flow of fresher water through the transect sides and net landward flow of saline water through the transect center. In terms of total steady flux to unsteady (tidal pumping) flux, summer and fall proportions of tidal pumping flux are indistinguishable

within uncertainty, while spring has proportionally more steady shear. Spring and summer experiment density forcing is the same, so one might expect them to have the same proportion of tidal pumping flux. However, higher spring experiment velocities increase steady shear as discussed in section 5.3.

### 6.4.3 Unsteady Shear Flux

Unsteady lateral and vertical shear fluxes are not displayed because the high frequency variability causing these fluxes is not well resolved by the harmonic analysis. These fluxes change by up to an order of magnitude under sensitivity analysis, and at their high end are similar in magnitude to the steady lateral and vertical fluxes. While we can not suggest specific values, there appears to be a positive unsteady lateral shear flux and no significant unsteady vertical shear flux. Lateral unsteady flux would be created from salinity to velocity phase lags that vary in time as tidally trapped eddies move to the center of the transect path. Asymmetries in sill-induced shear and frictional phasing would create vertical unsteady shear flux.

## 6.5 Dispersion Coefficients

Seasonal scaling of the flux mechanisms can be estimated with bulk along-channel dispersion coefficients, which are calculated from:

$$\text{Flux} = K_x \frac{d\overline{S}}{dx} \quad (72)$$

During the fall and summer experiments, the dispersion coefficients are  $380 \text{ m}^2 \text{ s}^{-1}$  and  $720 \text{ m}^2 \text{ s}^{-1}$ , respectively (figure 6.7). We put our  $K_x$  values in context by comparing them to earlier estimates and to standard scalings of  $K_x$ . Monismith [2002] calculated the bulk

dispersion coefficient ( $K_x(x, Q)$ ) along the axis of the San Francisco estuary over a range of Delta inflow rates from 30 year data sets of monthly along-axis salinity [USGS, 2004] and daily freshwater flow [DWR, 2004].  $K_x$  from the Monismith model at our transect path is within 33% of this experiment's values for the same seasonal freshwater flow rates (figure 6.7).

Monismith [2002] described  $K_x(x)$  as a function of several exchange mechanisms: gravitational circulation, bathymetrically induced exchange (e.g. tidal pumping), and strain induced periodic stratification (SIPS). To separate  $K_x$  by mechanism at any cross-section along the estuary, we focus on dependence of  $K_x$  on the along-channel salinity gradient.

$$\text{Flux} = \left( \sum_i k_i \left( \frac{d\bar{S}}{dx} \right)^{n_i} \right) \frac{d\bar{S}}{dx} \quad K_x = k \left( \frac{d\bar{S}}{dx} \right)^n \quad (73)$$

where  $n$  is 0 for purely tidal processes, such as standard tidal pumping and trapping.  $n$  will be positive for those processes that are a function of density forcing. For example,  $n$  is 2 for classical baroclinic circulation (from equation 45). Monismith et al. [2002] found that salt flux along the estuary scales more strongly with flow than could be achieved by either purely tidal or classical baroclinic circulation mechanisms. In other words,  $n$  averaged over the entire estuary is greater than 2. While the result for the entire estuary that  $\bar{n}(x)$  is greater than 2 is valid, at the Golden Gate we find a weaker dependency of

$K_x$  on  $\frac{d\bar{S}}{dx}$ .

From the model's  $K_x(x, Q)$ , we solve for  $n$  in our range of flows ( $100\text{-}1000 \text{ m}^3 \text{ s}^{-1}$ ) 1.5km from the Golden Gate.  $n$  is 6.2 in this model, which is considerably more than the  $n$  of 0.51 found from combining our fall and summer data. Model results for  $K_x$  are consistent with our data, so it is divergent  $\frac{d\bar{S}}{dx}$  values that cause the disagreement in dispersion scaling (figure 6.7). By fixing Golden Gate Bridge salinity at 32, the model overestimates  $\frac{d\bar{S}}{dx}$ . As shown in this experiment, mean salinity 1.5km from the Golden Gate drops significantly (by 2) even under moderate flows ( $406 \text{ m}^3 \text{ s}^{-1}$ ). Thus the Golden Gate Bridge is not strictly the downstream boundary of the salinity field. Moving the ocean salinity boundary condition of the model seaward would allow it to exhibit higher  $\frac{d\bar{S}}{dx}$  near the bridge. However, placing the zero point at the bridge zero point is understandable because the model is focused on describing upstream conditions, such as the location of X2. Also, the data available for use by the model [USGS, 2004] do not include samples taken west of the bridge, and the data in the 5km east of the bridge are sparse.

We now examine how each flux mechanism contributes to our scaling of the bulk dispersion coefficient. As described in section 6.1, tidal pumping increases with flow more than a purely tidal process because of density-driven effects. Thus,  $n$  for tidal pumping is greater than 0 ( $n=0.54$ ).  $n$  for steady lateral exchange is also greater than 0 (0.32), but for a different reason.  $\frac{d\bar{S}}{dy}$  increases proportionally more than  $\frac{d\bar{S}}{dx}$  between

our fall and summer data sets because of a North Bay to South Bay salinity gradient created by South Bay's longer salinity recovery time after spring runoff [section 5.4]. The steady lateral velocity gradient is essentially the same across seasons, so the rise from dry to wet seasons in the steady lateral dispersion coefficient comes entirely from a rise in lateral salinity gradients.

In the vertical direction,  $n$  for steady shear flux ( $n=0.50$ ) is much less than  $n$  from standard baroclinic scaling ( $n=2$ ) because most of the net vertical shear and stratification derive from asymmetric flow over a sill, which is forced more by tides than by density gradients [section 5.3.4].

Density forcing plays a role in generating the tidal pumping flux in addition to the vertical steady shear flux, so the vertical steady shear flux is not equal to the density-driven flux. Instead, we estimate the overall seasonal baroclinic flux by assuming the

density-driven fluxes scale with  $\frac{d\bar{S}}{dx}$  like baroclinic exchange ( $n=2$ ), and that the

remaining flux is strictly tidal ( $n=0$ ). From this assumption, the dispersion coefficient

scaling of  $n=0.51$ , and the seasonal  $\frac{d\bar{S}}{dx}$  values, it is found that 7% of the fall flux and

45% of the summer experiment flux are density-driven.

The dispersion coefficient analysis in this section assumes no discontinuities, such as internal hydraulic controls [Farmer 1986]. A control would be most likely to exist at the Channel's cross-section area minimum during ebb tide at peak spring-runoff. Based on



densiometric Froude number calculations (equation 6), we did not observe an internal hydraulic control. However, a control may exist during more extreme conditions either at the Golden Gate, as suggested Monismith [2002], or at Carquinez Strait.

## **6.6 Exchange Summary**

The net flux of salt between a coastal estuary (San Francisco Bay, CA) and the ocean has been quantified using cross-sectional observations of velocity and salinity. The tidally-averaged net dispersive salt flux for each season was validated with a box model using independently collected data. Decomposing the dispersive flux by temporal and spatial correlations showed that the temporal correlation of cross-sectionally averaged salinity and velocity (tidal pumping flux) is the largest part of the dispersive flux of salinity into the bay. From the tidal pumping flux portion of the dispersive flux, it was shown that there is less exchange through the Golden Gate than was found in earlier studies.

Ocean-estuary exchange is often described as a combination of two independent mechanisms: density-driven exchange, such as gravitational circulation, and tidal processes, such as shear dispersion, tidal pumping and tidal trapping. In this study we found that exchange is also governed by an interaction between these mechanisms. Tidally trapped eddies created in shallow shoals are mixed into the main channel earlier in the tidal cycle during the wet season because the eddies are pushed seaward by gravitational circulation. The resulting increase in tidally-averaged dispersive salt flux into the bay indicates that a dispersion coefficient scaling for tidal pumping flux based only on tidal forcing will be inadequate. Instead, an appropriate dispersion coefficient to

describe tidal pumping will require some dependence on density forcing. In contrast, the vertical steady shear exchange, which is usually assumed to be baroclinic, was found to also be a result of bathymetric forcing from a sill adjacent to the study site, as well as density-driven increases in ebb-flood frictional phasing. This results in a weaker scaling of this flux component with density forcing than would be expected with a baroclinic approach alone.

Taken together, we have established that density forcing and bathymetry both influence ocean-estuary exchange, as would be expected. The two forcing mechanisms can not be decoupled, however, and both enter into quantification of the tidal pumping and vertically-sheared steady fluxes.

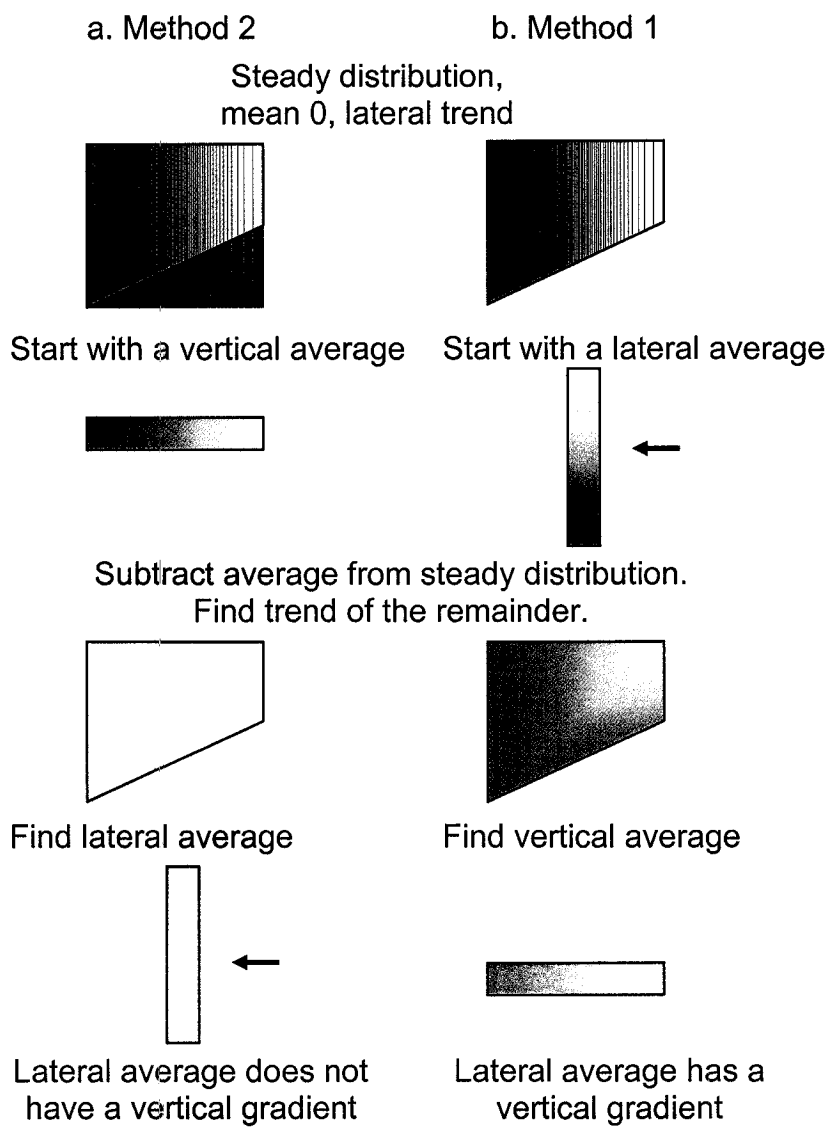


Figure 6.1: Averaging Order Schematic

This figure illustrates the effect of averaging order on vertical and lateral averages for non-rectangular cross-sections. Starting with a data that has a lateral trend and does not have a vertical trend, method 2 gives a lateral average with no vertical gradient, but method 1 gives a lateral average with a vertical gradient.

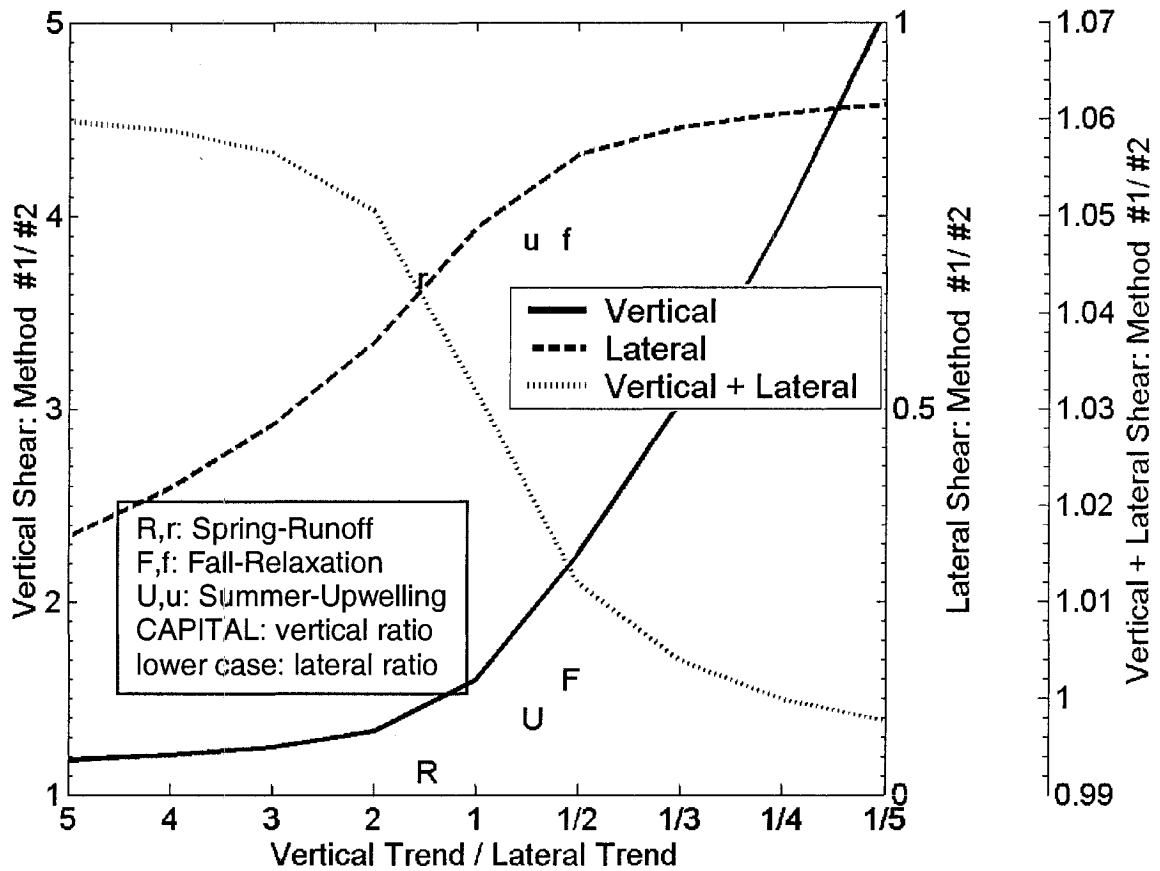


Figure 6.2: Averaging Order Ratios

Measured data points are plotted for each season, while the curves represent results from simulated data with linear trends. Velocity and salinity trends are imposed as in figure 6.1 for a range spanning conditions in which stratification and vertical shear are five times lateral salinity and velocity differences to conditions in which vertical salinity and velocity differences are one-fifth lateral ones. Lateral and vertical shear fluxes are calculated using both averaging order methods (eq. 59) for each set of conditions. Fluxes from the two methods are compared by examining the ratio of each flux from method #1 to method #2. Vertical shear flux is always larger in the first method, while lateral shear flux is always larger in the second. The amount of these differences changes with the proportion of vertical velocity and salinity trends to lateral trends.

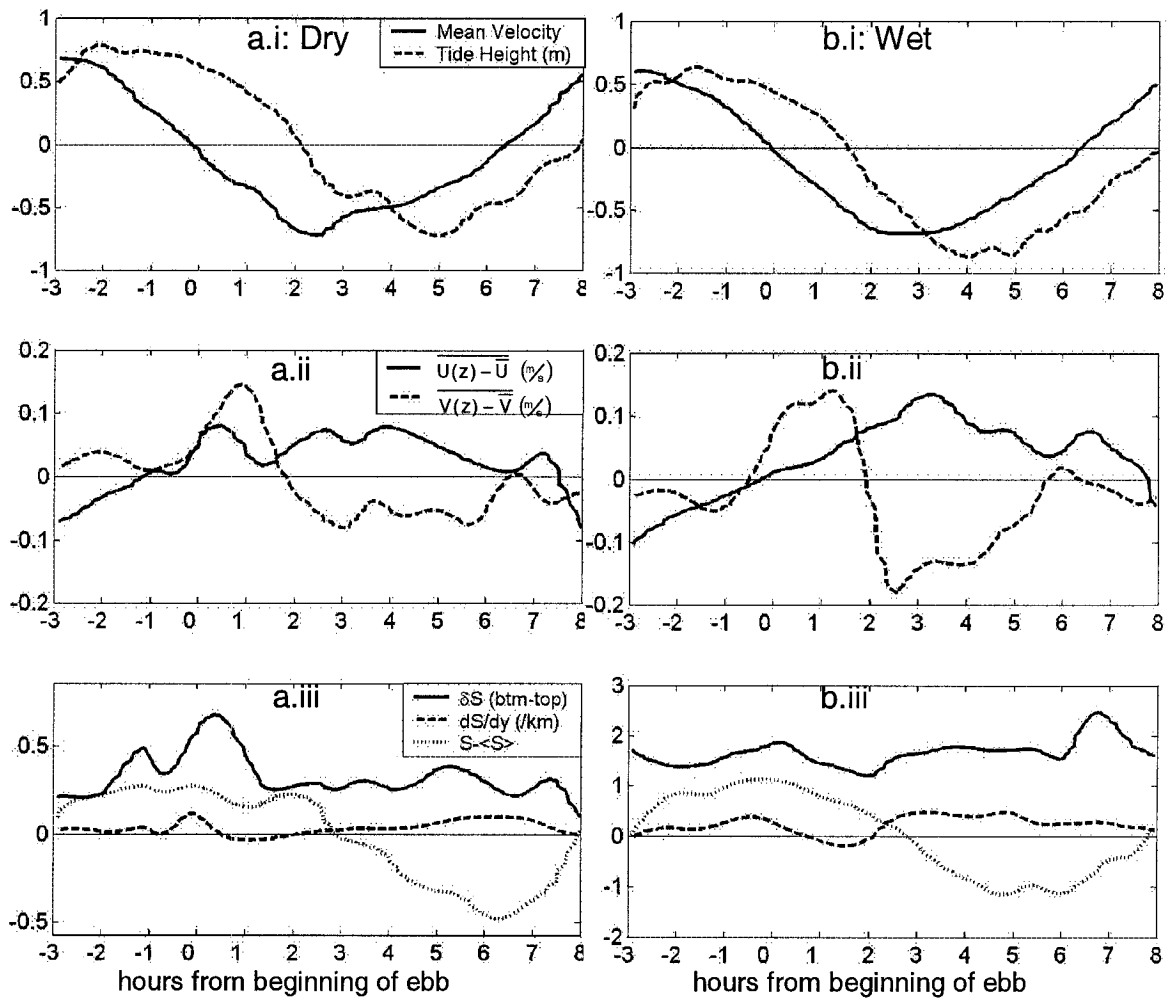


Figure 6.3: Tidally-Aligned Data

Measured tidally aligned mean velocities and tidal elevations are similar across seasons (a.i vs. b.i). Along-channel vertical shears and cross-channel vertical shears are stronger in wet seasons. 60.0 degrees east of north is the along-channel direction. (a.ii vs. b.ii). Stratification, the lateral salinity gradient, and the cross-section mean salinity deviation from the seasonal mean are scaled by 3.5 because the along-channel salinity gradient is 3.5 times larger in our wet season data (a.iii vs. b.iii).

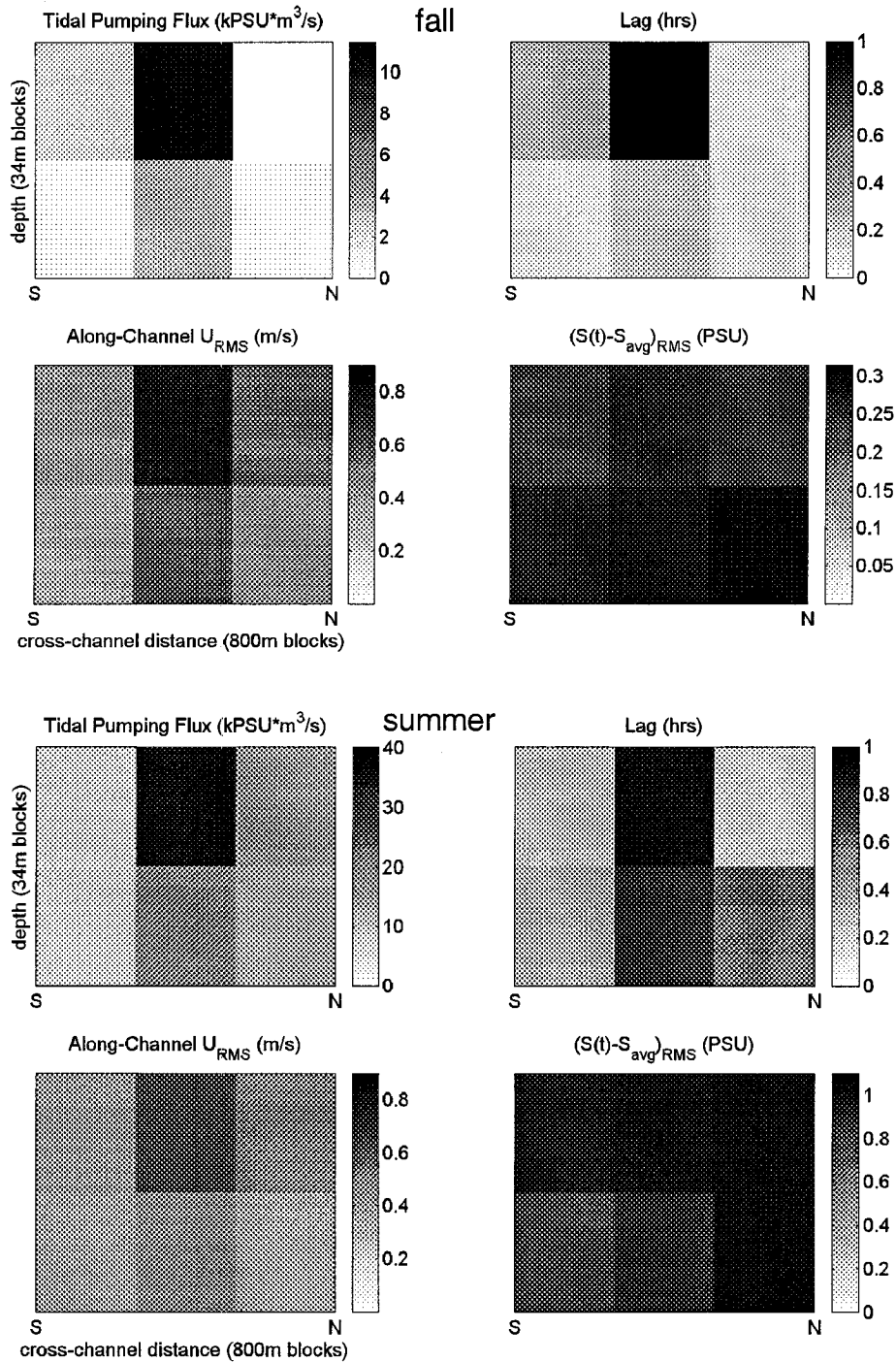


Figure 6.4: Tidal Pumping Across the Grid

Tidal pumping is proportional to the tidal range of velocity and salinity, as well as the lag from quadrature between salinity and velocity. Tidal pumping is strongest in the channel center. Seasonally, the salinity range as well as the lag increases with freshwater input.

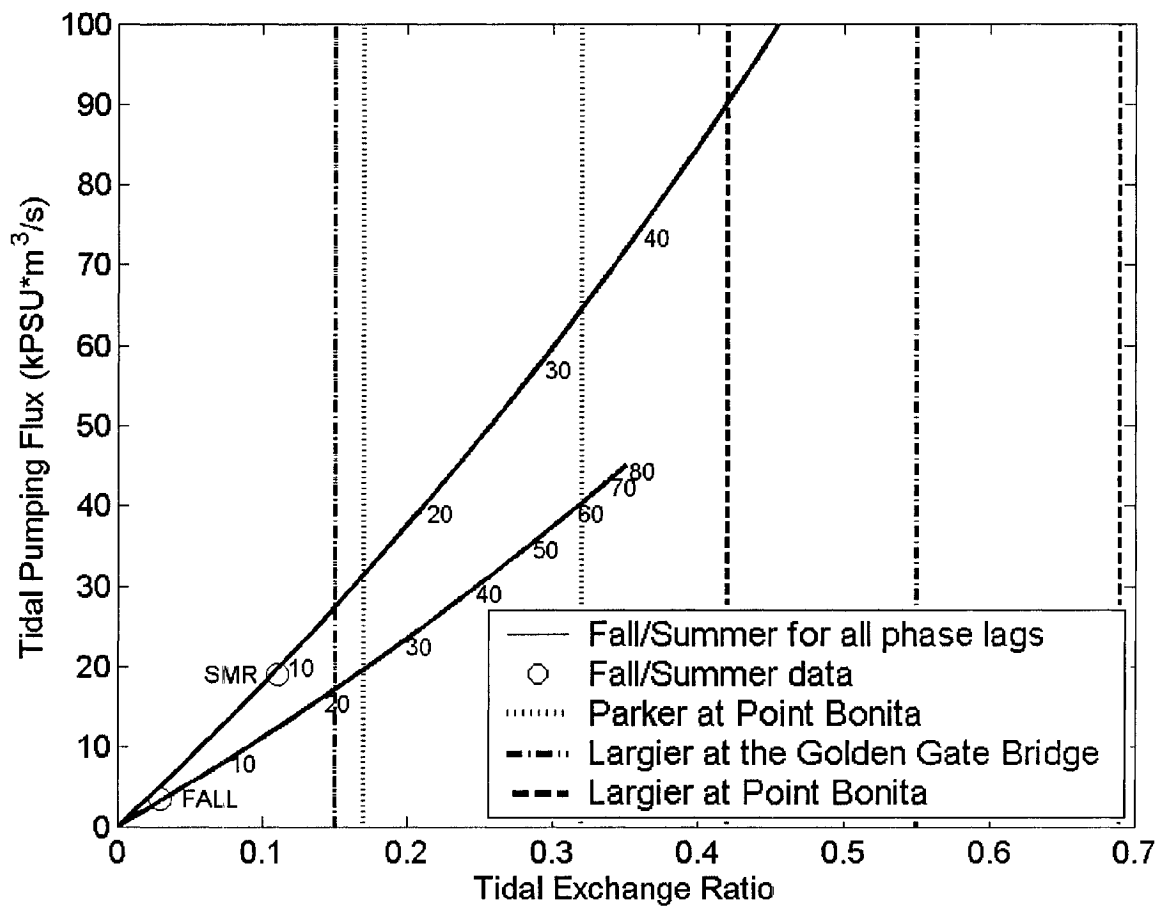


Figure 6.5: Tidal Pumping vs. TER

Both tidal pumping and TER increase with the phase lag ( $f$  in degrees) between mean flow [ $Q_0 \sin(\omega t)$ ] and salinity [ $-S_0 \sin(\omega t + \pi/2 + f)$ ]. Flow and salinity amplitudes ( $Q_0, S_0$ ) are from the fall and summer experiments.  $\omega$  is from the M2 tide. TER from Largier (1996) and Parker (1972), estimated for fall conditions, imply much higher tidal pumping flux and much higher phase lag than those in our experiments.

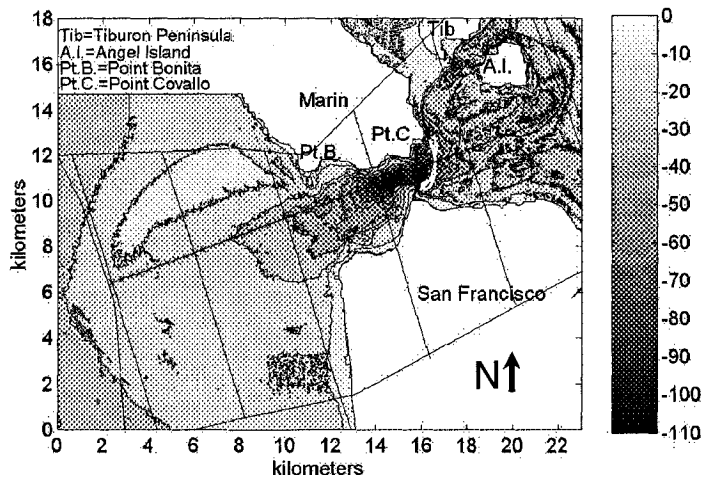


Figure 6.6a: Channel Cross-section Bathymetry

The map of bathymetry around the Golden Gate Channel has 10m contours. The transect path is 1 to 1.5km east of the Golden Gate Bridge, which is at the narrowest part of the channel contraction.

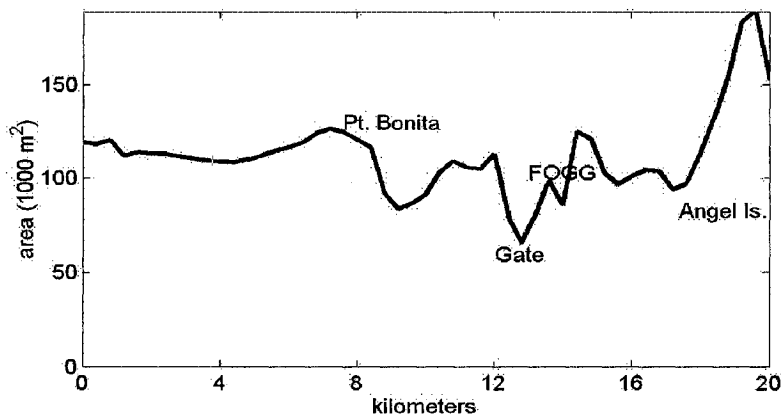


Figure 6.6b: Channel Cross-sectional Area

Cross-sectional areas are calculated at the normals to the along-channel axis line demarcated in figure 6.6a. The normals are bounded by a box that encloses the main channel. The resulting areas vary much less than channel width because the channel is deep where it contracts due to high shear stress, thus preventing sedimentation. FOGG, the label for this field site, stands for Flux Observations at the Golden Gate.



	FOGG		Monismith '02	
	Fall	Summer	Fall	Summer
$K \left( \frac{m^2}{s} \right)$	380	720	260	640
$\frac{dS}{dx} \left( \frac{1}{km} \right)$	<b>.06</b>	.21	<b>.216</b>	.245
S	32.1	<b>30.0</b>	31.68	<b>31.64</b>
n	0.51		6.2	

Figure 6.7: Dispersion Coefficients

Results from this experiment, Flux Observations at the Golden Gate, are compared to model results from Monismith et al. 2002. The model accurately predicted the along-channel dispersion coefficient (K) at the field site. However, the model severely overestimates the along-channel salinity gradient by fixing the location of the end of the estuary at the Golden Gate Bridge. As a result, the scaling of the dispersive salt flux with the along-channel salinity gradient, (which is parameterized by n), is overestimated.

## 7 Conclusions and Future Work

### 7.1 Methods

At the mouth of an estuary, particularly in the Golden Gate Channel, strong tides and bathymetric variability make it challenging to make meaningful measurements of exchange. Tow-yo profilers can be used to quantify exchange through estuary mouths, but there are a few notable drawbacks. The large turning radius of the profiler used in this study makes the Golden Gate Channel about as narrow a channel across which effective transects can be accomplished. However, with strong tides, one might not transect often enough to capture all of the tidal features of a larger channel. To resolve this problem for the SeaSciences Acrobat, we recommend increasing the wing size of the tow body. This would reduce cable payout lengths (by allowing quicker turns) and increase profiling depth, but it may also increase tension on the tow cable.

We explored two methods of diagnosing the instability problems the Acrobat often suffered at the deepest part of each profile. One could attach underwater tilt sensors to the Acrobat in the field, such as the ones sold by Applied Geomechanics Incorporated, or test the Acrobat in a long wide flume, such as one of the ocean engineering tow tanks at the Richmond Field Station [Yeung, pers. comm.]. We did not perform these diagnostic tests; nonetheless, we suggest two solutions to the instability problem. First, the Acrobat should communicate faster than 1 Hz with the computer. The initial instability seems correlated with this response time (based on the 4Hz SeaBird pressure sensor signal). Second, the planform area (area as viewed from above) of the wings is smaller than the

Acrobat's projected area facing the current. SeaScience now sells larger wings. They should add stability in addition to increasing diving ability. Along the same lines, we suggest streamlining the tow body and payload bay.

Despite these drawbacks, intensive field campaigns, such as this one, provide spatial resolution on the tidal time scale that is necessary for characterizing dynamic and topographically complex environments.

## **7.2 Tidal Pumping and Trapping**

Tidal pumping and tidal trapping appear in several forms at the landward end of the Golden Gate Channel. Aspects of pumping and trapping are influenced by density-driven circulation, and pumping and trapping generate density gradients which force density-driven circulation. By first considering tidal pumping and trapping effects, secondary processes not related to pumping and trapping can be isolated. Each of the analysis chapters (4-6) are summarized in this context.

In chapter 4, Tidal Variability, tidal pumping was evident in the first cross-channel velocity empirical orthogonal function (EOF) and second along-channel velocity EOF from Principal Component Analysis (PCA). The second cross-channel EOF, representing mainly cross-channel vertical shear, showed effects of a tidally trapped headland eddy, as well as a peak in shear at low slack. The lateral extent of a headland eddy was resolved numerically with TRIM. Differential advection from tidal pumping during the second

half of flood tide created lateral density gradients, which forced along-channel axial circulation.

In chapter 5, Residual Flow, several sources of residual circulation were observed; again the primary ones are related to tidal pumping and trapping. Traditional tidal pumping creates a lateral flow asymmetry, with residual flow into the estuary in the center and seaward along the perimeter. The measured size of this lateral asymmetry depends on tidal magnitude, distance of the transect path from the channel contraction, and degree to which the channel widens away from the contraction. Further, residual along-channel vertical shear is accentuated by tidal trapping of a headland eddy associated with the tidal pumping flood jet associated during the second half of flood tide. This eddy remains trapped behind a headland through the beginning of ebb tide. Upon exit, it forces dramatic cross-channel vertical shear changes over the sill connected to this headland.

The vertically-sheared residual flow varies more by season, as it is driven by density gradients in addition to bathymetric causes such as tidal pumping. Sill-induced vertical shear, associated with the tidal pumping lateral flow asymmetry, contributed the most to vertical shear during low to moderate freshwater flow forcing. As freshwater input strengthens the along-channel density gradient, traditional baroclinic circulation and SIPS (strain induced periodic stratification) also force significant amounts of residual vertical shear.

As first noted with PCA in chapter 4, one feature sticks out as not being related to tidal pumping or trapping. A residual vertical shear is caused by an asymmetry in frictional phasing between ebb-to-flood and flood-to-ebb transitions. Ebb tide draws North Bay and South Bay waters across the transect path. Their density difference generates lateral baroclinic circulation (seen in the PCA), which increases stratification and thus also increases frictional phasing. Seasonally, as shown by Uncles and Peterson [1996], the North Bay density field responds faster to freshwater flow changes than South Bay, so the frictional phasing asymmetry does not increase linearly with residual shear from traditional baroclinic circulation.

Residual circulation mechanisms combine with scalar concentration fields to exchange salinity. The first major result from the exchange portion of this project is the demonstration that one could obtain reasonable values for exchange from our measurement techniques. A residual advective flux out of the estuary was not determined accurately in this data set, but values for dispersive salt flux into the estuary were validated with a box model using independently collected data. From these validated flux results, it was shown that there is less exchange through the Golden Gate than was estimated in earlier studies.

As with the residual flow mechanisms in chapter 5, tidal pumping is featured in analysis of both tidally driven and density-driven salinity exchange processes in chapter 6. Analysis is focused on the tidal pumping flux because it is the largest dispersive flux process in each of our three measurement seasons. Dispersion from tidal pumping, which

would be constant if it was merely a tidal process, increased with freshwater forcing because of density-driven advection of a tidally trapped eddy during the flood-ebb tide transition. Similarly, vertical exchange does not scale with  $U_{rms}$  or  $\frac{dS}{dx}$  as a traditional baroclinic exchange because it is also due to a combination of tidal and density-driven processes. The purely tidal process is sill-induced shear; estuarine circulation is the purely density-driven process; and shear from asymmetric frictional phasing increases both with tidal and density-driven forcing.

Because of the irregular bathymetry, residual flow and exchange at the Golden Gate are governed by non-traditional mechanisms. Most of these mechanisms are related to tidal pumping and trapping, which traditionally are forced by tides in combination with bathymetric variations, not density differences. At the landward end of the Golden Gate Channel, there is a rich variety of interactions between density-driven and bathymetry-forced residual flow and exchange mechanisms. These unconventional mechanisms scale differently with forcing than traditional ones. These uncommon complexities are important to investigate because they occur at the mouths of estuaries, and thus govern ocean-estuary exchange.

### **7.3 Considerations for Future Studies**

In every experiment, there is a tradeoff between spatial and temporal resolution or between temporal resolutions among several time scales. In this experiment, there is high spatial resolution at fine temporal scales. However, a shipboard survey experiment such as this one does not capture longer timescale effects, such as exchange variation across an

entire freshet pulse. Also, even over smaller scales of variability, such as semi-diurnal tides, longer time series sampling is necessary for establishing statistically significant results. Long time series data are best captured from moored instruments. Cross-channel velocity and density differences clearly influence along-channel shear and exchange, so it would be helpful to place pairs of moorings in the channel. Moorings should be located along a cross-section that has been or will be transected by an experiment such as this one.

Since the Golden Gate Bridge is not the downstream end of the estuary, data should be collected seaward of this experiment's transect path. In section 6.5, it was shown that models of X2 could be improved with more time series data at, and seaward of, the Golden Gate Bridge. More generally, full-bay numeric models require a good ocean boundary condition to adequately describe Central Bay and Golden Gate hydrodynamics. Presently, as mentioned in section 4.3, there is very little data available for calibrating the ocean boundary of San Francisco Bay in numerical models. High frequency (HF) radar stations, which measure surface water velocities continuously, are being placed along the entire West Coast over the next few years [<http://www.cencoos.org>]. HF radar has excellent temporal resolution and data can be collected 60 km from the shore-mounted units, but HF radar can not yet be used to measure within 2 km of shore nor will it ever be able to measure velocities at depth [*Paduan and Shulman, 2004*]. While not as informative as an array of moored ADCPs, these data could prove useful for calibrating the ocean boundary for full-bay numerical models. Similarly, satellite data can be used to

estimate surface concentrations of a variety of scalars in the coastal ocean, but with less temporal resolution than HF radar.

Moored scalar concentration sensors can also be used to calibrate the ocean boundary of numerical models. Two CTDs have been moored within the eddy on the south end of the transect path [the eddy is described in *Stone and Bourgerie*, 1999]. The USGS mooring has been maintained for the last several years on Presidio Shoal, on the eddy's north end [Cuetara, pers. comm. 2004]. Another USGS CTD [<http://sfbay.wr.usgs.gov>] was located on a pier south of the mooring until 2003, and since 2004 a NEOCO CTD has been located on an adjacent pier [<http://www.es.ucsc.edu/~neoco>]. Each CTD collects a data point every 15 minutes, so one can evaluate tidal changes in the eddy during each season. The effect of eddies on scalar concentrations measured by these CTDs is important for relating these measurements to conditions across the entire channel and to evaluating fluxes in the part of cross-section that was not included in the transect path. It would be easier to characterize salinity in the channel if the CTDs were located away from tidal eddies, such as the USGS station that was operated on the south tower of the bridge. However, it is logistically difficult to locate moorings at more ideal locations in the Golden Gate Channel, such as further from shore. Scalar concentration moorings located away from shore have the additional possible advantage of being configured to measure stratification, not just a single concentration. An alternative location that may suffer less from eddy influence is the old lighthouse on the point underneath the bridge on the north side of the channel (Lime Point). As described in 5.4, there are seasonal changes in the cross-channel density gradient that could be characterized with a CTD on



the north side to pair with the south side moorings. Additionally, the south shore CTDs could be configured to measure the along-channel density gradient. Moving seaward, density changes are smaller and it is more difficult to operate a mooring as one gets further from the protected bay; perhaps only one additional mooring would be sufficient for measuring salinity, temperature, and other scalars at the seaward end of the channel.

Chlorophyll concentration was measured in this experiment, but the results were not discussed. One could characterize phytoplankton exchange between San Francisco Bay and the coastal ocean with this data set. By combining the chlorophyll and velocity results, it can be shown that there was a net chlorophyll flux into the bay during our summer experiment and a net efflux during fall and spring. To put these fluxes in context, one could compare these results to both in-bay (e.g. USGS) and coastal ocean (e.g. CalCOFI, SeaWiFS) monitoring studies, and consider the degree to which oceanic and estuarine phytoplankton species are being exchanged through the Golden Gate. Future chlorophyll exchange studies might consider sampling closer to the water surface. Chlorophyll data from this project do not have much vertical variability, which is contrary to the expectation that the phytoplankton would be mainly in the photic zone. Perhaps this indicates that phytoplankton in the Golden Gate channel are mixed vertically by the tides, so tidal pumping dominates their motion and distribution, as opposed to their own buoyancy controlled diel migration patterns. Tidally-aligned chlorophyll concentration results do not have as regular patterns as the salinity and temperature data, so one might need a longer time series to accurately describe phytoplankton exchange on the tidal timescale.

As with chlorophyll, suspended sediment concentration results from this experiment have not yet been described. At this field site, our typical suspended particles (15 $\mu$ m) were nearly two orders of magnitude smaller than the bed particles [*Rubin and McCulloch, 1979*]. Based on a Rouse profile, which considers settling velocity and vertical mixing, one expects no measurable vertical concentration gradient, however, a vertical gradient was found that would indicate a steady baroclinic influx of suspended sediment. Future studies might investigate the source of this vertical gradient. We note that this vertical influx is in the opposite direction as the tidal pumping flux associated with the along-channel concentration gradient. It would be useful to measure closer to the bed, where larger concentration gradients are expected. Furthermore, this signal varied more than chlorophyll, so, as with chlorophyll, one should consider collecting over a longer time period. Spatial gradients are typically not as strong as for salinity or temperature, so one might trade off spatial resolution for a longer time series.

While the overall effect of the Point Cavallo sill on exchange is discussed in chapter 5, the details of the front, eddy, and shear zone generation mechanisms were not probed. From the water surface pictures taken in the summer experiment, there are two front patterns: advection of the Point Cavallo eddy in mid-ebb tide, and shear lines emanating from and vortices shedding off of the sill during the second half of flood. The front demarking the end of the eddy moves at the mean tidal velocity as it crosses the transect path (figures 7.1 and 7.2). Correlating with transect data, there are strong shears and a sharp density discontinuity at the front (figure 7.3). In chapter 6, density-driven

acceleration was estimated, but it remains to be seen how much entrainment occurs across the front [*O'Donnell, 1993*] or how it evolves vertically in time. After the front at the end of the eddy, large shears develop over the sill, indicating that there may be internal hydraulic effects or vertical flow separation at this location [*Baines, 1995*]. Unlike Farmer and Armi's [1986] development, this sill does not cross the entire channel, so one needs to consider how flow moves around, not just over the sill [*Geyer, 1993; MacDonald and Geyer, 2005; Nash and Moum, 2001*]. Vortices of about 100m across shed off the edges of a gap in the Point Cavallo sill during the second half of flood tide. With only a few images to evaluate, it is not clear how often they shed, what constrains their size, or how they contribute to mixing by the sill. In the absence of a field campaign of cross-sill (as opposed to this experiment's along-sill) transects, these effects could be studied with a numerical model. The relevant portions of this data set could be augmented cheaply by collecting a much longer photographic time series at with images that span the entire Point Cavallo sill.

Large fauna, such as water birds, seals, and fish, may concentrate along tidal fronts and shear zones at the Golden Gate [*Burger and Holm, 2002; Johnston et al., 2005*]. From this experiment, it appears that birds and seals are present at the transect path during the second half of flood tide, at the same time as the strong surface features surface. A multiyear survey of surface seabird foraging patterns in western Central San Francisco Bay [*Saenz et al. in prep.*] finds that these birds, mostly cormorants, cluster on flood tide in the lee of the Point Cavallo sill and in the Point Cavallo eddy. The next step would be to correlate cormorant prey concentrations with frontal and shear features. Acoustic

backscatter of a variety of frequencies could be used to image both subsurface turbulent features and concentrations of organisms [*Trevorrow et al.*, 2005].

From large-scale exchange characteristics to small-scale transient habitats, there are a wide variety of areas that warrant further study of hydrodynamics at the Golden Gate.

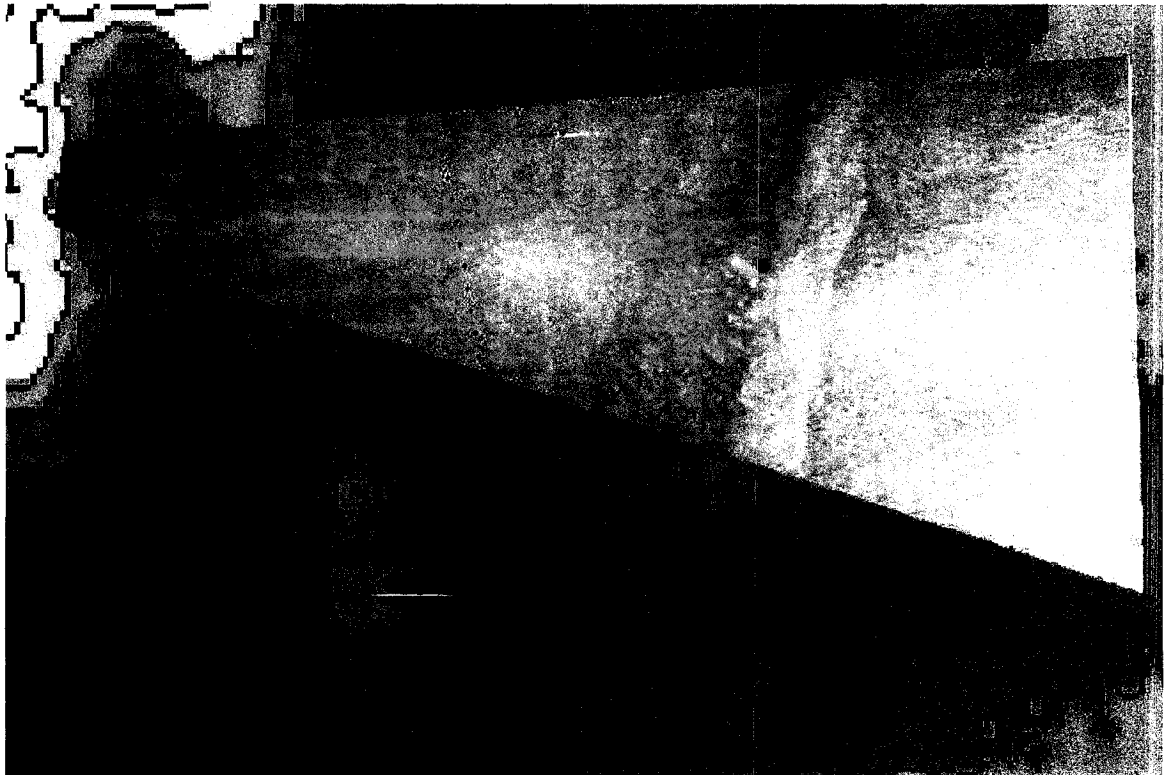


Figure 7.1: Photograph of a Lateral Front

Photograph overlaid on bathymetry from figure 2. The dot marks the location of a cross-channel front marking the landward end of a headland eddy crossing the transect path.

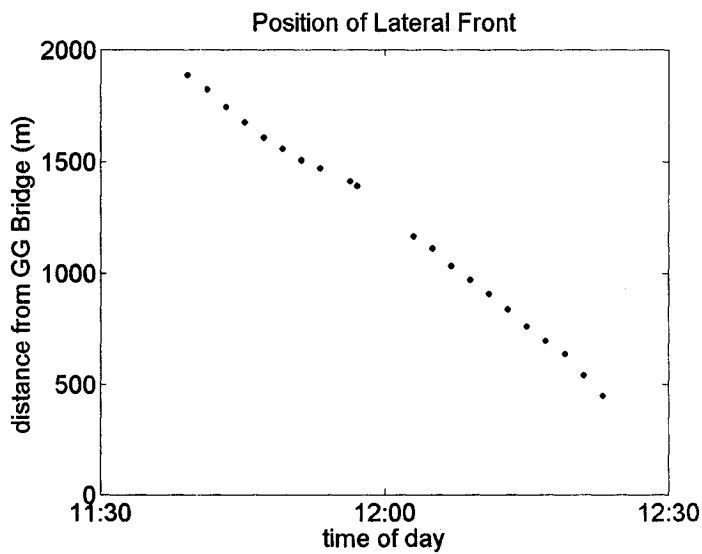


Figure 7.2: A Lateral Front Follows the Eddy

The front moves at the mean water surface velocity.

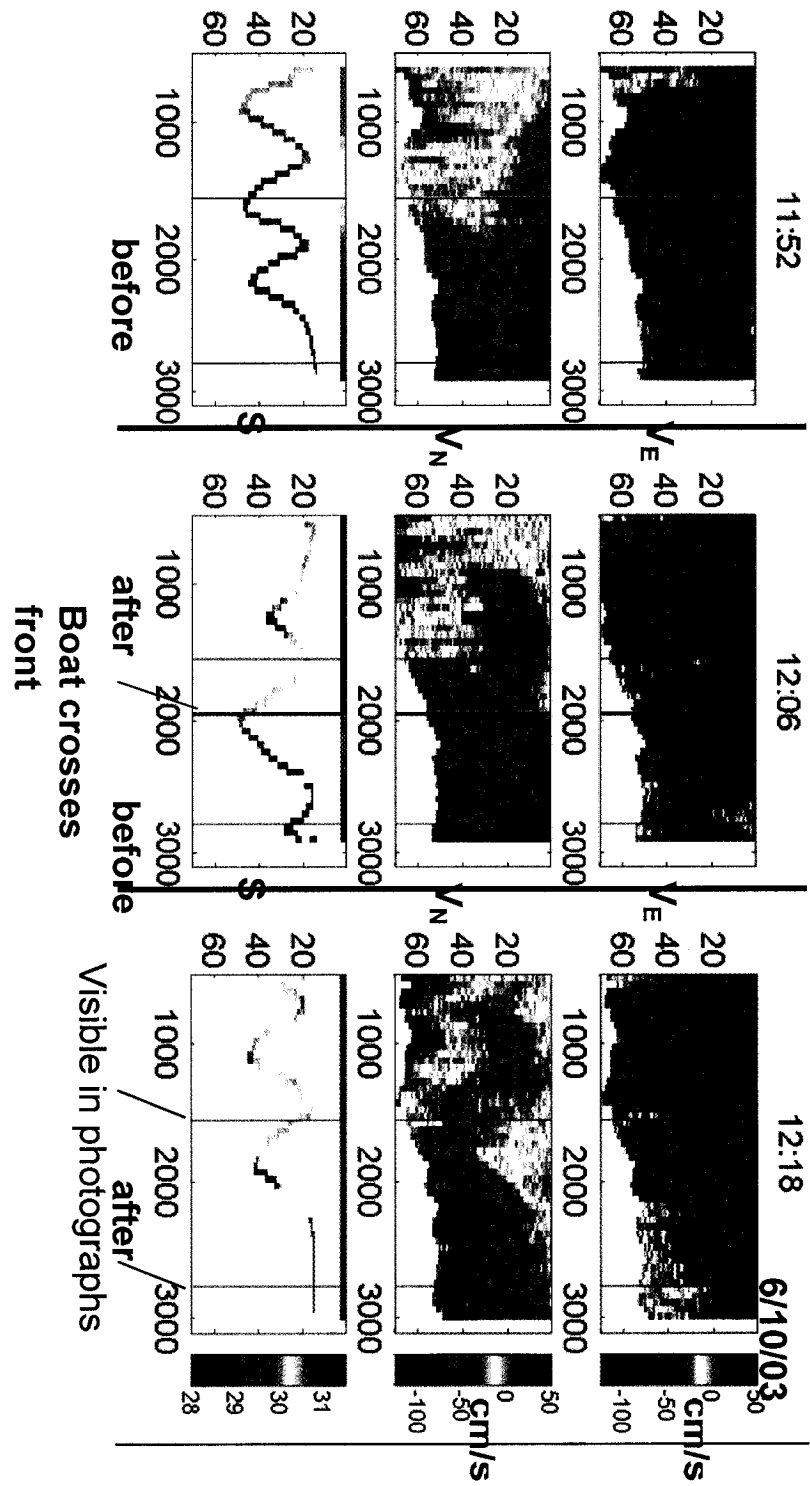


Figure 7.3: Sudden Changes at the Front

Depth vs. distance from the south shore along transect path

## References

- Atwater, B.F., C.W. Hedel, and E.J. Helley, Later quaternary depositional history, holocene sea-level changes, and vertical crustal movement, southern San Francisco Bay, California, *Mar. Chem.*, *64* (1), 1-15, 1999.
- Austin, J.A., Estimating the mean ocean-bay exchange rate of the Chesapeake Bay, *JGRO*, *107* (C11), 3192, 2002.
- Baines, P.G., *Topographic effects in stratified flows*, 482 pp., Cambridge University Press, Cambridge, 1995.
- Barth, J.A., D. Bogucki, S.D. Pierce, and P.M. Korso, Secondary circulation associated with a shelfbreak front, *Geophys. Res. Let.*, *25* (15), 2761-2764, 1998.
- Bowen, M.M., and W.R. Geyer, Salt transport and the time-dependent salt balance of a partially stratified estuary, *J. Geophys. Res.*, *108* (C5), 3158, 2003.
- Burger, A.E., and K.J. Holm, Foraging behaviour and resource partitioning by diving birds during winter in areas of strong tidal currents, *Waterbirds*, *25* (3), 312-325, 2002.
- Carlson, P.R., and D.S. McCulloch, The Floor of Central San Francisco Bay, *Mineral Information Service*, *23* (5), 97-107, 1970.
- Casulli, V., Semi-implicit finite difference methods for the two-dimensional shallow water equations, *J. Comput. Phys.*, *86*, 56-74, 1990.
- Chadwick, D.B., and J.L. Largier, The influence of tidal range on the exchange between San Diego Bay and the ocean, *JGRO*, *104* (C12), 29,885-829,899, 1999a.
- Chadwick, D.B., and J.L. Largier, Tidal exchange at the bay-ocean boundary, *JGR-O*, *104* (C12), 29,901-929,924, 1999b.
- Chatwin, P.C., Some remarks on the maintenance of the salinity distribution in estuaries, *Estuarine Coastal and Shelf Science*, *4*, 555-566, 1976.
- Cheng, R.T., V. Casulli, and J.W. Gartner, Tidal, Residual, Intertidal Mudflat (TRIM) model and its applications to San Francisco Bay, California, *ECSS*, *36*, 235-280, 1993.
- Chin, J.L., F.L. Wong, P.R. Carlson, and D.A. Cacchione, Shifting shoals and shattered rocks: how man has transformed the floor of west-central San Francisco Bay, *USGS Circular*, *1259*, 2004.
- Cloern, J.E., Phytoplankton bloom dynamics in coastal ecosystems: a review with some general lessons from sustained investigation of San Francisco Bay, California, *Rev. Geophys.*, *34* (2), 127-168, 1996.
- Collins, C.A., C.G. Castro, H. Asanuma, T.A. Rago, S.K. Han, R. Durazo, and F.P. Chavez, Changes in the hydrography of Central California water associated with the 1997-1998 El Nino, *Prog. Ocean.*, *54*, 129-147, 2002.
- Conomos, T.J., Properties and circulation of San Francisco Bay waters, in *San Francisco Bay: The Urbanized Estuary*, edited by T.J. Conomos, pp. 47-84, Pacific Division, AAAS, 1979.
- Conomos, T.J., D.S. McCulloch, D.H. Peterson, and P.R. Carlson, Drift of surface and near-bottom waters of the San Francisco Bay system: March 1970 through April 1971, in *USGS Open-File Map*, USGS, 1971.
- Crowe, C.T., D.F. Elger, and J.A. Roberson, *Engineering Fluid Mechanics*, 714 pp., Wiley, New York, 2001.

- DWR, California Department of Water Resources Delta Outflow, [cdec.water.ca.gov](http://cdec.water.ca.gov), 2004.
- Dyer, K.R., *Estuaries: A Physical Introduction*, John Wiley & Sons, 1997.
- Edwards, K.A., P.M. MacCready, J.N. Moum, G. Pawlak, J.M. Klymak, and A. Perlin, Form drag and mixing due to tidal flow past a sharp point, *J. Phys. Ocean.*, *34*, 1297-1312, 2004.
- Eggleston, D.B., D.A. Armstrong, W.E. Elis, and W.S. Patton, Estuarine fronts as conduits for larval transport: hydrodynamics and spatial distribution of Dengeness crab postlarvae, *MEPS*, *164*, 73-82, 1998.
- Epifanio, C.E., and R.W. Garvine, Larval Transport on the Atlantic continental shelf of North America: a review, *Estuarine, Coastal and Shelf Science*, *52*, 51-77, 2001.
- Farmer, D.M., and L. Armi, Maximal two-layer exchange over a sill and through the combination of a sill and contraction with barotropic flow, *J. Fluid Mech.*, *164*, 53-76, 1986.
- Farmer, D.M., and L. Armi, Stratified flow over topography: the role of small-scale entrainment and mixing in flow establishment, *Proc. R. Soc. Lond. A*, *4555*, 3221-3258, 1999.
- Findikakas, A.N., J. Imberger, I.S. Hansen, L.A. Delgado, R. Garcia-Martinez, and E. Gundlach, A study of environmental remediation options for Lake Maracaibo, Venezuela, in *Proceedings XXIX IAHR Congress*, Beijing, China, 2001.
- Fischer, H.B., Mass transport mechanisms in partially stratified estuaries, *J. Fluid Mech.*, *53* 671-687, 1972.
- Fischer, H.B., J. Imberger, E.J. List, R.C.Y. Koh, and N.H. Brooks, *Mixing in Inland and Coastal Waters*, Academic Press, 1979.
- Geyer, W.R., Three-dimensional tidal flow around headlands, *JGR*, *98* (c1), 955-966, 1993.
- Geyer, W.R., R.C. Beardsley, S.J. Lentz, J. Candela, R. Limeburner, W.E. Johns, C.G. Castro, and I.D. Soares, Physical oceanography of the Amazon shelf, *Cont. Shelf Res.*, *16* (56), 575-616, 1996.
- Geyer, W.R., and H. Nepf, Tidal pumping of salt in a moderately stratified estuary, in *Buoyancy Effects on Coastal and Estuarine Dynamics*, pp. 213-226, American Geophysical Union, 1996.
- Geyer, W.R., and R. Signell, Measurement of Tidal Flow Around a Headland With a Shipboard Acoustic Doppler Current Profiler, *JGR-Oceans*, *95* (C5), 3189-3197, 1990.
- Hansen, D.V., and M. Rattray, Gravitational circulation in straits and estuaries, *J. Mar. Res.*, *23* (2), 104-122, 1965.
- Hansen, D.V., and M. Rattray, New dimensions in estuary classification, *Limnology and Oceanography*, *6* (3), 319-326, 1966.
- Horn, D.A., B. Laval, J. Imberger, and A.N. Findikakas, Field study of physical processes in Lake Maracaibo, in *Proceedings XXIX IAHR Congress*, Beijing, China, 2001.
- Ivey, G.N., Stratification and mixing in sea straits, *Deep Sea Res.*, *51*, 441-451, 2004.
- Jassby, A.D., J.E. Cloern, and T.M. Powell, Organic carbon sources and sinks in San Francisco Bay: variability induced by river flow, *Mar. Ecol. Prog. Ser.*, *95*, 39-54, 1993.



- Jassby, A.D., W.J. Kimmerer, S.G. Monismith, C. Armor, J.E. Cloern, T.M. Powell, J.R. Schubel, and T.J. Vendliniski, Isohaline position as a habitat indicator for estuarine populations, *Ecol. Appl.*, 5 (1), 272-289, 1995.
- Jay, D.A., W.R. Geyer, R.J. Uncles, J. Vallino, J.L. Largier, and W.R. Boynton, A review of recent developments in estuarine scalar flux estimation, *Estuaries*, 20 (2), 262-280, 1997.
- Jay, D.A., and J.D. Smith, Residual circulation in shallow estuaries. 1. Highly stratified, narrow estuaries, *J. Geophys. Res.*, 95 (C1), 711-731, 1990.
- Johnston, D.W., A.J. Westgate, and A.J. Read, Effects of fine-scale oceanographic features on the distribution and movements of harbour porpoises *Phocoena phocoena* in the Bay of Fundy, *MEPS*, 295, 279-293, 2005.
- Kay, D.J., and D.A. Jay, Interfacial mixing in a highly stratified estuary: 1. characteristics of mixing, *JGR*, 108 (C3), 17, 2003a.
- Kay, D.J., and D.A. Jay, Interfacial mixing in a highly stratified estuary: 2. a 'method of constrained differences' approach for the determination of the momentum and mass balances and the energy of mixing, *JGR*, 108 (C3), 18, 2003b.
- Kay, D.J., D.A. Jay, and J.D. Musiak, Salt transport calculations from acoustic doppler current profiler (ADCP) and conductivity-temperature-depth (CTD) data: a methodological study, in *Buoyancy effects on coastal and estuarine dynamics: coastal and estuarine studies*, edited by D.G. Aubrey, and C.T. Friedrichs, pp. 195-212, AGU, 1996.
- Kimmerer, W.J., Effects of freshwater flow on abundance of estuarine organisms: physical effects or trophic linkages?, *MEPS*, 243, 39-55, 2002a.
- Kimmerer, W.J., Physical, biological, and management responses to variable freshwater flow into the San Francisco estuary, *Estuaries*, 25 (6B), 1275 -1290, 2002b.
- Knauss, J.A., *Introduction to physical oceanography*, 309 pp., Prentice Hall, Upper Sadle River, N.J., 1997.
- Krone, R.B., Recent sedimentation in the San Francisco Bay system, in *San Francisco Bay: The Ecosystem*, edited by T. Hollibaugh, pp. 63-68, AAAS, 1996.
- Kundu, P., and I.M. Cohen, *Fluid Mechanics*, 730 pp., Academic Press, San Diego, 2002.
- Largier, J.L., Hydrodynamic exchange between San Francisco Bay and the ocean: the role of ocean circulation and stratification, in *San Francisco Bay: the Ecosystem*, edited by J.T. Hollibaugh, pp. 69-104, AAAS, 1996.
- Lerczak, J.A., and W.R. Geyer, Modeling the lateral circulation in straight, stratified estuaries, *J. Phys. Ocean.*, 34, 1410-1427, 2004.
- LTMS, *Long-term management strategy for the placement of dredged material in the San Francisco Bay region*, USACE, 1998.
- MacCready, P.M., Toward a unified theory of tidally-averaged estuarine salinity structure, *Estuaries*, 27 (4), 561-570, 2004.
- MacCready, P.M., and W.R. Geyer, Estuarine adjustment to changes in river flow and tidal mixing, *JPO*, 29 (4), 708-726, 1999.
- MacDonald, D.G., and W.R. Geyer, Hydraulic control of a highly stratified estuarine front, *J. Phys. Ocean.*, 35, 374-387, 2005.
- Monismith, S.G., J.R. Burau, and M.T. Stacey, Stratification dynamics and gravitational circulation in northern San Francisco Bay, in *San Francisco Bay: the Ecosystem*, edited by J.T. Hollibaugh, pp. 123-156, AAAS, 1996.

- Monismith, S.G., and D.A. Fong, A simple model of mixing in stratified tidal flows, *JGR*, 101 (C12), 28583-28595, 1996.
- Monismith, S.G., W.J. Kimmerer, J.R. Burau, and M.T. Stacey, Structure and flow-induced variability of the subtidal salinity field in northern San Francisco Bay, *J. Phys. Ocean.*, 32, 3003-3019, 2002.
- Munk, W.H., and E.R. Anderson, Notes on a theory of the thermocline, *J. Mar. Res.*, 7 (3), 276-295, 1948.
- Nash, J.D., and J.N. Moum, Internal hydraulic flows of the continental shelf: high drag states over a small bank, *JGR*, 106 (C3), 4593-4612, 2001.
- Nepf, H.M., and W.R. Geyer, Intratidal variations in stratification and mixing in the Hudson estuary, *J. Geophys. Res.*, 101 (C5), 12,079-12,086, 1996.
- Nunes, R.A., and J.H. Simpson, Axial convergence in a well-mixed estuary, *Est., Coast. & Shelf Sci.*, 20, 637-649, 1985.
- O'Donnell, J., Surface fronts in estuaries: a review, *Estuaries*, 16, 12-39, 1993.
- Okubo, A., Effect of shoreline irregularities on streamwise dispersion in estuaries and other embayments, *Netherlands J. of Sea Research*, 6 (1-2), 213-224, 1973.
- Ozsoy, E., *Flow and mass transport in the vicinity of tidal inlets*, 196 pp., University of Florida, Gainesville, 1977.
- Paduan, J.D., and I. Shulman, HF radar data assimilation in the Monterey Bay area, *JGR-O*, 109 (C7), 2004.
- Parker, D.S., D.P. Norris, and A.W. Nelson, Tidal exchange at the Golden Gate, *J. San. Eng. Div. Proc. ASCE*, 98, 305-323, 1972.
- Pawlowicz, R., Quantitative visualization of geophysical flows using low-cost oblique digital time-lapse imaging, *J. Ocean Eng.*, 28 (4), 699-710, 2003.
- Petrick, E.P., C.A. Collins, and W.C. Boicourt, Currents through the Golden Gate, in *San Francisco Bay: The Ecosystem*, edited by T.J. Hollibaugh, pp. 105-122, AAAS, 1996.
- Prandle, D., On salinity regimes and the vertical structure of residual flows in narrow tidal estuaries, *Est., Coast. Shelf Sci.*, 20 615-635, 1985.
- Prandle, D., A. Murray, and R. Johnson, Analysis of Flux Measurements in the River Mersey, in *Coastal and Estuarine Studies*, edited by R.T. Cheng, pp. 413-430, Springer-Verlag, 1990.
- Preisendorfer, R.W., *Principal Component Analysis in Meteorology and Oceanography*, Elsevier, New York, 1991.
- Price, J.F., R.A. Weller, and R. Pinkel, Diurnal cycling: observations and models of the upper-ocean response to diurnal heating, cooling, and wind-mixing., *JGR*, 91, 8411-8427, 1986.
- Ralston, D.K., and M.T. Stacey, Longitudinal mixing and lateral circulation in the intertidal zone, *JGR in review*, 2005.
- Ramp, S.R., J.D. Paduan, I. Shulman, J. Kindle, F.L. Bahr, and F.P. Chavez, Observations of upwelling and relaxation events in the northern Monterey Bay during August 2000, *JGRO*, 110 (7), 13, 2005.
- Rattray, M., and J.G. Dworski, Comparison of methods for analysis of the transverse and vertical circulation contributions to the longitudinal advective salt flux in estuaries, *Est. Coast. Mar. Sci.*, 11, 515-536, 1980.

- Redfield, A.C., The tidal system of Lake Maracaibo, Venezuela, *Limnology and Oceanography*, 6 (1), 1-12, 1961.
- Rubin, D.M., and D.S. McCulloch, The movement and equilibrium of bedforms in Central San Francisco Bay, in *San Francisco Bay: The Urbanized Estuary*, edited by T.J. Conomos, pp. 97-114, Pacific Division, AAAS, 1979.
- Rubin, Y., *Applied Stochastic Hydrogeology*, 391 pp., Oxford University Press, 2003.
- Schoellhamer, D.H., 1996 Annual Report of the Regional Monitoring Program for Trace Substances, pp. 65-77, USGS, 1996.
- Schoellhamer, D.H., Variability of suspended-sediment concentration at tidal to annual time scales in San Francisco Bay, USA, *Cont. Shelf Res.*, 22 1857-1866, 2002.
- Sherman, F.S., J. Imberger, and G.M. Corcos, Turbulence and mixing in stably stratified waters, *Ann. Rev. Fluid Mech.*, 10, 267-288, 1978.
- Simpson, J.H., J. Brown, J. Matthews, and G. Allen, Tidal straining, density currents, and stirring in the control of estuarine stratification, *Estuaries*, 13 (2), 125-132, 1990.
- Simpson, J.H., T.P. Rippeth, and A.R. Campbell, The phase lag of turbulent dissipation in tidal flow, in *Interactions between estuaries, coastal seas and shelf seas*, edited by T. Yanagi, pp. 57-67, Terra Scientific, 2000.
- Stacey, M.T., J.R. Burau, and S.G. Monismith, Creation of residual flows in a partially stratified estuary, *J. Geophys. Res.*, 106 (C8), 17,013-017,037, 2001.
- Stommel, H., and H.G. Farmer, *On the Nature of Estuarine Circulation*, Woods Hole Oceanographic Institution, 1952.
- Stone, P., and R. Bourgerie, Towed acoustic doppler current profiler measurements at the Golden Gate in San Francisco Bay, in *IEEE Oceans '99 Conference*, CO-OPP NOS/NOAA, 1999.
- Talke, S.A., and M.T. Stacey, The influence of ocean swell on flows over an estuarine intertidal mudflat in San Francisco Bay, *ECSS*, 58 (3), 531-554, 2003.
- Taylor, J.R., *An introduction to error analysis: the study of uncertainties in physical measurements*, University Science Books, 1997.
- Timmermans, M., and L.J. Pratt, Hydraulic control of exchange flows through deep passages and straits, in *EOS Trans. Suppl.*, pp. 42G-10, AGU Ocean Sciences, Portland, OR, 2004.
- Trevorrow, M.V., D.L. Mackas, and M.C. Benfield, Comparison of multifrequency acoustic and in situ measurements of zooplankton abundances in Knight Inlet, British Columbia, *J. Acoustic Soc. Amer.*, 117 (6), 3574-3588, 2005.
- Uncles, R.J., and D.H. Peterson, The long-term salinity field in San Francisco Bay, *Cont. Shelf Res.*, 16 (15), 2005-2039, 1996.
- USGS, Water quality of San Francisco Bay, [sfbay.wr.usgs.gov/access/wqdata](http://sfbay.wr.usgs.gov/access/wqdata), 2004.
- Valle-Levinson, A., and K.M. Lwiza, The effects of channels and shoals on exchange between the Chesapeake Bay and the adjacent ocean, *JGR*, 100 (C9), 18,551-518,563, 1995.
- Valle-Levinson, A., and J. O'Donnell, Tidal interaction with buoyancy driven flow in a coastal plain estuary, in *Buoyancy Effects on Coastal and Estuarine Dynamics*, edited by D.G. Aubrey, and C.T. Friedrichs, pp. 265-281, AGU, 1996.
- van Geen, A., and S.N. Luoma, The impact of human activities on sediments of San Francisco Bay, California: an overview, *Mar. Chem.*, 64, 1-6, 1999.

- Walters, R.A., R.T. Cheng, and T.J. Conomos, Time scales of circulation and mixing processes of San Francisco Bay waters, *Hydrobiologia*, 129, 13-36, 1985.
- Walters, R.A., and J.W. Gartner, Subtidal sea level and current variations in the northern reach of San Francisco Bay, *Est. Coast. Shelf Sci.*, 21, 17-32, 1985.
- Wells, M.G., and G.J.F. van Heijst, A model of tidal flushing of an estuary by dipole formation, *Dynamics of Atmos. Oceans*, 37, 223-244, 2003.
- Wessel, P., and D. Bercovici, Interpolation with splines in tension: a Green's function approach, *Math. Geol.*, 30 (1), 77-93, 1998.
- Wright, S.A., and D.H. Schoellhamer, Trends in the sediment yield of the Sacramento River, California, 157-2001, *San Francisco Estuary and Watershed Science*, 2 (2), 2004.
- Zimmerman, J.T.F., Whirlpool - a review of horizontal dispersion by tidal and residual currents, *Netherlands J. of Sea Research*, 20 (2-3), 133-154, 1986.